

Journal of Combustion

Advanced Engine Flows and Combustion

Lead Guest Editor: Zhijun Peng

Guest Editors: Thanos Megaritis, Chih-Jen Sung, Minoru Yaga, Paul Hellier,
and Guohong Tian





Advanced Engine Flows and Combustion

Journal of Combustion

Advanced Engine Flows and Combustion

Lead Guest Editor: Zhijun Peng

Guest Editors: Thanos Megaritis, Chih-Jen Sung, Minoru Yaga,
Paul Hellier, and Guohong Tian



Copyright © 2017 Hindawi. All rights reserved.

This is a special issue published in “Journal of Combustion.” All articles are open access articles distributed under the Creative Commons Attribution License, which permits unrestricted use, distribution, and reproduction in any medium, provided the original work is properly cited.

Editorial Board

Ajay K. Agrawal, USA
Kalyan Annamalai, USA
I. P. Borovinskaya, Russia
Craig T. Bowman, USA
Steven G. Buckley, USA
S. R. Chakravarthy, India
Lea-Der Chen, USA
Michael A. Delichatsios, UK
Ofodike A. Ezekoye, USA
Michael Fairweather, UK
Zoran Filipi, USA

Sergey M. Frolov, Russia
E. G. Giakoumis, Greece
Peyman Givi, USA
Ashwani K. Gupta, USA
Yannis Hardalupas, UK
Hong G. Im, KSA
Yiguang Ju, USA
Kazunori Kuwana, Japan
Cheng-Xian Lin, USA
Ji-dong Lu, China
Thanos Megaritis, UK

Michael F. Modest, USA
Alexander S. Mukasyan, USA
Tran X. Phuoc, USA
Ishwar K. Puri, Canada
C. D. Rakopoulos, Greece
Dimitrios C. Rakopoulos, Greece
Ruggero M. Santilli, USA
Richard Saurel, France
Benjamin Shaw, USA
Christopher W. Wilson, UK

Contents

Advanced Engine Flows and Combustion

Zhijun Peng, Thanos Megaritis, Chih-Jen Sung, Minoru Yaga, Paul Hellier, and Guohong Tian
Volume 2017, Article ID 9285097, 3 pages

Effects of Injection Rate Profile on Combustion Process and Emissions in a Diesel Engine

Fuqiang Bai, Zuowei Zhang, Yongchen Du, Fan Zhang, and Zhijun Peng
Volume 2017, Article ID 9702625, 8 pages

Small Engines as Bottoming Cycle Steam Expanders for Internal Combustion Engines

Rohitha Weerasinghe and Sandra Hounsham
Volume 2017, Article ID 1742138, 8 pages

Parametric Study to Improve Subpixel Accuracy of Nitric Oxide Tagging Velocimetry with Image Preprocessing

Ravi Teja Vedula, Mayank Mittal, and Harold Schock
Volume 2017, Article ID 6159802, 17 pages

Influence of Advanced Injection Timing and Fuel Additive on Combustion, Performance, and Emission Characteristics of a DI Diesel Engine Running on Plastic Pyrolysis Oil

Ioannis Kalargaris, Guohong Tian, and Sai Gu
Volume 2017, Article ID 3126342, 9 pages

Experimental Study on the Influence of DPF Micropore Structure and Particle Property on Its Filtration Process

Zhongwei Meng, Jia Fang, Yunfei Pu, Yan Yan, Yi Wu, Yongzhong Wang, and Qiang Song
Volume 2016, Article ID 9612856, 12 pages

Editorial

Advanced Engine Flows and Combustion

**Zhijun Peng,¹ Thanos Megaritis,² Chih-Jen Sung,³ Minoru Yaga,⁴
Paul Hellier,⁵ and Guohong Tian⁶**

¹University of Bedfordshire, Luton, UK

²Brunel University London, Uxbridge, UK

³University of Connecticut, Storrs, CT, USA

⁴University of the Ryukyus, Okinawa, Japan

⁵University College London, London, UK

⁶University of Surrey, Guildford, UK

Correspondence should be addressed to Zhijun Peng; jun.peng@beds.ac.uk

Received 12 July 2017; Accepted 12 July 2017; Published 7 August 2017

Copyright © 2017 Zhijun Peng et al. This is an open access article distributed under the Creative Commons Attribution License, which permits unrestricted use, distribution, and reproduction in any medium, provided the original work is properly cited.

The transport sector accounts for a significant part of carbon emissions worldwide, and so the need to mitigate the greenhouse effect of CO₂ from fossil fuel combustion and to reduce vehicle exhaust emissions has been the primary driver for developing cleaner and more efficient vehicle powertrains and environmentally friendly fuels. As alternatives to combustion engines have yet to overcome technical challenges to attain significant utilisation in the transport sector, piston-driven internal combustion engines and gas turbine aeroengines remain very attractive powertrain options due to their high thermal efficiency. Meanwhile, since the introduction of various emissions standards, which have forced the employment of various aftertreatment systems, the evolution of combustion process has been significant. Advanced combustion strategies have attempted to find in-chamber approaches either to meet these emission standards fully and thus avoid the need to use aftertreatment or, at the very least, to lower the performance demands required from aftertreatment systems thus reducing their cost and complexity. While the main focus of combustion system development has been recently to lower emissions of CO₂, there is also significant interest to lower nitric oxides (NO_x) and particulate matter (PM) emissions and other harmful emissions.

For piston-driven internal combustion engines, the most recent technology to have been successfully commercialised is Gasoline Direct Injection (GDI). GDI technology enables

the air-fuel charge to be appropriately stratified so that ultralean burn combustion for improved fuel efficiency and reduced emissions can be achieved. As fuel is injected at the latter stages of the compression stroke, combustion takes place in a cavity on the piston's surface which has normally a toroidal shape and is either placed in the centre (for a central injector) or displaced to one side of the piston that is closer to the injector position. The cavity creates swirl or tumble effects so that the small amount of air-fuel mixture is optimally placed near the spark plug. This stratified charge is surrounded mostly by air and residual gases, thereby keeping the fuel and the flame away from the cylinder walls. Those requirements demonstrate that it is critical for GDI engines to organise appropriate air motion around the cavity area to provide suitable air-fuel ratios for spark ignition and in the whole cylinder for necessary charge stratification.

Lean burn with decreased combustion temperature in GDI engines can provide low emissions and low heat losses, leading to improved efficiency. However, a new devastating knock named superknock, which is much different from traditional gasoline engine knock combustion and whose instantaneous in-cylinder pressure can reach above 200 bars, has become a main obstacle for increasing GDI engine power density. Researchers are actively engaged in researching superknock, but the mechanism by which it is generated and practical control strategy are still not fully clarified. A mainstream view is that, in a superknock cycle, the occurrence of

preignition is related to the dilution of the cylinder oil which may be caused by spray impingement on cylinder wall for turbocharged GDI engines. The viscosity of the diluted oil decreases with high temperature in combustion chamber, and the diluted oil can easily escape into the combustion chamber from the cylinder wall. Since oil typically has a high cetane number and its autoignition temperature is much lower than that of gasoline, the preignition of mixtures with oil in the late compression stroke occurs before spark ignition timing, inducing superknock. More researches are still needed for investigating injection impingement, interaction between fuel injection and oil film, and oil droplet's characteristics in combustion chambers of GDI engines.

Unlike GDI which can directly dominate engine combustion systems as a single combustion technology, Low Temperature Combustion (LTC) has mainly infiltrated into various combustion systems as a new combustion mode to reduce combustion temperature and improve combustion efficiency. LTC technology, which can work for both gasoline and diesel engines, has been widely studied in recent years due to advantages of low NO_x emission and simultaneously high efficiency. Early works on piston engines with LTC demonstrated that engine-out NO_x and PM emissions could be lowered to about 1–10% of conventional gasoline and diesel engine technologies. To implement LTC in diesel or gasoline engines, the control of ignition timing, which cannot be directly regulated as is the case in conventional internal combustion engines with fuel injection or spark ignition, must be dealt with. Because load is dependent on both the combustion phasing and the amount of reactant species present in the cylinder, both load and combustion phasing are therefore coupled and dependent on in-cylinder species concentrations, temperature, and pressure. Starting LTC with the previous cycle, a certain amount of residual gas should be trapped, while both air and EGR (Exhaust Gas Recirculation) in the correct proportions and at the right temperature must be added. Fuel is added in such a way that it evaporates and is then dispersed to support the premixed mode of combustion. Existing research results have suggested that VVA/VVT (Variable Valve Actuation/Variable Valve Timing) are effective for operating LTC mode, particularly for practically transient operating conditions. When VVA/VVT are employed, their effects on in-cylinder flows and the subsequent influences of these on air-mixing and ignition process become complicated and must be comprehensively examined for utilising the maximum benefit of LTC technology.

In terms of gas turbine aircraft engines, for achieving low emissions, low specific fuel consumption, and low cost of manufacture/maintenance, it is a great challenge for combustor design to reduce NO_x emission without negative effects on other performances of the combustor. Recent approaches for NO_x reduction had been presented including fuel staging, some applied combustors such as dual annular combustor, direct injection and Rich burn/Quick quench/Lean burn (RQL) and Lean Premixed and Prevaporized (LPP) combustion, and so on. For instance, premixer-prevaporizer combustor, which is a key technology for NO_x emission reduction, has been presented in the form of a number of different designs. One design is to use an air assisted pressure

swirl atomizer to atomize fuel, while a circular premixer was fitted at the end of the atomizer. Then swirl, which is necessary for flame stabilization, is created by axially oriented swirl vanes at the end of the premixer. Another LPP combustor design is to use a premixer-prevaporizer at main stage with a conventional injection used in pilot stage, and then it becomes a dual annular combustor. The LPP combustor structure for this design consisted of a swirl cup injection with a lengthened sleeve to form a LPP tube. Fuel-air mixing/preparation devices in aeroengines not only directly influence ignition process, lean blow-out, combustion efficiency, and fuel consumption but also have significant effects on emissions and exit temperature distributions. Swirl cups, whose main components normally include primary-swirler, Venturi, secondary-swirler, flare, and fuel nozzle, have been applied in many combustion systems. These technologies are currently under intensive investigation, including studies of flow fields, aerodynamics, spray structure and atomization, air-fuel mixing, combustion processes, and emissions.

Combustion processes in gas turbine engines are very sensitive to fluctuations of pressure, density, and temperature of the environment. Even slow changes of those quantities will affect the energy released according to rules that can be deduced from the behaviour for steady combustion. Combustion instabilities normally occur in frequency ranges such that genuine dynamical behaviour is significant. Any fluctuation in burning produces local changes in the properties of the flow. Then those fluctuations propagate in the medium and join the global unsteady field in the chamber. The dynamical response of the medium converts the local fluctuations into global behaviour. For various combustion systems and new combustion technologies, combustion instability is always one of the main challenges and significant attention must be paid to these details in flows and combustion.

The International Energy Agency estimates that biofuels can grow to as much as 30% of the world's road transport fuel mix by 2050. Such fuels will include biodiesel and synthetic diesel fuels from waste sources via processes such as Fisher Tropsch. In the same time-frame, alcohols such as bioethanol produced from nonfood sources with reduced production costs and low CO₂ emissions have been proposed as alternative fuels for direct blending with diesel, biodiesel, or synthetic diesel. According to Shell, one of main suppliers of biofuel, ethanol made from Brazilian sugar cane produces around 70% lower CO₂ emissions from production to use compared to gasoline. Therefore, following ethanol-gasoline blends and direct biodiesel, potentials of ethanol-diesel blends (e-diesel) as alternative fuel for low carbon advanced diesel engines have been studied by some researchers. It is likely that an increasingly diverse range of alternative biofuels, of varying molecular structure, will be utilised in the future as further emphasis is placed on sustainable production routes that result in reduced emissions of greenhouse gases (GHG) over the fuel production and usage lifecycle. These will likely contain molecules such as furans or terpenes from sources such as lignocellulosic biomass or genetically engineered microorganisms, and much research is still required so as to fully understand the impact of possible

future fuels such as these on ignition characteristics and the production of toxic pollutants.

In addition, it has been noticed that microexplosion may be exceedingly possible to occur during spray atomisation and combustion of fuel blends with differences of physical properties among the different fuels in the mixture. As one possible key phenomenon the understanding of which is necessary for using multicomponent fuels, microexplosion of a miscible multicomponent fuel droplet is due to the difference of volatility and boiling point among the different components. For an immiscible multicomponent fuel droplet (emulsion droplet as routinely termed), the likelihood of microexplosion will considerably increase if the lower-boiling-point component cannot dissolve in the mixture and disperse as microdroplets inside the fuel droplet, such as in the case of e-diesel as the volume fraction of bioethanol increases. Studies have shown that water emulsified in fossil fuels used in all combustion systems can lead to reductions in the adiabatic flame temperature, resulting in measurable reductions of NO_x emissions. Because of the difference in the evaporation rates of liquid diesel and water, the water molecules reached their superheated stage faster than the diesel, creating vapour expansion breakup. It is at this stage that the two phenomena, microexplosion and puffing, exist. Microexplosion is the rapid breakup of the emulsion droplets into smaller droplets, while, in puffing, water leaves the droplets in a very fine mist. These microexplosions result in a fast breakdown or secondary atomization of the fuel droplet, which, in turn, causes rapid fuel evaporation and, hence, leads to an improved air-fuel mixing. More studies on the preparation of emulsified water-fuel mixtures and multicomponent fuels and microprocessing of microexplosion and puffing under different operating conditions are necessary for applying the technology on practical engines.

As relevant researches have been moved to more detailed microresolutions including spatial and temporal ones during more complicated processes, various advanced optical diagnostics have been widely developed and applied for examining flows and combustion processes. Since flow fields, including their velocity distributions, temperature distribution, and species distributions, in both piston engines and gas turbines are at high level turbulent scales, optical particularly laser based diagnostic tools which bring no disturbance to the flow and reaction field are so helpful to measure and obtain information during detailed transient flow or combustion process inside combustion chambers. In addition to those more generally popular laser diagnostics such as nonspectroscopic PIV (Particle Image Velocimetry), LDA (Laser Doppler Velocimetry), PDA (Phase Doppler Anemometry), spectroscopic LIF (Laser Induced Fluorescence), and LII (Laser Induced incandescence), using X-ray Phase Contrast Imaging for investigating cavitation and gas ingestion in practical diesel injectors, DIH (Digital In-Line Holography) for microparticle characterisation, RS (Raman Scattering) for different species concentrations simultaneously, CARS (Coherent anti-Stokes Raman spectroscopy) for combustion species and temperature, TDLAS (Tuneable Diode Laser Absorption Spectroscopy) for species concentrations, and

MTV (Molecular Tagging Velocimetry) for velocity measurement in supersonic combustion has been recently reported.

Meanwhile, numerical simulation methods have also achieved significant development in recent years. Large Eddy Simulation (LES), in which the larger scales of turbulence are directly solved, where smaller scales are modelled using the subgrid models due to their isotropic characteristics, has been applied to engine combustion simulation in the last two decades. As LES is able to obtain more information of the turbulent flow field compared to RANS (Reynolds-Averaged Navier-Stokes) model, whilst less computational requirement is needed relative to DNS (Direct Numerical Simulation), LES has been expected to be the main way to model engine combustion.

Though the computational cost of DNS is very high and the computational resources required by a DNS for general combustion system will exceed the capacity of the most powerful computers currently available, it is still a useful tool in fundamental research in turbulent flows and combustion. Relevant "numerical experiments" by using 1D, 2D, and 3D DNS to complete simulation for premixed combustion have extracted required information which is difficult or impossible to obtain in the laboratory. This can allow a better understanding of the physics of turbulent flows and combustion. Meanwhile, DNS simulations are useful in the development of turbulence models for practical applications, such as subgrid scale models for LES and models for methods that solve RANS. This is done by means of "a priori" tests, in which the input data for the model is taken from a DNS simulation, or by "a posteriori" tests, in which the results produced by the model are compared with those obtained by DNS. DNS models and simulation methods will be definitely main research areas in the near future for turbulent flows and combustion, and it should be gradually able to provide significant help for new combustion system developments.

This edition is aiming to collect high-quality research articles and reviews that seek to address recent development on flow characteristics, air-fuel mixing, ignition and combustion processes, and emission reduction. Relevant prospects on opportunities and challenges for alternative fuels and novel combustion concepts have also been included with researches by both experimental works and numerical simulations.

*Zhijun Peng
Thanos Megaritis
Chih-Jen Sung
Minoru Yaga
Paul Hellier
Guohong Tian*

Research Article

Effects of Injection Rate Profile on Combustion Process and Emissions in a Diesel Engine

Fuqiang Bai,¹ Zuowei Zhang,¹ Yongchen Du,² Fan Zhang,¹ and Zhijun Peng^{2,3}

¹Key State Lab of Engines, Tianjin University, Tianjin, China

²School of Engineering and Technology, University of Hertfordshire, Hertfordshire, UK

³Faculty of Creative Arts, Technologies and Science, University of Bedfordshire, Luton, UK

Correspondence should be addressed to Zhijun Peng; jun.peng@beds.ac.uk

Received 3 February 2017; Accepted 7 May 2017; Published 21 June 2017

Academic Editor: Kalyan Annamalai

Copyright © 2017 Fuqiang Bai et al. This is an open access article distributed under the Creative Commons Attribution License, which permits unrestricted use, distribution, and reproduction in any medium, provided the original work is properly cited.

When multi-injection is implemented in diesel engine via high pressure common rail injection system, changed interval between injection pulses can induce variation of injection rate profile for sequential injection pulse, though other control parameters are the same. Variations of injection rate shape which influence the air-fuel mixing and combustion process will be important for designing injection strategy. In this research, CFD numerical simulations using KIVA-3V were conducted for examining the effects of injection rate shape on diesel combustion and emissions. After the model was validated by experimental results, five different shapes (including rectangle, slope, triangle, trapezoid, and wedge) of injection rate profiles were investigated. Modeling results demonstrate that injection rate shape can have obvious influence on heat release process and heat release traces which cause different combustion process and emissions. It is observed that the baseline, rectangle (flat), shape of injection rate can have better balance between NO_x and soot emissions than the other investigated shapes. As wedge shape brings about the lowest NO_x emissions due to retarded heat release, it produces the highest soot emissions among the five shapes. Trapezoid shape has the lowest soot emissions, while its NO_x is not the highest one. The highest NO_x emissions were produced by triangle shape due to higher peak injection rate.

1. Introduction

High pressure common rail (HPCR) fuel injection system have provided significant benefit for optimizing air-fuel mixing and controlling ignition, combustion, and emissions in diesel engines. With the aid of electronic controllers, HPCR system allows adjustment of injection pressure, fuel injection amount, injection timing, and injection pulse number in each combustion cycle very flexibly [1–3]. Then optimized injection strategies can improve diesel engine combustion for low combustion noise, high combustion efficiency, and low emissions [4, 5]. It can also provide postinjection for helping after-treatment system for regeneration. In recent years, as piezoinjectors are widely used for HPCR injection systems [6, 7]; injection timing and injection duration for each pulse can be controlled more precisely. Then multi-injection strategies are employed more and more for minimising emissions and fuel consumption.

When multi-injection strategies are employed, it has been realised that pressure waves that exist in HPCR system can result in significant effects on injection pressure and injection rate of sequent injection pulses [8, 9]. When an injection pulse is completed, then the injector valve is closed; a pressure wave inside the fuel pipe does oscillate between the injector valve and the common rail. Even the pressure in the rail is rather steady during an injection, there is still pressure wave induced by a close of injector valve. Then the actual injection pressure and injection rate of sequent injection pulse will be changed by the pressure wave [10, 11]. When the start timing of a sequent injection pulse is just at the peak of pressure wave, its injection pressure at the beginning will be higher than rail pressure. Otherwise, the injection pressure will be lower than the rail pressure. Then intervals between two adjacent injection pulses play very important role in managing the injection pressure and injection rate of sequent injection pulse.

Currently, most injection strategies for diesel engines are designed to avoid different injection pressure between injection pulses, in order to have simple control to combustion processes. However, this kind of arrangements may not be the best option for achieving optimal combustion and lowest emissions. Increased or reduced injection pressure and then varied injection rate and even injection rate shape for a sequent injection pulse may result in required improvement to air-fuel mixing and combustion rate under specific engine operation condition. For this issue, more investigations are still needed for achieving a clear idea how varied pressure, varied injection rate, and varied injection rate shape between injection pulses affect the combustion process and emissions.

Previous researches have suggested that effects of injection rates and their shape on air-fuel mixing and combustion processes are significantly important to organising diesel combustion [12, 13]. Suh [13] has conducted experiments on a high speed direct injection (HSDI) diesel engine for which compression ratio is 15.3 : 1 reduced from 17.8 : 1 by modification of combustion chamber shape to investigate the effects of the twin-pilot-injection strategies on combustion performance and exhaust emissions. The study shows lower NOx emissions (up to 45.7% were observed), whereas soot generation level was almost unaltered in the multiple-injection case. Desantes et al. [14] investigated the effects of boot-type rate shapes on engine performance and emissions. From their two-part study, they concluded that long boot length and low boot pressure decreased NOx emissions but increased brake specific fuel consumption (BSFC) and soot emissions. Moreover, they discovered that boot-type rate shapes caused substantial change to the diffusion combustion regime as compared to the premixed combustion regime.

There have been a number of researches for examining injection rate of HPCR system, in particular for those single injection pulse. Multiple injection still lacks adequate understanding of the injection rate with flexible injection interval, in particular with consideration of pressure wave's effects. The present research is applying CFD numerical simulation to examine how varied injection rate will affect combustion process and emissions in diesel engines. A full combustion model of diesel engine including submodels of fuel injection, evaporation, air-fuel mixing, combustion, and emissions was validated by required experimental results. Then combustion process and emissions were investigated by considering five injection rate shapes which are possibly produced by HPCR systems under influence of pressure wave. Simulation results provide an insight into effects of injection rate shapes on diesel combustion and emissions.

2. Numerical Model

2.1. Model Description. Numerical simulations were conducted by using KIVA-3V code [15], which was improved by introducing several submodels, as shown in Table 1. The submodels introduced have been tested by previous researchers [16] and it has been suggested that these new submodels are appropriate for diesel combustion. For resolving the turbulent flows in cylinder, the Renormalization Group (RNG) k - ϵ turbulence model [17] was used. The heat transfer from the

TABLE 1: Computational submodels.

Turbulent model	RNG k - ϵ model [17]
Breakup model	KH-RT model [19]
Collision model	Nordin model [20]
Splash model	Han et al. model [21]
Heat transfer (wall)	Han-Reitz model [18]
Combustion	CHEMKIN [22]
Fuel chemistry	Reduced N-Heptane mechanism [23]
Soot model	Phenomenological model [24]
NOx mechanism	Extended Zeldovich mechanism [24]

wall was computed by the model developed by Han and Reitz [18] which counted the variations of both gas density and the turbulent Prandtl number in the boundary layer.

The spray process was modeled by a particle method, where the breakup processes of injected droplets were simulated by a Kelvin-Helmholtz Rayleigh-Taylor (KH-RT) model [19]. The collision model used here was one developed by Nordin [20] with improved grid independence. The interaction between spray and wall was represented by the model introduced by Han et al. [21], which considered the effects of gas density variation in simulating the size of secondary droplets in splashing.

The CHEMKIN [22] solver was coupled with KIVA-3V code to compute the chemical reaction. A reduced n-heptane reaction mechanism [23] was used to simulate diesel fuel chemistry, where the soot formation was solved by a phenomenological model, and NOx formation was represented with extended Zeldovich mechanism. Simulation results [24] has shown fair agreements with experimental results that could be achieved when the simulating method was used.

2.2. Engine Specifications. The engine used in this numerical study was a HSDI (high speed direct injection) diesel engine, same as the one used for experimental investigation by Herfatmanesh et al. [9]. The engine has four valves and a displacement of 0.55 litre per cylinder. Most of the engine parameters were maintained the same as those used in original experiments for the model validation except for some modifications made on the injector for further combustion simulations. The specifications of the engine are listed in Table 2.

2.3. Computational Grid. Since the diesel injector used in the research has 6 equally distributed orifices, the combustion chamber was represented by a 60° sector grid with periodic boundary conditions, as shown in Figure 1. The grid for the cylinder volume at TDC (top dead centre) has approximately 25,231 hexahedral cells. The typical cell size is smaller than 3 mm in three dimensions, which is at the similar level used by Kim et al. [25]. Kim et al. also employed KIVA-3V for their simulation with grids ($2.2 \times 2.2 \times 3.0$ mm³) and their results have demonstrated adequate confidence of precision for combustion simulation. Therefore the grid used here is considered to yield reasonable accuracy for those predictions.

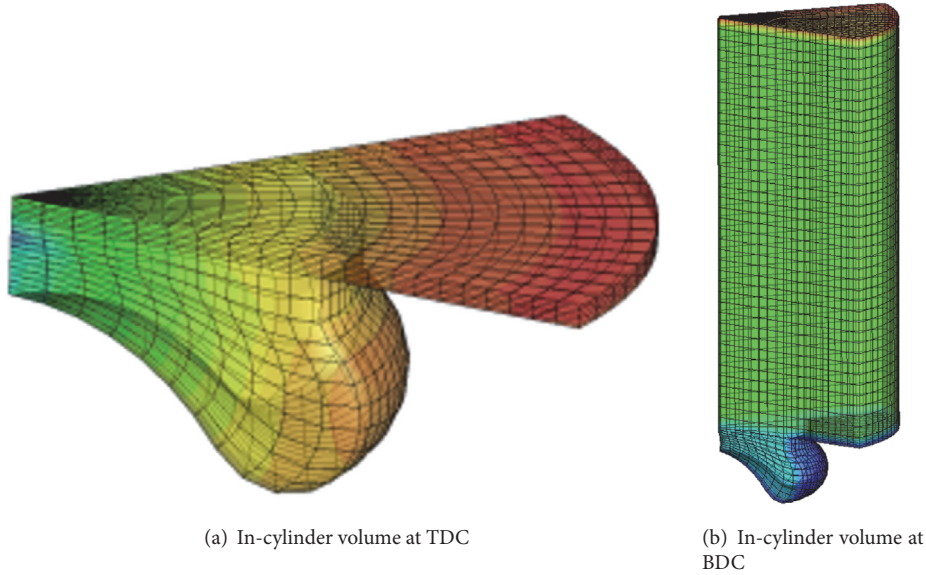


FIGURE 1: Computational mesh ((a) and (b) are not in same scale).

TABLE 2: Engine specifications for CFD simulation.

Parameter	Unit	Detail
Engine type		2.2L 4-cylinder turbocharged
Bore	mm	86
Stroke	mm	94.6
Valve number		4/cylinder
Compression ratio		18 : 1
Turbocharger		VGT
Fuel injection system		Common rail
Injector hole diameter	mm	0.12
Injector hole number		6/injector
Peak torque	Nm	360 @1500 rpm
Peak power	kW	155 @3800 rpm

2.4. Model Validation. The validation presented here was mainly combined with engine experimental results presented by previous researchers [16]. The fuel mass per cycle for the validation was 1 mg for pilot injection and 21 mg for main injection. The engine speed is 1800 rpm and the injection pressure is 180 MPa. Other operating conditions were maintained the same as described in [16]. Figure 2 shows the comparison of the in-cylinder pressure between the simulation and experimental results. From the figure, it can be observed that a good agreement has been achieved between experimental and simulation results. For emissions which are shown in Figure 3, both NO_x and soot emissions have been compared between experimental results and simulation by

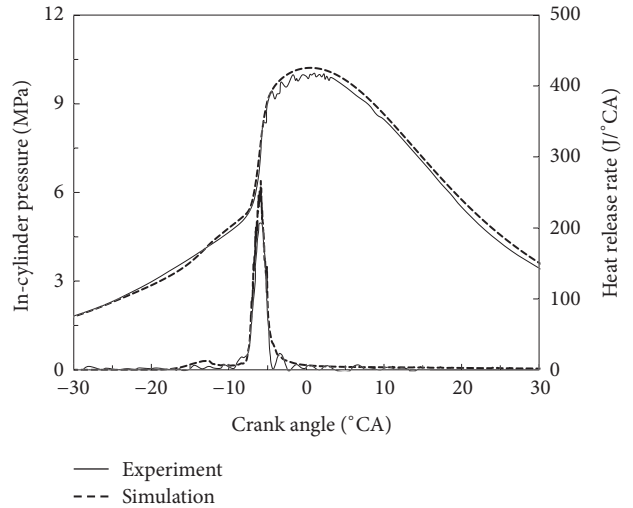


FIGURE 2: Comparison of in-cylinder pressure traces between experimental results and simulation.

varying the main injection timing. Those results show that the model can predict emissions with necessary accuracy.

3. Simulation Conditions

Previous experimental investigation has demonstrated that the sequential injection pulse can have very different injection rate profile. While other parameters are constant, increasing interval between injection pulses can result in the injection rate shape of sequential pulse gradually becoming more flat. The injection rate shape of sequent pulse for interval that increased from 750 μ s to 2500 μ s is very different, as shown in Figure 4.

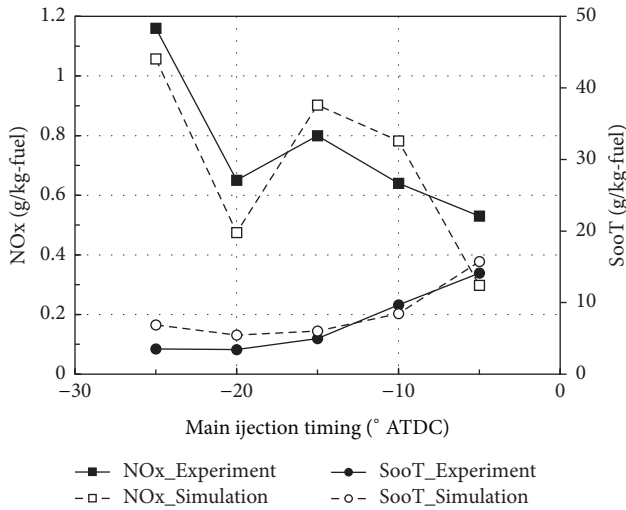


FIGURE 3: Comparison of NOx and soot emissions between experimental results and simulation.

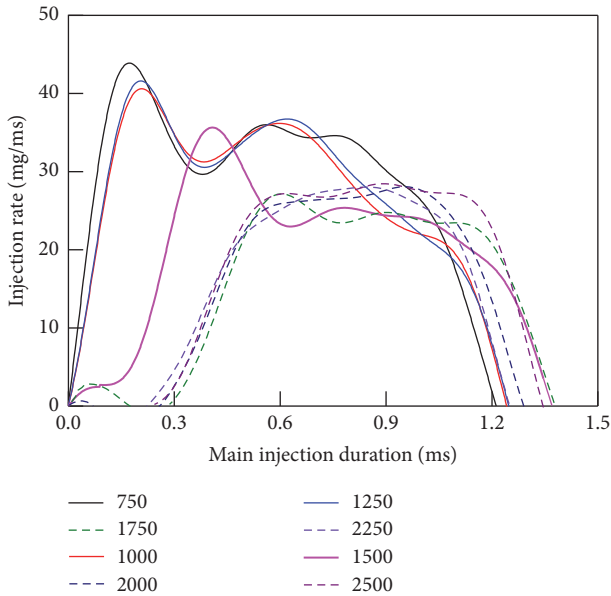


FIGURE 4: Experimental results of injection rates of second injection pulse (pulse width of 600μ s– 600μ s, interval shown in the figure, 80 MPa injection pressure).

It can be seen in Figure 4 that average injection rates for different injection intervals are very different. With the increase of interval, the average injection rate keeps decreasing, in particular from 1250 to 1500 and then to 1750 μ s. Those injection rates of intervals less than 1250 μ s have similar trend and shape. They have a high peak at the start point and then second low peak after some reduction. The final stage has a smooth decreasing slope. The injection rate of 1500 μ s has some delay at the beginning and then displays similar trend as those of less than 1250 μ s. After the interval increases over 1750 μ s, all traces of injection rates have very similar profile, after a longer delay than that of 1500 μ s, then having very slow

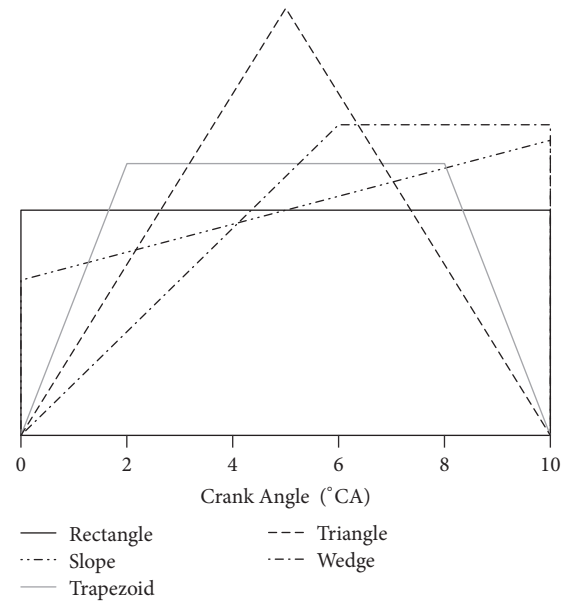


FIGURE 5: Different injection rate shape used for CFD simulation.

increase and long and flat persistence and finally decreasing quickly.

Considering practical injection rate shape's variation, in this research, five different injection rate shapes were selected to investigate the effects. As shown in Figure 5, among the five different injection rate shapes, the total fuel amount, pulse width, and average injection rate are maintained the same. While the rectangle shape has totally flat injection rate, the slope one has smooth increase across all pulse, and the wedge one has a little more steep increase at the beginning and then keeps flat at late stage. The triangle shape consists of only an increase stage and then a decrease stage with highest peak rate at the middle point. The trapezoid has the faster increase at beginning and fast decrease at finish stage but has some flat stage in between.

Although those shapes are considered here more for theoretical analysis, resemblant profiles may be produced under certain injection conditions, in particular, the trapezoid which is more close to most practical injection rate profiles. In order to study the effect of injection rate shapes, it was assumed that all the fuel was injected before TDC with the injection timing at 8.6° CA BTDC. The fuel amount is 49.2 mg.

4. Result and Discussions

4.1. Effects on Combustion Process and Heat Release Rate. The in-cylinder pressure traces and heat release rate traces for five cases are presented in Figure 6. As the rectangle one has the highest injection rate at the start point, its ignition timing is the earliest one and at the beginning its heat release rate has a faster increase than other shapes. As the triangle one has the highest injection rate close to TDC, it produces the highest heat release rate near TDC.

During late stage of combustion, as the rectangle one and slope one do not get further increase too much of injection

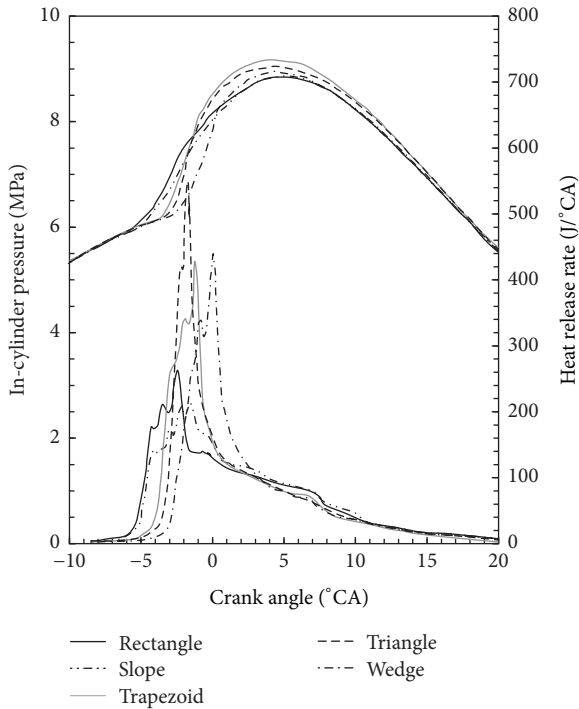


FIGURE 6: Simulated in-cylinder pressure traces and heat release rate traces for five different injection rate shapes.

rate, increases in heat release rates are not so obvious compared to other three shapes. The wedge one has a later peak at late stage because of its highest injection rate for a long time at the late injection stage.

Basic process can be analysed by inspecting the in-cylinder temperature distribution. The results at four different crank angles are shown in Table 3. At the beginning and late stage of fuel injection is shown that in-cylinder temperature distributions are very similar for all the five shapes. But by the mid-stage combustion (about 5°CA ATDC), triangle and trapezoid have obviously bigger areas of high temperature than other three shapes. This may be due to the higher injection rate during middle injection stage for those two shapes.

At the late stage of combustion (such as 10°CA ATDC as shown in Table 3), all five have similar temperature distribution, although wedge has the smallest area of high temperature (red colour) and slope has the smallest area of mid-high temperature (yellow colour). In Table 3, it can be observed that slope and wedge shapes have still obvious fuel spray at TDC, while other shapes' injection have almost totally stopped. This may be due to higher injection rate at late injection stage for slope and wedge shape.

By analysing the in-cylinder temperature traces from in-cylinder pressure traces for five shapes, from results as shown in Figure 7, it can be observed that they are consistent with information shown in Table 3. Although the initial temperature increase did not take place too early for trapezoid and triangle shapes, their temperatures increase very rapidly and maintain high values than other three shapes. For wedge shape, its temperature is not so high although its peak value of

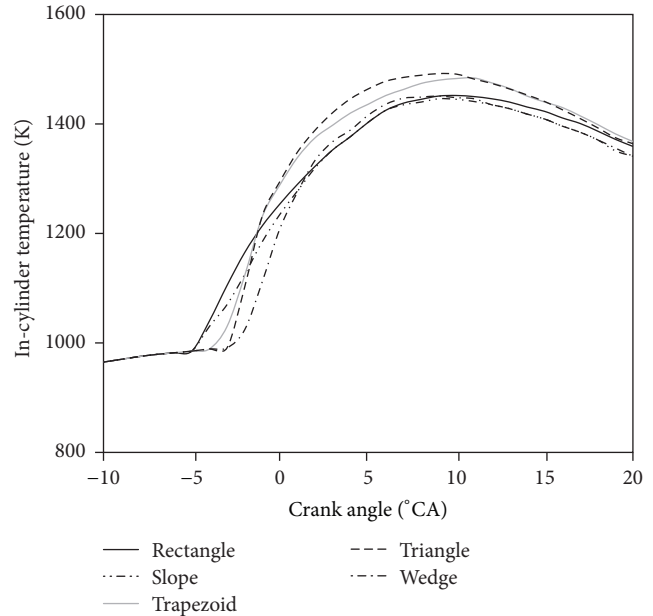


FIGURE 7: Simulated in-cylinder temperature for five different injection rate shapes.

heat release is about twice higher than that of rectangle shape. The main reason may be that its most heat release takes place at a later stage compared to the other shapes.

4.2. Effects on Emissions. Based on the difference of in-cylinder peak temperature (as shown in Figure 7), the triangle shape shows the highest NOx emissions and the wedge shows the lowest NOx emissions, as shown in Figure 8. A special point is that the rectangle shape has lower peak temperature than the slope one, but its NOx emissions are higher. By checking the in-cylinder temperature distributions of two shapes (as shown in Table 3), it can be observed that the high temperature area of the rectangle shape is bigger than the slope one at the crank angle where the combustion will be completed.

Soot and NOx emissions as shown in Figure 9 basically show their relation as trade-off. But triangle one which has the highest NOx emissions does not follow the trend to have lowest soot emissions. By reviewing the heat release rates, it can be seen that its peak heat release rate is too early compared to the others. The reason for the more soot emissions is that a lot of fuel was injected due to the highest injection rate. Hence, a liquid film may be formed inside the piston bowl as shown in Table 3. If both NOx and soot emissions are considered as important factors, the rectangle shape can have better compromise between them, while the triangle shape is the worst case. For practical applications, this means that high peak in injection rate shape should be avoided.

Figure 10 shows the results of CO and HC emissions. For triangle shape, because it has the highest in-cylinder temperature, its HC emissions are the lowest one. But its CO emissions are the highest one. This may be due to the poor air-fuel mixing while most fuel is injected during middle stage

TABLE 3: In-cylinder temperature distributions at 8°CA BTDC, TDC, 5°CA ATDC, and 10°CA ATDC for five different injection rate shapes.

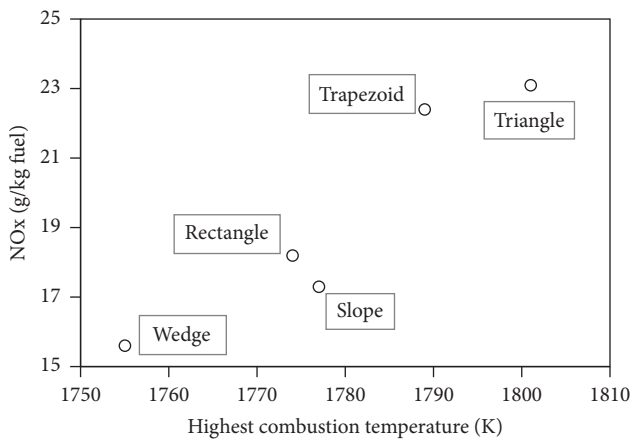
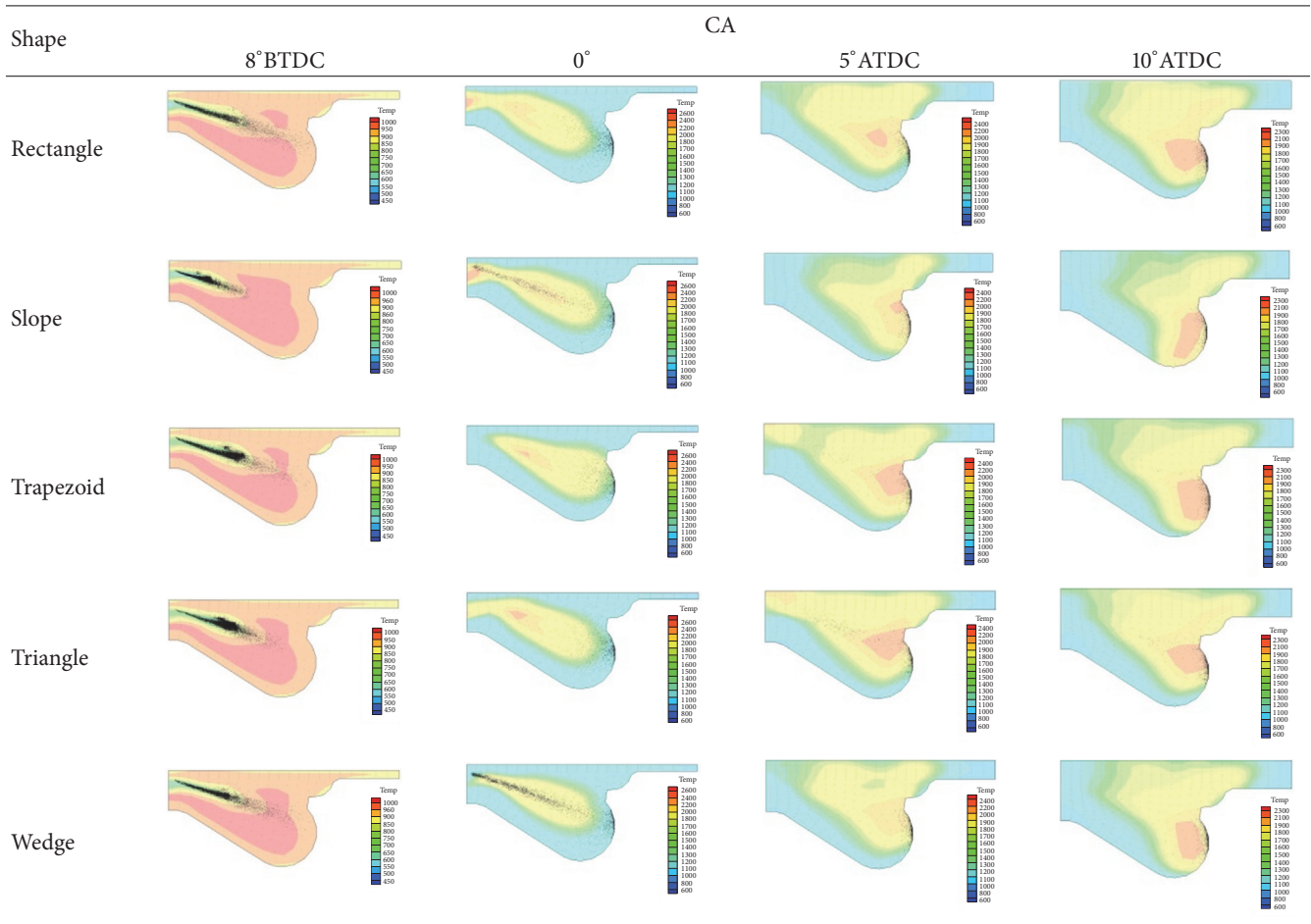


FIGURE 8: Simulation results of NOx emissions for five different injection rate shapes.

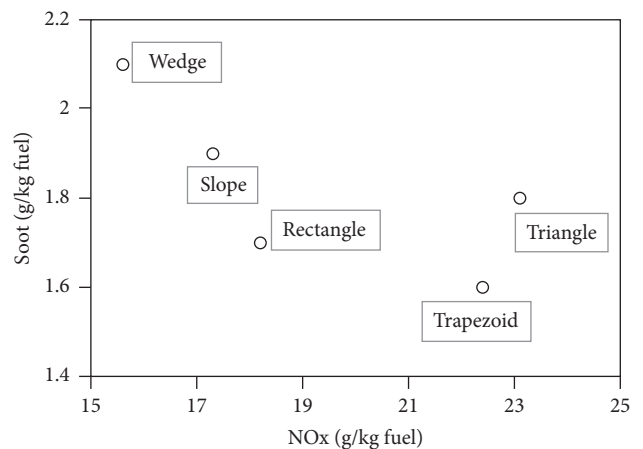


FIGURE 9: Simulation results for soot and NOx emissions of five different injection rate shapes.

with very high injection rate. The wedge shape has also very high CO emissions since it has high injection rate at the late injection stage. Its HC emissions are the highest one. This is obviously due to its low combustion temperature. Slope and rectangle have low CO emissions but high HC emissions. This

may be because their injection rates are flat compared to the other shapes. In the one hand, the flat injection rate may result in better mixing, then producing lower CO emission. On the other hand, their low combustion temperatures contribute to high HC emissions. It can be noticed that slope has both lower

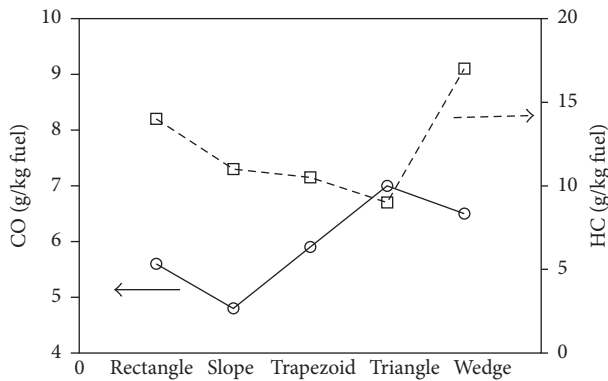


FIGURE 10: Simulation results for CO and HC emissions of five different injection rate shapes.

CO and HC emissions than rectangle shape. This suggests slow increase of injection rate can benefit both HC and CO emissions, compared to totally flat injection rate.

Having this set of simulations suggests that different injection rate shape for individual injection pulse can also have influence on combustion process and emissions. The rectangle shape can have better balance between NO_x and soot emissions, because other shapes with higher injection rate at some point (temporal) will result in higher NO_x or soot emissions.

5. Conclusions

In the research work presented, influences of variations of injection rate shape caused by different injection intervals were examined by numerical simulation based on KIVA-3V CFD code. From the results, the following conclusions have been derived:

- (i) Injection rate shape has an influence on diesel combustion process, in-cylinder mixing, heat release rate, and in-cylinder temperature distribution. The triangle shape has the highest peak combustion temperature due to too high injection rate at some injection point. The wedge shape's combustion temperature is the lowest across most combustion stages due to its late ignition timing.
- (ii) Rectangle shape can have better balance between NO_x and soot emissions, while other shapes with higher injection rate at some point (temporal) will result in higher NO_x or soot emissions.
- (iii) The triangle shape produces the highest NO_x emissions due to the highest combustion temperature. The trapezoid shape shows the lowest soot emissions due to both better mixing and high combustion temperature.
- (iv) The slope shape has the lowest CO emissions and not very high HC emissions. Regarding CO and HC emissions, it is better than rectangle shape.

Acronyms

ATDC:	After top dead centre
BTDC:	Before top dead centre
CA:	Crank angle
CFD:	Computational fluid dynamics
CO:	Carbon monoxide
EOI:	End of injection
HC:	Hydrocarbon
HPCR:	High pressure common rail
HRR:	Heat release rate
HSDI:	High speed direct injection
NO _x :	Nitrogen oxides
PM:	Particulate matters
TDC:	Top dead centre.

Conflicts of Interest

The authors declare that there are no conflicts of interest regarding the publication of this paper.

References

- [1] J. Hinkelbein, C. Sandikcioglu, S. Pischinger, M. Lamping, and T. Körfer, "Control of the Diesel Combustion Process via Advanced Closed Loop Combustion Control and a Flexible Injection Rate Shaping Tool," *SAE Technical Paper*, vol. 24, article 0114, 2009.
- [2] X. Li, H. Zhou, L. M. Zhao, L. Su, H. Xu, and F. Liu, "Effect of split injections coupled with swirl on combustion performance in DI diesel engines," *Energy Conversion and Management*, vol. 129, pp. 180–188, 2016.
- [3] P. Dimitriou, Z. Peng, W. Wang, B. Gao, and M. Wellers, "Effects of advanced injection strategies on the in-cylinder air-fuel homogeneity of diesel engines," *Proceedings of the Institution of Mechanical Engineers, Part D: Journal of Automobile Engineering*, vol. 229, no. 3, pp. 330–341, 2015.
- [4] B. Rohani and C. Bae, "Effect of exhaust gas recirculation (EGR) and multiple injections on diesel soot nano-structure and reactivity," *Applied Thermal Engineering*, vol. 116, pp. 160–169, 2017.
- [5] A. Gharehghani, S. M. Mirsalim, and S. A. Jazayeri, "Numerical and experimental investigation of combustion and knock in a dual fuel Gas/Diesel compression ignition engine," *Journal of Combustion*, vol. 2012, Article ID 504590, 10 pages, 2012.
- [6] H. Nouraei, R. Ben-Mrad, and A. N. Sinclair, "Development of a Piezoelectric Fuel Injector," *IEEE Transactions on Vehicular Technology*, vol. 65, no. 3, pp. 1162–1170, 2016.
- [7] J. Kim, J. Kim, S. Jeong, S. Han, and J. Lee, "Effects of different piezo-acting mechanism on two-stage fuel injection and CI combustion in a CRDi engine," *Journal of Mechanical Science and Technology*, vol. 30, no. 12, pp. 5727–5737, 2016.
- [8] A. E. Catania, A. Ferrari, M. Manno, and E. Spessa, "Experimental investigation of dynamics effects on multiple-injection common rail system performance," *Journal of Engineering for Gas Turbines and Power*, vol. 130, no. 3, Article ID 032806, 2008.
- [9] M. R. Herfatmanesh, Z. Peng, A. Ihracska, Y. Lin, L. Lu, and C. Zhang, "Characteristics of pressure wave in common rail fuel injection system of high-speed direct injection diesel engines," *Advances in Mechanical Engineering*, vol. 8, no. 5, pp. 1–8, 2016.
- [10] J. Baumann, U. Kiencke, T. Schlegel, and W. Oestreicher, "Practical feasibility of measuring pressure waves in Common Rail

- injection systems by magneto-elastic sensors," *SAE Technical Papers*, vol. 1, article 0891, 2006.
- [11] A. De Risi, F. Naccarato, and D. Laforgia, "Experimental analysis of common rail pressure wave effect on engine emissions," *SAE Technical Papers*, vol. 1, article 0373, 2005.
- [12] C. Y. Choi and R. D. Reitz, "Modeling the effects of oxygenated fuels and split injections on DI diesel engine performance and emissions," *Combustion Science and Technology*, vol. 159, no. 1, pp. 169–198, 2000.
- [13] H. K. Suh, "Study on the twin-pilot-injection strategies for the reduction in the exhaust emissions in a low-compression-ratio engine," *Proceedings of the Institution of Mechanical Engineers, Part D: Journal of Automobile Engineering*, vol. 228, no. 3, pp. 335–343, 2014.
- [14] J. M. Desantes, J. Benajes, S. Molina, and C. A. González, "The modification of the fuel injection rate in heavy-duty diesel engines. Part 1: Effects on engine performance and emissions," *Applied Thermal Engineering*, vol. 24, no. 17-18, pp. 2701–2714, 2004.
- [15] A. Amsden, "KIVA-3V: A block-structured KIVA program for engines with vertical or canted valves," Technical Report for Los Alamos National Laboratory LA-13313-MS, Los Alamos, NM, USA, 1997.
- [16] Z. Peng, B. Liu, W. Wang, and L. Lu, "CFD investigation into diesel PCCI combustion with optimized fuel injection," *Energies*, vol. 4, no. 3, pp. 517–531, 2011.
- [17] Z. Han and R. D. Reitz, "Turbulence modeling of internal combustion engines using RNG k-e models," *Combustion Science and Technology*, vol. 106, no. 4, pp. 267–276, 1995.
- [18] Z. Han and R. D. Reitz, "A temperature wall function formulation for variable-density turbulent flows with application to engine convective heat transfer modeling," *International Journal of Heat and Mass Transfer*, vol. 40, no. 3, pp. 613–625, 1997.
- [19] L. M. Ricart and R. D. Reitz, "Comparisons of diesel spray liquid penetration and vapor fuel distributions with in-cylinder optical measurements," *Journal of Engineering for Gas Turbines and Power*, vol. 122, no. 4, pp. 588–595, 2000.
- [20] N. Nordin, *Complex chemistry modeling of diesel spray combustion. Thesis [Ph.D. thesis]*, Chalmers University of Technology, Goteborg, Sweden, 2001.
- [21] Z. Han, Z. Xu, and N. Trigui, "Spray/wall interaction models for multidimensional engine simulation," *International Journal of Engine Research*, vol. 1, no. 1, pp. 127–146, 2000.
- [22] R. Kee, F. Rupley, E. Meeks, and J. Miller, "CHEMKIN-III: A FORTRAN chemical kinetics package for the analysis of gas-phase chemical and plasma kinetics," Technical Report for Sandia National Laboratories SAND96-8216, Albuquerque, NM, USA, 1996.
- [23] A. Patel, S.-C. Kong, and R. D. Reitz, "Development and validation of a reduced reaction mechanism for HCCI engine simulations," *SAE Technical Papers*, vol. 1, article 0558, 2004.
- [24] M. Jia, Z.-J. Peng, and M.-Z. Xie, "Numerical investigation of soot reduction potentials with diesel homogeneous charge compression ignition combustion by an improved phenomenological soot model," *Proceedings of the Institution of Mechanical Engineers, Part D: Journal of Automobile Engineering*, vol. 223, no. 3, pp. 395–412, 2009.
- [25] Y.-J. Kim, S. H. Lee, and N.-H. Cho, "Effect of air motion on fuel spray characteristics in a gasoline direct injection engine," *SAE Technical Papers*, vol. 1, article 0177, 1999.

Research Article

Small Engines as Bottoming Cycle Steam Expanders for Internal Combustion Engines

Rohitha Weerasinghe and Sandra Hounsham

Department of Engineering, Design and Mathematics, University of the West of England, Coldharbour Lane, Bristol BS16 1QY, UK

Correspondence should be addressed to Rohitha Weerasinghe; sujithrohitha@yahoo.com

Received 16 January 2017; Revised 4 April 2017; Accepted 20 April 2017; Published 31 May 2017

Academic Editor: Paul Hellier

Copyright © 2017 Rohitha Weerasinghe and Sandra Hounsham. This is an open access article distributed under the Creative Commons Attribution License, which permits unrestricted use, distribution, and reproduction in any medium, provided the original work is properly cited.

Heat recovery bottoming cycles for internal combustion engines have opened new avenues for research into small steam expanders (Stobart and Weerasinghe, 2006). Dependable data for small steam expanders will allow us to predict their suitability as bottoming cycle engines and the fuel economy achieved by using them as bottoming cycles. Present paper is based on results of experiments carried out on small scale Wankel and two-stroke reciprocating engines as air expanders and as steam expanders. A test facility developed at Sussex used for measurements is comprised of a torque, power and speed measurements, electronic actuation of valves, synchronized data acquisition of pressure, and temperatures of steam and inside of the engines for steam and internal combustion cycles. Results are presented for four engine modes, namely, reciprocating engine in uniflow steam expansion mode and air expansion mode and rotary Wankel engine in steam expansion mode and air expansion mode. The air tests will provide base data for friction and motoring effects whereas steam tests will tell how effective the engines will be in this mode. Results for power, torque, and p - V diagrams are compared to determine the change in performance from air expansion mode to steam expansion mode.

1. Introduction and Motivation

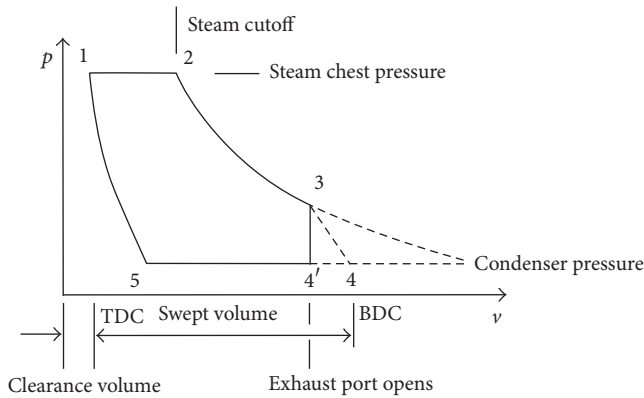
Finding a suitable bottoming cycle for recovery of low grade heat recovered from an internal combustion engine is based on the temperature range of operation and the expected efficiency. Thermoelectric heat recovery provides a relatively cleaner less complicated option, but with very low efficiency. Steam on the other hand has been proven to work in heat recovery cycles with a decent efficiency range. Thomas Newcomen's atmospheric engine, today referred to as the Newcomen engine, was the first practical device that harnessed power of steam to produce mechanical work. James Watt developed it further and steam reciprocating engines have been in use for the last 200 years [1]. The use of steam engines has diminished in the advent of the internal combustion engine and the electric motor. However, steam engines are still being used in various engineering applications, especially in the power generation industry. Small steam expansion engines are in limited use [2]; this is usually because a steam generating system is also required which makes them uneconomical. There have been attempts to use steam expanders

as primary power plant of an automobile [3]; however the present work is based on steam small engines as bottoming cycle expanders. There has not been much research done in this area. Particularly, there are no data available on performance of these engines. The work is intended to provide a platform for the development of small steam engines that can be used as bottoming cycle heat expanders. There are various options as steam expanders, for example, vane rotors and microturbines. However, reciprocating expanders and Wankel engines are readily available as small engines that can be converted into steam expanders. The range of the engines in the study has been limited by the size and power that can be mounted on the test apparatus, a table-top dynamometer. Essentially, the range has been restricted to less than 20 cc cylinder capacity. The primary parameters of the two engines that have been used in the study are listed in Table 1.

1.1. The Rankine Cycle. The steam engine generally operates on the Rankine thermodynamic cycle. Rankine cycles [4] have been widely used in both prime movers and bottoming

TABLE I: Engine data.

Engine	Four stroke reciprocating engine	Wankel rotary engine
Model	OS 32 SX	OS 49 PI
Bore (mm)	19.5	N/A
Stroke (mm)	17.5	N/A
Capacity (cc)	5.23	4.97
Compression ratio	10:1	7:1 (approx.)

FIGURE 1: Rankine cycle reciprocating expander P - V diagram.

cycle expanders. The reciprocating Rankine cycle has been used in locomotives, ships, and stationary engines. Rotary expanders, primarily, steam turbines, are used in power generation. The use of rotary engine has been restricted by the optimum operating range it offers in comparison to the wide range offered by the reciprocating engine. The use of the steam expander used in this study is mainly aimed as a directly coupled engine that can operate in sync with an internal combustion engine. A reciprocating engine offers similar torques power characteristics to an IC engine. The other main advantage is the availability of small engines that can be converted into steam expanders.

1.1.1. Rankine Cycle with a Reciprocating Expander. A reciprocating Rankine cycle shown in Figure 1 is explained by the following steps:

- (1-2) Admission of steam at steam chest pressure.
- (2-3) Expansion of steam until the exhaust port is open.
- (3-4') Blow down of the steam to condenser pressure.
- (4-5) Exhaust of steam until the exhaust port is closed.
- (5-1) Compression of steam left in the cylinder.

The work and heat for the cycle can be found done by obtaining the specific enthalpies h_n , where n refers to steps in Figure 1. The theoretical work by the cycle is given by $h_2 - h_3$

and the heat supplied is given by $h_2 - h_1$. The efficiency is given by

$$\eta = \frac{(h_2 - h_3)}{(h_2 - h_1)}. \quad (1)$$

The pump work is neglected as it is small compared to the heat in. Reciprocating steam expanders were the most common type of expanders, known for their high torque and simple operation. These are mostly used as marine and old locomotive prime movers. The speed achievable from large steam engines is limited. Uniflow and counter-flow arrangements are possible with reciprocating expanders [1]. However, the valve arrangements become more complex with counter-flow arrangement [5]. Reciprocating engines are perceived to be easier to implement than Wankel engines [6].

1.1.2. Rotary Steam Engines. Steam turbines are efficient devices, but the range of operation is limited, hence not very suitable for automotive applications. The major attraction of the turbine cycle is the high overall efficiency in operation. However the flexibility of operation outweighs the efficiency factor and makes the reciprocating Rankine cycle more practical. In addition, the ability to cater to fluctuating torque and velocity conditions of the reciprocating cycle makes it the preferred device for automotive applications. Nevertheless, if the energy developed in a turbine is converted into electricity and used to drive an electric motor it leads to a practical solution for hybrid vehicles [7].

An intermediate solution is the Wankel rotary expander [8]. Wankel engine offers some advantages of both the turbine cycle and the flexibility of the reciprocating engine [9, 10]. Micro-Wankel engines can be fabricated with improved fabrication technology [11]. Attempts have been made to correctly emulate the operation of the Wankel engine [12], but the current application is using steam as the working fluid without internal combustion. Figure 2 shows the theoretical Rankine cycle and the pressure volume diagram of a Rankine cycle.

1.2. Waste Heat Recovery. The major attraction of Rankine cycle [13] today is its applicability in the waste heat recovery systems [12]. In power generation, Rankine turbines are driven by steam generated through waste heat recovery. Use of reciprocating engines in waste heat recovery systems is seldom. On the other hand, use of rotary steam engines in small scale applications is not common. Ability of Rankine cycle to operate on low grade heat sources such as steam makes it attractive to employ in a bottoming cycle [14]. Two main types of expanders have been applied in Rankine cycle applications that are of two types: first one is the velocity type, such as axial turbines and radial-flow turbines; the other is positive displacement type, such as scroll expanders, screw expanders, piston expanders, and rotary vane expanders [15]. These expanders feed off a steam reservoir courtesy of heat recovery in a bottoming cycle [16, 17].

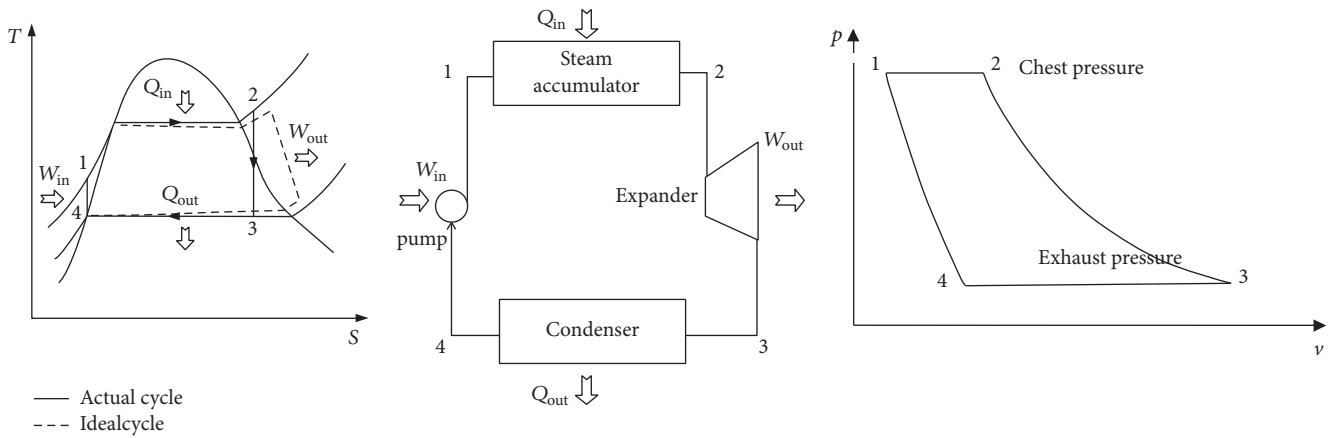


FIGURE 2: A simple Rankine cycle and Wankel Rankine expander P-V diagram.

2. Experimental Setup

The experimental setup consists of a dynamometer, a data acquisition system controlled by LabVIEW software, a steam/air supply, and a condenser unit. The sensor inputs are fed to the system through a multichannel data acquisition card. Figure 3 shows the components of the system and how they are linked.

2.1. The Dynamometer. Testing of small scale engines offer the advantages of portability, less instrumentation, low space costs, and flexibility. However there are no readily available dynamometer setups for testing small engines. Hence, a small scale dynamometer facility pictured in Figure 4 had to be developed to mount the small engines for testing. The dynamometer was derived from a model makers’ lathe and the drive train was modified to absorb power and to motor when necessary. The engine output shaft is mounted inline with the lathe shaft. Torque transducer arrangement connects the engine output shaft and the lathe shaft. A 400 WDC motor drives the main shaft that can also absorb power. The end of the drive shaft is fitted to a pulse encoder that generates three pulse streams, namely, (i) pulse per revolution (ppr), (ii) pulse per revolution -90° (directional indicator), and (iii) pulse per crank angle degree (pcd).

The engines used were modified model hobby engines manufactured by OS (Japan). The following data are available of the engines used.

For the use as steam expanders, the inlets and exhausts had to be modified to induct and exhaust steam. The engine heads were modified to accommodate for steam connections.

Figure 4 shows a schematic of how the steam induction and exhaust connections and valves are configured. The picture shows the configuration of the ports controls and steam in and out. The arrangement is the same for the rotary engine except for the fact that the rotary engine has two inlet valves and two exhaust valves. The opening and closing of the rotary engine valves take place without electronic control.

2.2. Steam Expanders. Steam expanders are available in the form of reciprocating expanders and rotary expanders. In the

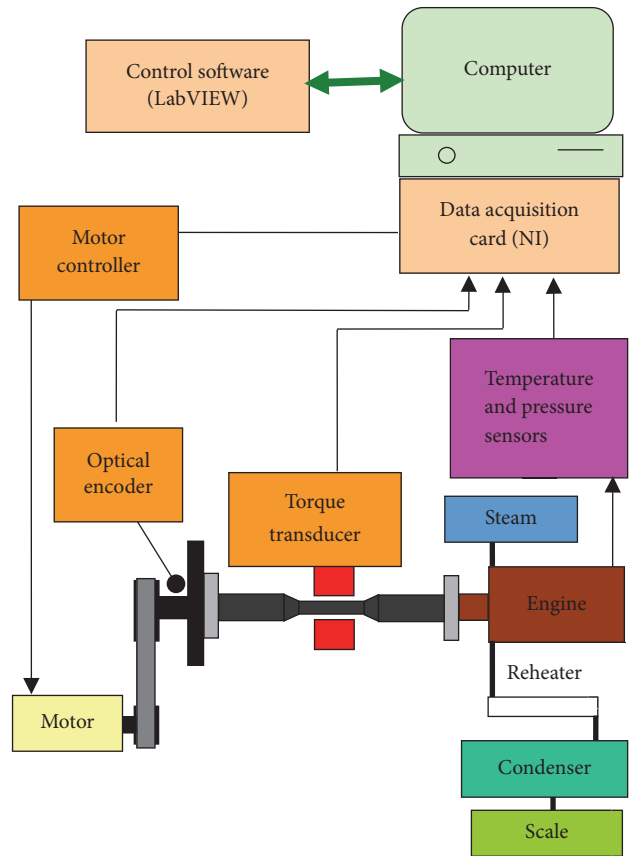


FIGURE 3: The experimental setup.

present context uniflow reciprocating expander and a rotary Wankel engine are tested.

2.2.1. Reciprocating Steam Engine. A two-stroke internal combustion engine has been modified to accommodate steam admission through an electrically operated overhead valve. An automotive fuel injection valve has been modified for the purpose. The steam enters through an electrically

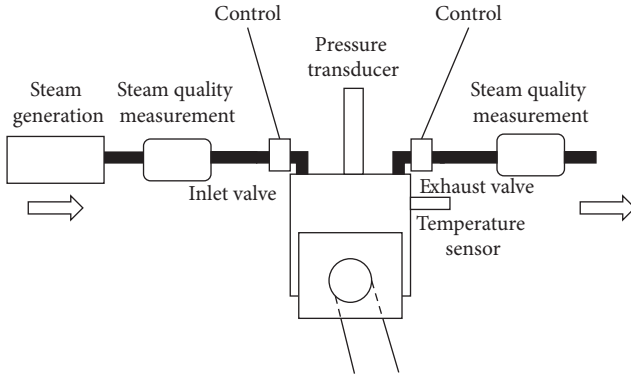


FIGURE 4: Schematic of the cylinder arrangement.

operated inlet valve and exhausts through a port at the BDC. The timing of steam admission is critical for propulsion. The valve timing was set to 3° BTDC and kept for 100° for the inlet valve. Exhaust takes place through a 6 mm long 25 mm wide port before BDC.

2.2.2. Valve Arrangement for the Two-Stroke Reciprocating Engine. Two pulse streams are utilized from the optical encoder by the data acquisition card, the pulse per revolution (ppr), and the pulse per crank angle degree (pcd). The ppr pulse is aligned with the top dead centre of the piston. LabVIEW software that controls the actuation of the valve and samples the data for storage uses the pcd pulse as a source of clock ticks and ppr pulse as a trigger for an output pulse. The timing of the valve actuation is synchronized with pcd pulse and is variable.

2.2.3. Wankel Steam Engine. A modified small scale internal combustion Wankel engine is used as a steam expander. The flow through the Wankel engine is uniflow, and continuous generation of torque is available with three expansions per cycle of the rotor. The P - v diagram for a Wankel Rankine cycle is not available in the literature. However, Figure 9 shows a pressure plot drawn against the crank angle as that is more appropriate than a P - v diagram. A 5 cm^3 model Wankel engine has been modified to run as a Wankel steam expander. There are two inlet ports and two exhaust ports. They were changed to obtain optimum performance. The inlet port is at 20° to the original line of the engine and the exhaust valves have been changed to a side exhaust arrangement as in Figure 5.

2.3. Instrumentation and Measurements. The engine is supplied with air or steam as appropriate and the fluid flow rate is controlled electronically. Measurements were taken at two set pressures of 7 bars and 15 bars for air and steam, respectively. Pressure, temperature, torque, speed, and pulse signals are fed through the National Instruments (NI) data acquisition card to the computer. Communication with the scales takes place via an RS232 connection. All the data acquisition and control are performed using LabVIEW software. The sampling was triggered by the pulse per crank angle degree (pcd) pulse from the optical encoder.

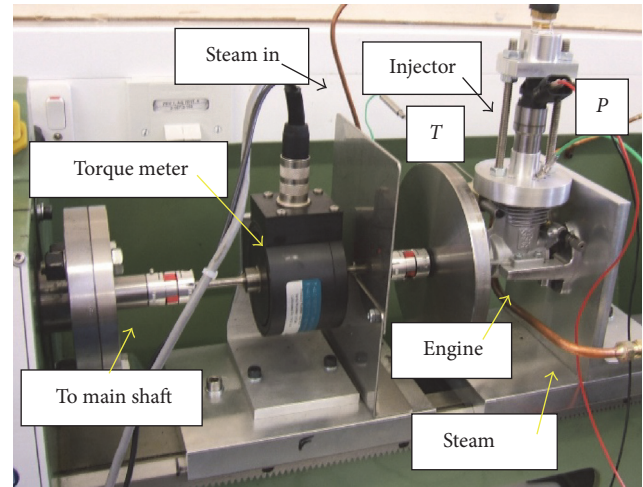


FIGURE 5: The dynamometer with the reciprocating engine mounted; P = pressure sensor; T = thermocouple.

2.3.1. Pressure. Pressure measurements were acquired for the engine inlet, engine outlet, inside of the cylinder, reheater inlet, and reheater outlet via piezoelectric pressure sensors.

2.3.2. Temperature. The temperatures at engine inlet, engine outlet, inside of the engine, reheater inlet, and reheater outlet were acquired using K type thermocouples.

2.3.3. Torque and Speed. Torque and speed are obtained via the inline torque transducer, from these readings power is given by

$$P = 2\pi NT. \quad (2)$$

2.3.4. Mass Flow Rate. The condensate from the engine is collected in a vessel on the electronic scales. The incremental weight against time gives the mass flow rate.

2.3.5. Steam Quality. The analysis of the steam quality of the exhausted steam required a new device setup. The steam coming out of the engine is wet and hence, the pressure and temperature alone would not give the steam condition. A reheater section is fitted to the exhaust pipes which brings the steam to a superheated condition at which the pressure and temperature alone would be able to give the state of the steam. Figure 6 shows the temperature and pressure tapping point and Figure 7 shows the steam quality analyzer.

Pressure and temperature sensors are placed at the input to the SQA (ri) and the exit point from the SQA (re). The readings are used to obtain the specific enthalpy h_{re} at re from steam tables. Then, h_{ri} is given by

$$h_{re} - h_{ri} = \frac{VI t}{M}, \quad (3)$$

where M is the mass of water collected in time t . VI is the recorded voltage and current used by the reheater section. The most important measurements of the system are the pressures and temperatures of the inlet, outlet, and inside of

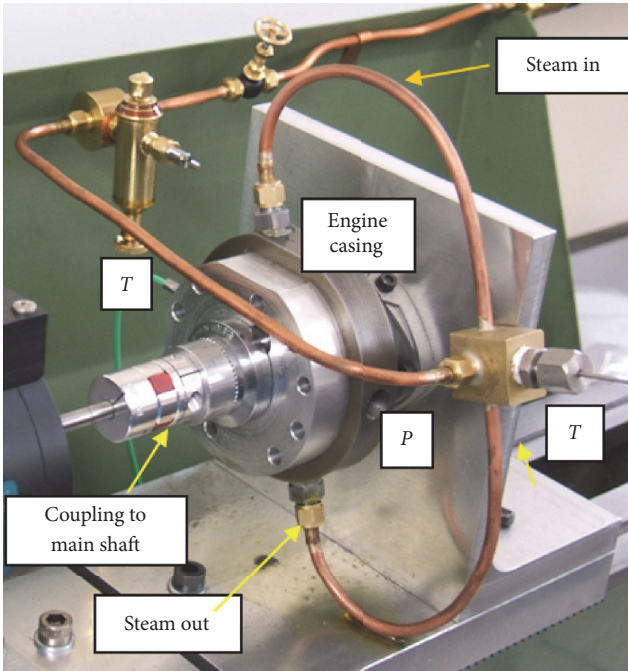


FIGURE 6: The Wankel engine; P = pressure sensor; T = thermocouple.

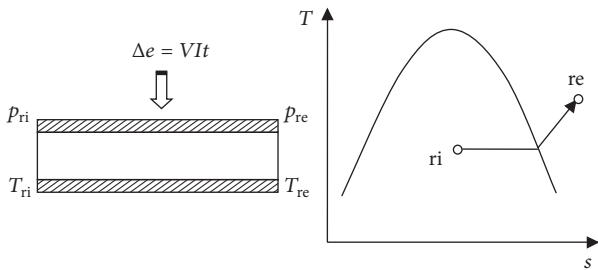


FIGURE 7: Steam quality analyzer (SQA).

the engine. These measurements can be used to determine the inlet and outlet conditions of the steam and hence to develop an energy balance.

2.3.6. *Engine Efficiency.* Efficiency of the engine can be calculated with the heat input values and the power developed by the engine.

3. Engine Test Results

Figures 10 and 13 show the power curves for different inlet pressures of the engine. The optimum supply pressure lies around 30 bars that has been confirmed by previous Prasad [7]. Pressures above this range will have a negative effect which is explained by a close analysis of the Molier diagram for water. Saturated steam at pressures above 30 bars stores less enthalpy than steam at 30 bars. Peak to peak measurements of pressures have been taken and the data are referred against supply pressure of zero. The readings are

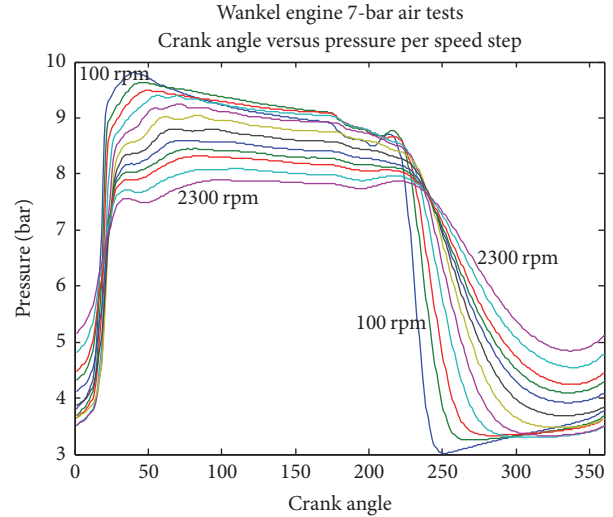


FIGURE 8: Wankel engine 7-bar air tests, crank angle versus pressure.

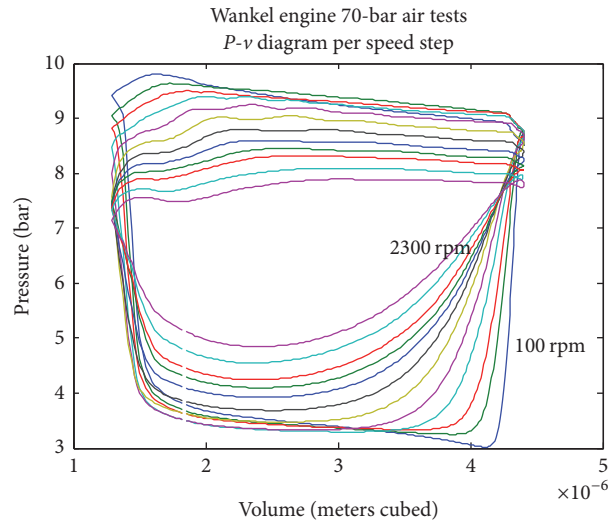


FIGURE 9: Wankel engine 7-bar air tests, p - V diagram.

plotted after taking the offset into account and reflect the absolute value.

3.1. *Air Tests on Wankel Engine.* Air test data was acquired for rpm values 100, 200, 300, 500, 700, 900, 1100, 1300, 1500, 1700, 2000, and 2300. The pressure volume diagram for air tests for the Wankel engine is given in Figure 9 for 7-bar air. The pressure-crank angle relationship is shown in Figure 8. When the supply pressure is low, substantial motoring takes place and is illustrated by the negative pressures in the P - v diagram.

Air test data was acquired for rpm values 200, 300, 500, 900, 1300, and 1700.

3.2. *Steam Tests on Wankel Engine.* Steam tests were done at 10-bar supply pressure and 15-bar supply pressure. 15-bar results are shown here as 15 bars was the highest pressure

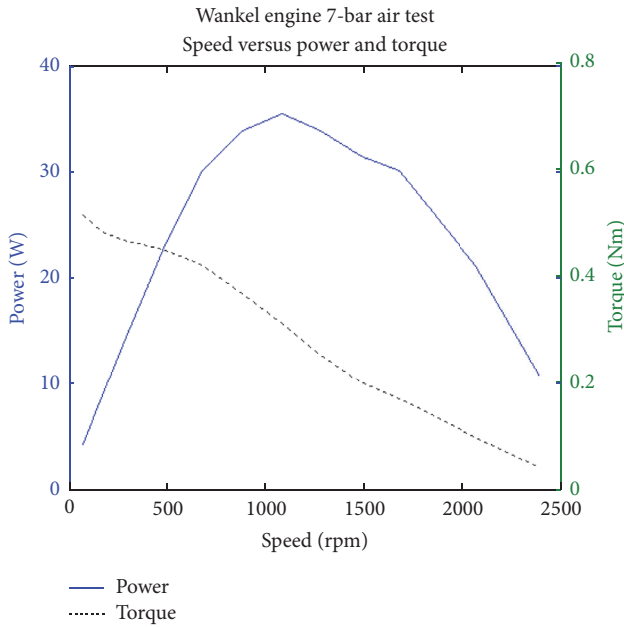


FIGURE 10: Wankel engine power and torque for 7-bar air.

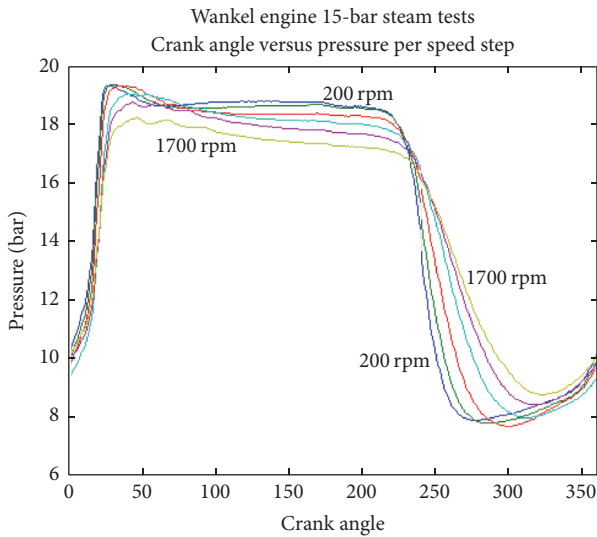


FIGURE 11: Wankel engine 15-bar steam tests, crank angle versus pressure.

at which data were logged as in Figures 11 and 12. Tests were done with a pressure regulated steam supply off an industrial boiler. The major observation expected of the pressure characteristics of the steam tests is the effect of expansion.

3.3. *Air and Steam Tests on Reciprocating Engine.* Measurements were taken on the expansion of steam at 10 bars in the reciprocating engine. Data was obtained only at 200 rpm to 800 rpm. This is deemed appropriate as the engine is expected to run at a lower speed than the IC engine. The shape of the $P-v$ diagram is significantly consistent with the theoretical

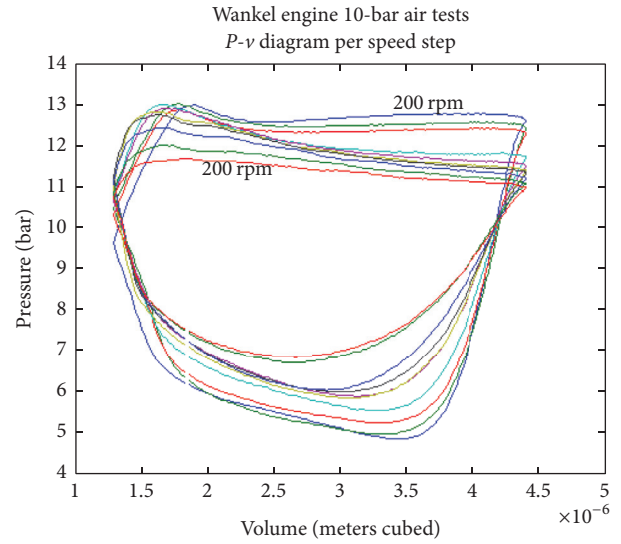


FIGURE 12: Wankel engine 15-bar steam tests, $p-V$ diagram.

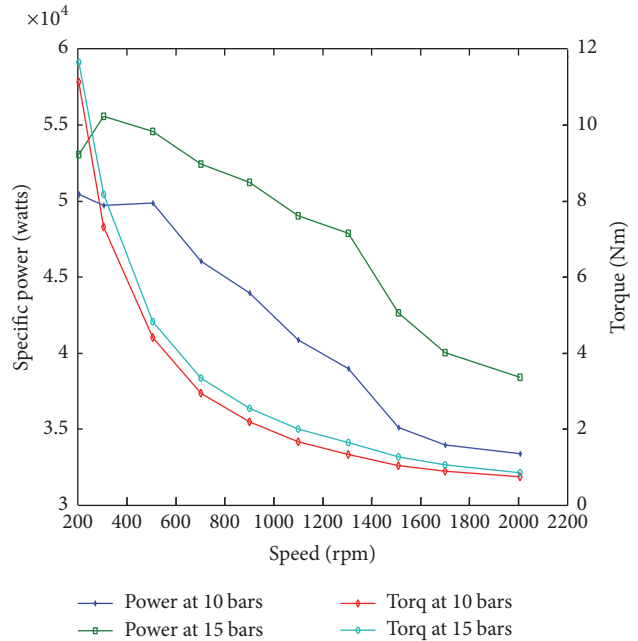


FIGURE 13: The Wankel engine power and torque for 10-bar and 15-bar steam.

diagram as shown in Figure 14. Specific power and torque characteristics are shown in Figure 15 at 10 bar.

The power torque diagram is also pretty impressive and is of expected shape except for the readings at 400 rpm. However, the general behavior is as expected.

Table 2 summarizes the results obtained for the air and steam tests. Air test diagrams are not shown in here as they were done only for validation purposes.

3.4. *Analysis of Results.* The $P-V$ diagrams for air and steam expansion in rotary and uniflow reciprocating engines are presented. The $p-V$ characteristics of the Wankel expander

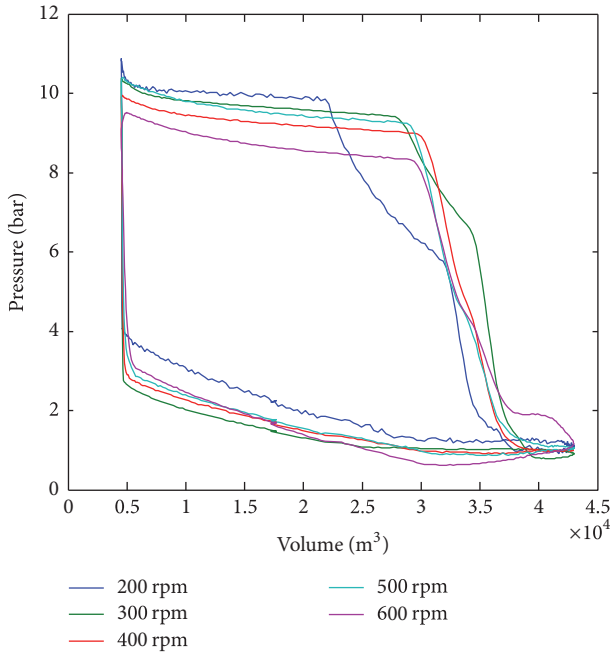


FIGURE 14: P - v diagram, reciprocating engine, 10-bar steam, with solenoid inlet valve.

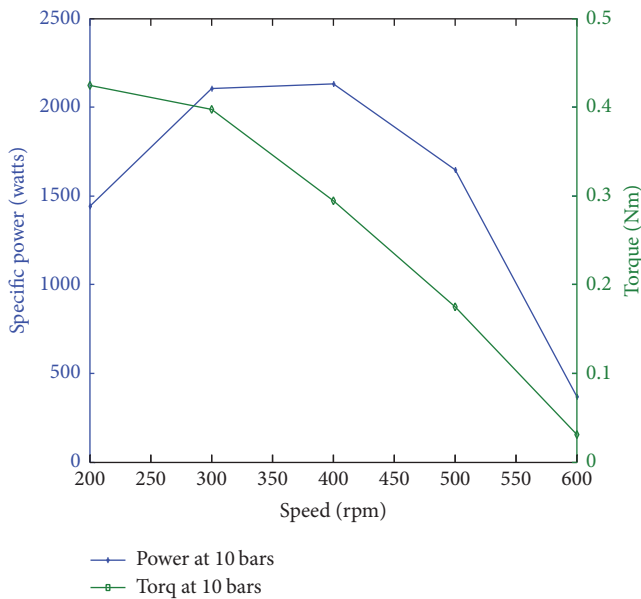


FIGURE 15: Specific power and torque, reciprocating engine, 10-bar steam.

are shown in Figures 9 and 12. The pressure against crank angle diagram for the Wankel engine shows a clear expansion of steam at low speeds. The expansion effect diminishes with higher speeds. This is better explained by the torque curve for the same. The torque developed is high at lower speeds. The clear reason for this behavior is the time taken by steam to expand [18]. The expansion of steam is much higher than that of air and the energy release is clearly visible. The maximum power curve for air gives a maximum at around 1000 rpm

TABLE 2: Performance comparison of the engines.

	Wankel engine	Reciprocating engine
Maximum power (air)	1400 W/kg	2800 W/kg
Maximum torque (air)	0.80 Nm	0.38 Nm
Maximum power (steam)	5550 W/kg	2600 W/kg
Maximum torque (steam)	11.65 Nm	0.45 Nm

whereas this for steam is at around 400 rpm. This shows the higher expansion rate of air. The steam coming out of the engines being wet means that there is a phase change in the expansion process. The phase change process is slower than the direct expansion of air. However, when these are used as bottoming cycles it is necessary to have a reduction ratio of around 10:1 to run parallel with an internal combustion engine. This is due to the fact that optimum operating rpm range of steam expanders lies within 100 to 250 whereas IC engines run optimum around 2000 rpm.

The slow operation of steam does not make it a less favored candidate as a bottoming cycle expansion medium. It allows the steam to build up and consumes at a slower rate as well. Once properly geared this should supply enough boost torque through the drive train.

In addition to the results obtained from testing, certain issues were highlighted during testing. The quality of the steam is critical to the prolonged operation of the engine [19]. A closed cycle system is hence preferred to an open cycle. The steam admission valve design is critical in the injection of steam into the cylinder. A mechanical device may be more robust, at least for the parts that are in contact with steam. The small engines may suffer from them being small, so that the endurance of the engines is low. It is anticipated to obtain better endurance from those engines.

Proper scaling can be done when all the simulation and test data are available for the engines.

4. Conclusion and Future Work

Performance measurements have been carried out to predict the suitability of small engines as steam expanders. The engines have been modified to suit steam expansion. The operating speed range of steam is much lower than that of internal combustion engine. This prevents us making direct comparisons. The air tests provide a much comparable set of data for the expanders. Comparing the maximum power and torque data of the two engines it is evident that the Wankel engine provides a much better device as an expander.

The major aim of this work is to measure the suitability of Rankine steam cycle as a heat recovery bottoming cycle and compare the performance of two engine types, the reciprocating engine and the Wankel engine. The power and torque characteristics shown for small engines make them very suitable for the purpose. The work involves the development of complete Rankine bottoming cycle including controls. This includes the heat recovery system and thermal control of the IC engine and the steam cycle. Endurance tests need to be done to steam engines developed to check the

longevity [3, 20]. Separate work is being done to develop the control strategies and techniques.

The scaled down dynamometer developed to measure the performance of the engine provides a very useful tool for scaled model testing. The torque and power curves obtained could be scaled up for a full size engine.

The valve timing for the two-stroke engine is a sensitive factor in the engine performance. Small engines do not allow a great deal of flexibility for us to change this. Only the timing can be changed with electronic triggering. In a full scale engine, much larger valves can be employed and there will be room for finer adjustment.

The tests revealed a number of areas for improvement. The reliability of the engines could be a major issue. Use of steam oil that improves reliability is possible with a closed cycle. In an open cycle this becomes an emission issue as it will be released to the atmosphere.

Using small engines to determine engine characteristics supplies a basis for designing medium scale steam engines. The finding can be backed up by simulations once a complete set of data are available. The authors intend to do further testing on a larger engine with a heat recovery system attached to an internal combustion engine.

4.1. Engine Simulations. The results can be compared with results obtained from 1D engine simulation results. Values can be obtained for air expansion and an optimum operating point can be obtained. No simulation results are presented at this moment. Initial comparisons which are not presented here, however, suggest that the measurements can be backed by simulations. These results show that steam expanders, even at small scale, are suitable devices for heat recovery bottoming cycles. A full set of simulations as described above can be used for scaling up of the findings for commercial engine applications. The motoring effect and friction are expectedly high in small engines as a percentage. However, they provide concept proving valid statistics.

Conflicts of Interest

The authors declare that there are no conflicts of interest regarding the publication of this paper.

Acknowledgments

The authors would like to extend their gratitude to the EPSRC for funding the work [Grant no. GR/T19810/01], Professor R. K. Stobart, the principal investigator, Ian Wallis and Barry Jackson of University of Sussex for their support in conducting the research, and Spirax Sarco Ltd., UK, for providing steam facility and support.

References

- [1] P. W. B. Semmens and A. J. Goldfinch, *How Steam Locomotives Really Work*, Oxford University Press, 2000.
- [2] G. Ferrara, G. Manfrida, and A. Pescioni, "Model of a small steam engine for renewable domestic CHP (combined heat and power) system," *Energy*, vol. 58, pp. 78–85, 2013.
- [3] S. Jakuba and J. A. McGeehan, "Component development of automotive reciprocating steam expanders," SAE Prepr, SAE Technical Paper, 1975.
- [4] S. Zhu, K. Deng, and S. Qu, "Energy and exergy analyses of a bottoming rankine cycle for engine exhaust heat recovery," *Energy*, vol. 58, pp. 448–457, 2013.
- [5] M. Badami and M. Mura, "Preliminary design and controlling strategies of a small-scale wood waste Rankine Cycle (RC) with a reciprocating steam engine (SE)," *Energy*, vol. 34, no. 9, pp. 1315–1324, 2009.
- [6] G. Bidini, A. Manuali, and S. Saetta, "Reciprocating steam engine power plants fed by woodwaste," *International Journal of Energy Research*, vol. 22, no. 3, pp. 237–248, 1998.
- [7] S. B. Prasad, "Steam engine characteristics and theoretical performance," *Energy Conversion and Management*, vol. 34, no. 12, pp. 1323–1333, 1993.
- [8] G. A. Brown and D. A. Bowlus, "Rotary piston expander engine," in *Proceedings of the 11th ICECEC*, pp. 1187–1191, 1976.
- [9] O. Badr, S. Naik, P. W. O'Callaghan, and S. D. Probert, "Expansion machine for a low power-output steam Rankine-cycle engine," *Applied Energy*, vol. 39, no. 2, pp. 93–116, 1991.
- [10] J. D. Wade, R. M. Tompkins, G. A. Brown, and G. J. Silvestri, "Rotary expander engine testing and analysis," in *Proceeding of 18th IECEC*, pp. 636–641, 1983.
- [11] C. H. Lee, K. C. Jiang, P. Jin, and P. D. Prewett, "Design and fabrication of a micro Wankel engine using MEMS technology," *Microelectronic Engineering*, vol. 73–74, pp. 529–534, 2004.
- [12] L. Tartakovskiy, V. Baibikov, M. Gutman, M. Veinblat, and J. Reif, "Simulation of Wankel engine performance using commercial software for piston engines," *SAE Technical Papers*, vol. 4, 2012.
- [13] B. Fu, Y. Lee, and J. Hsieh, "Experimental investigation of a 250-kW turbine organic rankine cycle system for low-grade waste heat recovery," *International Journal of Green Energy*, vol. 13, no. 14, pp. 1442–1450, 2016.
- [14] R. Stobart and R. Weerasinghe, "Heat recovery and bottoming cycles for SI and CI engines—A perspective," *SAE Technical Papers*, no. 0662, 2006.
- [15] G. Qiu, H. Liu, and S. Riffat, "Expanders for micro-CHP systems with organic Rankine cycle," *Applied Thermal Engineering*, vol. 31, no. 16, pp. 3301–3307, 2011.
- [16] F. J. Bayley, "The saturated liquid reservoir for energy storage in hybrid vehicles," in *Proceedings of the IMechE Automobile Division SoUthern Centre Conference on Total Vehicle Technology Challenging Current Thinking*, September 2001.
- [17] R. Stobart, S. Hounsham, and R. Weerasinghe, "Controllability of vapour based thermal recovery systems in vehicles," *SAE International, World Congress*, no. 0270, 2007.
- [18] W. M. S. R. Weerasinghe, R. K. Stobart, and S. M. Hounsham, "Thermal efficiency improvement in high output diesel engines a comparison of a Rankine cycle with turbo-compounding," *Applied Thermal Engineering*, vol. 30, no. 14–15, pp. 2253–2256, 2010.
- [19] V. Dolz, R. Novella, A. García, and J. Sánchez, "HD Diesel engine equipped with a bottoming Rankine cycle as a waste heat recovery system. Part 1: study and analysis of the waste heat energy," *Applied Thermal Engineering*, vol. 36, no. 1, pp. 269–278, 2012.
- [20] A. Nuvolari, B. Verspagen, and N. von Tunzelmann, "The early diffusion of the steam engine in Britain, 1700–1800: a reappraisal," *Cliometrica*, vol. 5, no. 3, pp. 291–321, 2011.

Research Article

Parametric Study to Improve Subpixel Accuracy of Nitric Oxide Tagging Velocimetry with Image Preprocessing

Ravi Teja Vedula,¹ Mayank Mittal,² and Harold Schock¹

¹Department of Mechanical Engineering, Michigan State University, East Lansing, MI 48824, USA

²Department of Mechanical Engineering, Indian Institute of Technology Madras, Chennai 600036, India

Correspondence should be addressed to Ravi Teja Vedula; vedulara@egr.msu.edu

Received 30 September 2016; Accepted 20 November 2016; Published 20 February 2017

Academic Editor: Guohong Tian

Copyright © 2017 Ravi Teja Vedula et al. This is an open access article distributed under the Creative Commons Attribution License, which permits unrestricted use, distribution, and reproduction in any medium, provided the original work is properly cited.

Biacetyl phosphorescence has been the commonly used molecular tagging velocimetry (MTV) technique to investigate in-cylinder flow evolution and cycle-to-cycle variations in an optical engine. As the phosphorescence of biacetyl tracer deteriorates in the presence of oxygen, nitrogen was adopted as the working medium in the past. Recently, nitrous oxide MTV technique was employed to measure the velocity profile of an air jet. The authors here plan to investigate the potential application of this technique for engine flow studies. A possible experimental setup for this task indicated different permutations of image signal-to-noise ratio (SNR) and laser line width. In the current work, a numerical analysis is performed to study the effect of these two factors on displacement error in MTV image processing. Also, several image filtering techniques were evaluated and the performance of selected filters was analyzed in terms of enhancing the image quality and minimizing displacement errors. The flow displacement error without image preprocessing was observed to be inversely proportional to SNR and directly proportional to laser line width. The mean filter resulted in the smallest errors for line widths smaller than 9 pixels. The effect of filter size on subpixel accuracy showed that error levels increased as the filter size increased.

1. Introduction

Flow field inside the engine cylinder is one of the most important factors controlling the fuel combustion process and hence engine performance [1, 2]. This realization arises in the automotive engine community after attaining relatively significant knowledge on in-cylinder flows and their cycle-to-cycle variations in the past few decades, while noticing the occasional dominance of the high-speed fuel spray in preparation of combustible air-fuel mixture [3–5]. Flow measurement techniques such as laser Doppler velocimetry (LDV [6–9]), particle image velocimetry (PIV [10–15]), and molecular tagging velocity (MTV [16]) continue to play a crucial role in understanding in-cylinder flows of an automotive engine. Effective quantitative details such as in-cylinder flow velocity, velocity root-mean-square (rms), circulation, and turbulent length and time scales are being made possible from such advanced measurement techniques. Magnetic

resonance imaging is yet another technique, majorly used in medical field, which has been recently employed for engine flow studies in the form of magnetic resonance velocimetry (MRV) [17–19]. A major advantage of MRV is that optical access is not needed for data acquisition, allowing it to be used for flow imaging in highly complex geometries. Molecular tagging velocimetry offers multipoint, planar measurements demanded for engine flow studies, overcoming the single-point measurement issues of LDV and hot-wire anemometry. The number of particle images per interrogation region or the particle image density is an important parameter that affects the PIV measurement uncertainty [20, 21]. Particle image density sometimes increases as the chamber volume decreases during piston compression. This would heighten the probabilities of increase in particle size and correlation peak uncertainty; the particle size increases due to agglomeration and/or thermal expansion due to higher temperatures [12]. Having mentioned these uncertainties, there are several

PIV-based works that captured the velocity field throughout the engine cycle [22, 23]. Nevertheless, MTV is relaxed from maintaining such desired levels of particle image density as seen for PIV within the temporally varying cylinder volume due to piston motion. Another point to note is occasionally in PIV; the particles cannot follow the flow when the flow motion undergoes high spatial and temporal acceleration [24]. Fulfilling the Stokes number condition $S_k < 0.1$ [16] could be an option for verifying the flow-following capability. However, a study showed that the particles tracked the flow properly even when the S_k value was greater than 0.1 and only failed to follow for measurements in the Taylor length scale [25]. A brief overview with several applications of MTV for engine flow studies is given in [26]. MTV is a flow measurement technique that is based on one of the two luminescence principles: phosphorescence and fluorescence. In the phosphorescence technique, a pulsed laser marks a pattern on excitation of the phosphorescent molecules (premixed or inherent) in the flow. The long-lived phosphorescence of these tracers is captured at two instants of time (undelayed, time zero; delayed, time Δt). In the fluorescence technique, a “write” laser photodissociates the seeded or inherent molecule in the flowing medium. The new photoproduct is excited with another “read” laser and the corresponding fluorescence is captured at two instants of time (undelayed and delayed). The Lagrangian displacement vector evaluated within a known time span provides the flow velocity. By using a collection of tagged lines instead of a laser sheet, spatial resolution of MTV could be controlled to some extent with the MTV grid spacing while taking into account other factors such as the laser line width and optics arrangement. Also, using laser lines reduces the amount of wall reflections due to reduced number of photons per unit area, impinged on the optical window or the liner.

Biacetyl has been demonstrated to be an elegant molecular tracer for flow measurements mainly due to its longer phosphorescence lifetime which allows measuring both high and low speed flows. Epstein developed a new quantitative flow visualization technique using biacetyl as the seeder to measure the time resolved, three-dimensional flow in a transonic compressor rotor [27]. Hiller et al. [28] demonstrated the applicability of biacetyl as a molecular tracer for laser-marking method for velocity measurements in gas flows. Biacetyl phosphorescence MTV was used for several in-cylinder swirl and tumble flow studies in an optical engine. Phosphorescence MTV with biacetyl tracer suffers from quenching due to O_2 . Hence the engine flow studies using biacetyl phosphorescence adopted N_2 as the working medium, assuming that it represents the air motion. Such an assumption is worthwhile, and this technique offered planar and three-dimensional whole field detection of in-cylinder flows and their cycle-to-cycle variations using molecule as the seed [29–31]. Nevertheless, an analysis of in-cylinder flows using air as the working fluid would be more convenient than using nitrogen based system, especially at low manifold pressures. Nitric oxide (NO) tagging velocimetry has been in use for measuring high-speed air flows without exhibiting any major quenching effects [32, 33]. This MTV technique is a fluorescence-based type wherein a seed molecule is

photodissociated to create NO line(s). On identifying the usage of toxic gases as the conventional seed molecules for NO MTV, Elbaz and Pitz [34] employed nitrous oxide (N_2O) as the seed to create N_2O -to-NO tag lines. Nitrous oxide, also called “laughing gas,” is nontoxic and sometimes used as an aerosol agent in foods. Based on the photodissociation chemistry of N_2O , both the initial amount of N_2O seeded and the fraction which is dissociated to NO would determine the signal-to-noise ratios (SNRs) of the resulting grid images. The laser energy density (J/cm^2) as required to achieve desired levels of N_2O dissociation demands maximum energy utilization, starting from the laser output. Furthermore, maintaining a uniform energy density for multiple beams to construct a sufficiently dense MTV grid would determine the thickness of the laser lines. For instance, an excitation beam of 5 mJ and 0.47 mm nominal diameter was used to obtain 25% dissociation of N_2O in 4% N_2O -air mixture [34]. The same energy density ($\sim 3 J/cm^2$) could be achieved with a beam of 2.3 mJ and 1 mm nominal diameter assuming all the other parameters to be constant.

Spatial correlation technique [35] has been the standard method employed to correlate undelayed and delayed MTV images of in-cylinder flows and thereby determine the corresponding Lagrangian displacement vector. Instead of a direct cross correlation coefficient $\overline{I_1 \cdot I_2}$ as used for PIV image processing [36], a normalized direct cross correlation or the spatial correlation coefficient is used for MTV images and is written as

$$R = \frac{\overline{I_1 \cdot I_2} - \overline{I_1} \cdot \overline{I_2}}{\sigma_{I_1} \sigma_{I_2}}, \quad (1)$$

where the overbar is for expected value, I is the intensity field, and σ is the standard deviation. Subscripts 1 and 2 represent source window (on undelayed image) and roam window (on delayed image) for MTV and interrogation spots at two recording times for PIV.

An illustration of this data processing method is included later in this work. The spatial correlation function is discrete and the flow displacement is computed with single pixel resolution. Hence, a fitting polynomial is used for correlation values in the vicinity of its peak to attain subpixel accurate displacements. Accuracy of MTV measurements for engine flow studies was previously reported to be within 0.1 pixels, (i) using spatial correlation technique in a steady flow rig model [37] and (ii) using spatial correlation in combination with a decoupled technique [38] for in-plane velocity component of stereoscopic measurements [31].

Having realized the potential application of N_2O MTV for in-cylinder air flow studies, the authors here investigated the effect of image SNR and laser line width (LW) on the subpixel accuracy of flow displacements. Several image filtering techniques are evaluated, and the performance of selected filters is analyzed in terms of error reduction. The current study builds on the work of [35, 39]. Effect of factors such as image SNR, contrast enhancement, laser line width, and source window size (related to MTV’s spatial correlation technique) on subpixel accuracy was studied in [35]. Effect of image preprocessing on displacement error reduction was

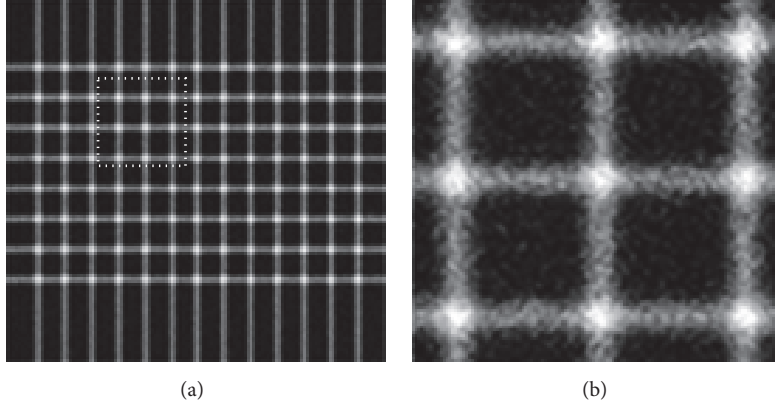


FIGURE 1: (a) Simulated undelayed image having an 8×13 MTV grid and (b) zoomed-in view of the highlighted region in (a).

analyzed using image filters in [39]. Caso and Bohl [39] utilized multiple filter techniques for image preprocessing; however, the results of only mean and sigma (modified mean) filters were presented. The current work reproduces some of the results obtained in the above two works while discussing in more detail the performance of various image filters in enhancing the image quality and MTV error reduction. These discussions will be corroborated with visual demonstrations and graphical results. Although the prime motive is to assess the requirements to develop an N_2O MTV measurement system for engine flow studies, this analysis work is applicable to any 2D-MTV (grid pattern) technique in general. Synthetic images were generated to perform these studies, and the details of the generation process are discussed in the next section.

2. Methods: Synthetic Image Generation and Image Filtering Techniques

MTV technique requires that a pair of images (undelayed image at the initial time, $t_1 = t$, and delayed image at the later time, $t_2 = t + \Delta t$) be acquired during the luminescence lifetime of the molecular tracer. The first (or undelayed) image, representing a region of tagged flow, was simulated by laying down an 8×13 grid of Gaussian profile “laser lines” as shown in Figure 1. It should be noted that the excimer laser outputs a rectangular beam having a top-hat intensity profile along one axis and a Gaussian profile along the other. Depending on the axis chosen for reducing the beam into a sheet, the laser lines can be considered to be of Gaussian profile. In addition, it was observed previously that the error magnitude was higher for Gaussian profile than for non-Gaussian profile [35]. Hence, Gaussian profile laser lines are implemented for the current study to investigate the performance of image filters under limited experimental optimizations. These lines were characterized by w (note that, in the present work, line width corresponds to $2w + 1$ pixels) their peak intensity, I_{\max} , and the location of the line center, d , via

$$I = I_{\max} \exp^{-d^2/w^2}. \quad (2)$$

In the present work, I_{\max} was fixed at 80 counts and a uniform background intensity of 30 counts was added to the image to simulate nonzero black levels typically seen in intensified CCD cameras. This led to a maximum intensity of 190 counts where the lines intersected. The second (or delayed image), representing the tagged region at the later time, was generated by displacing the laser lines of the original image by a known displacement vector. This simulation strategy was used in prior studies; see, for example, [35, 39]. In this work, Gaussian white noise was added to both undelayed and delayed simulated images, and then the pixel intensities were scaled to achieve the desired contrast. Caso and Bohl [39] also added the same level of noise to both undelayed and delayed simulated images for a more accurate reflection of real-world conditions. As demonstrated using Figures 1(a) and 1(b), the magnified view of a chosen section of the whole image showed more clearly the details of signal and noise distributions. Hence, hereafter this magnified region of the original images is considered in discussion.

Signal-to-noise ratio is one of the crucial image features that determine the accuracy of flow parameters in techniques such as particle image velocimetry and molecular tagging velocimetry. As the name indicates, optical SNR can be described as the ratio of photon signal to the noise present around this signal. One of the ways to determine the image SNR is by using a reference image [40]. In the absence of a reference image, determining SNR becomes more challenging and uncertain due to unavailability of a source for comparison. This situation is more applicable in MTV or any other experimental techniques. In such cases, considering a local neighborhood of a pixel would be the preferred way of detecting probable presence of noise and thereby evaluating SNR value. The neighborhood of a pixel can be sampled in several ways, among which the 4-connected and 8-connected neighborhood are most commonly used [41]. In the 4-connected neighborhood, the signal and noise are considered at 4 pixels that are adjacent to the edges of a central pixel (Figure 2(a)). Additionally, diagonal pixels are included in the 8-connected neighborhood (Figure 2(b)).

The pixel-wise SNR values were determined at the central pixels of the 8-connected neighborhood window and in the

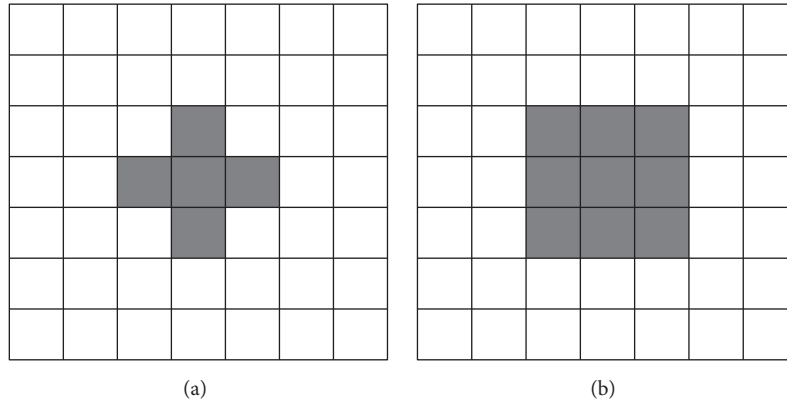


FIGURE 2: Pixels highlighted in (a) 4-connected neighborhood and (b) 8-connected neighborhood around a chosen central pixel.

end were averaged to obtain the pixel-mean SNR of the whole image. The default definition used here for SNR was

$$\text{SNR} = \frac{\text{mean} [A_{P \times Q}]}{\text{standard deviation} [A_{P \times Q}]}, \quad (3)$$

where $A_{P \times Q}$ is the pixel intensity matrix of size $P \times Q$.

The SNR of an image in general can be enhanced using different image filtering techniques. These techniques make use of either spatial filters, for example, mean, median, sigma, and Wiener filters, or frequency filters, for example, ideal pass, Gaussian, and Butterworth filters [42, 43]. Selected filters were applied to the simulated images and their effectiveness in enhancing the image SNR was evaluated.

2.1. Spatial Filters. A spatial filter replaces the value at a given pixel with an operand value (mean, median, threshold-based sigma, etc.) of all pixels within a selected neighborhood. Several types of mean filters such as arithmetic mean, contraharmonic mean, and alpha-trimmed mean filters were tested on the simulated images (not shown here). It was observed that the arithmetic mean filter was more effective in noise removal in the current images compared to the other two. Hence, the arithmetic mean was chosen to analyze the performance of the mean filter. Figures 3(a)–3(d) show the original image and the preprocessed images obtained by applying various spatial filters. The corresponding SNR values evaluated from (3) were noted above these images. As seen in the mean-filtered image (Figure 3(b)), a significant amount of noise was removed from the highly noisy image (Figure 3(a)). However, the averaging of signal intensities resulted in a relatively darker or low intensity grid; grid nodes in the mean-filtered image are notably dimmer than in the original image. The filtered image SNR value increased which could suggest that the mean filter was effective in noise removal.

In general, median filters are known for removing the impulse noise or “salt-and-pepper” noise. This is apparent when Figure 3(c) is compared with Figures 3(a) and 3(b). The median filter remarkably removed the noise present in the line-to-line gap (or void region), black/clean regions compared to spotted regions in Figure 3(a) and shaded

regions in Figure 3(b). Another advantage of median filter over mean filter is that the former prevents or minimizes significantly the smoothening of the actual signal intensities especially as apparent here at the grid nodes. However, the laser lines in the median-filtered image were nonuniform, with additional intensities randomly appended. This latter feature of random intensity addition can be attributed to the original noise and might have been detected by the MATLAB code as signal intensity, thereby resulting in a higher SNR value. Similar to the median filter, the Wiener filter could remove noise in the void regions (in Figure 3(d)). However, the noise overlaid on the actual lines was not removed completely and is visually apparent; see Figure 3(d). The higher SNR of the Wiener-filtered image might be again due to the falsification of noise as signal intensity. These visual observations will be revisited in Section 4.2 to assess quantitatively the performance of these filters in reducing the measured displacement errors.

2.2. Frequency Filters. While spatial filtering techniques are applied in the spatial domain, frequency filtering techniques are applied to the image of interest in the frequency domain. The idea here is to process the raw images by analyzing the gradient of intensities, that is, the rate of change of a chosen intensity level in the frequency domain. This is attained using the convolution theorem, which states that the Fourier transform of the product of two functions in the spatial domain is the convolution of the transforms of the two functions in the frequency domain. In general, noise signals have peak frequency values due to sharp intensity transitions and hence a low-pass filter is preferred for noise removal [42]. Commonly used low-pass frequency filters are the ideal pass filter, Gaussian filter, and Butterworth filter. For the current study, the Gaussian filter was considered due to the well-known “ringing” effect of ideal pass filter and itself acting as a special case of Butterworth filter. Given that the simulated images were generated by adding a Gaussian white noise, the performance of the Gaussian filter in error reduction could be considered as a reference to assess the performance of other filters. Figure 4 shows the performance of the Gaussian filter with a cut-off frequency of 50 Hz on the highly noisy

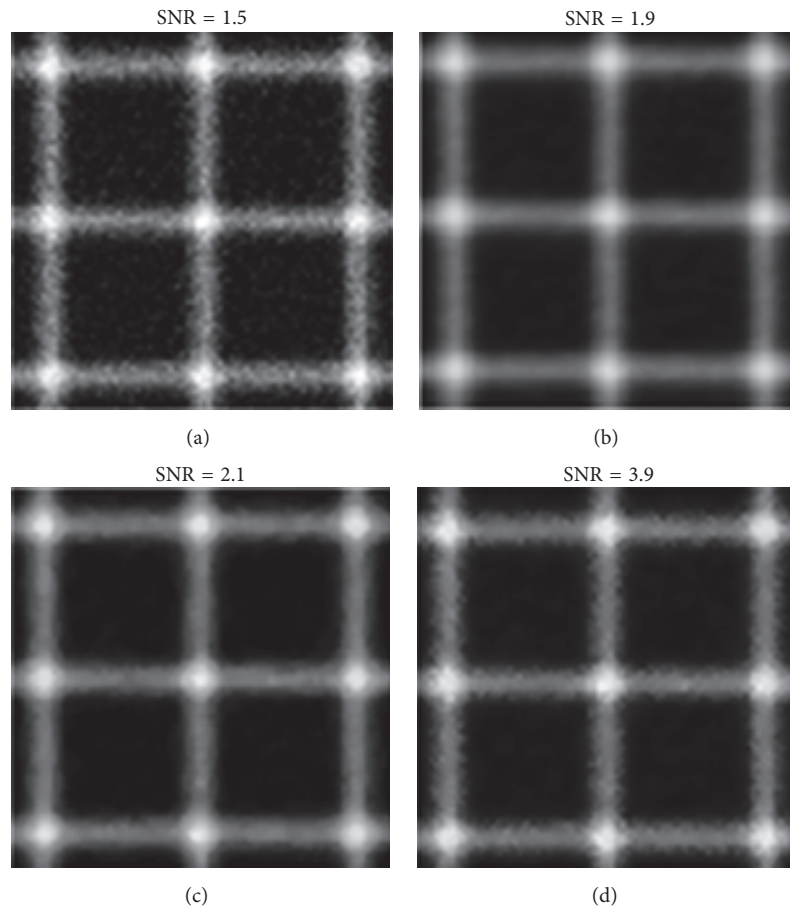


FIGURE 3: (a) Original, (b) mean-filtered, (c) median-filtered, and (d) Wiener-filtered image. Here $LW = 9$ pixels.

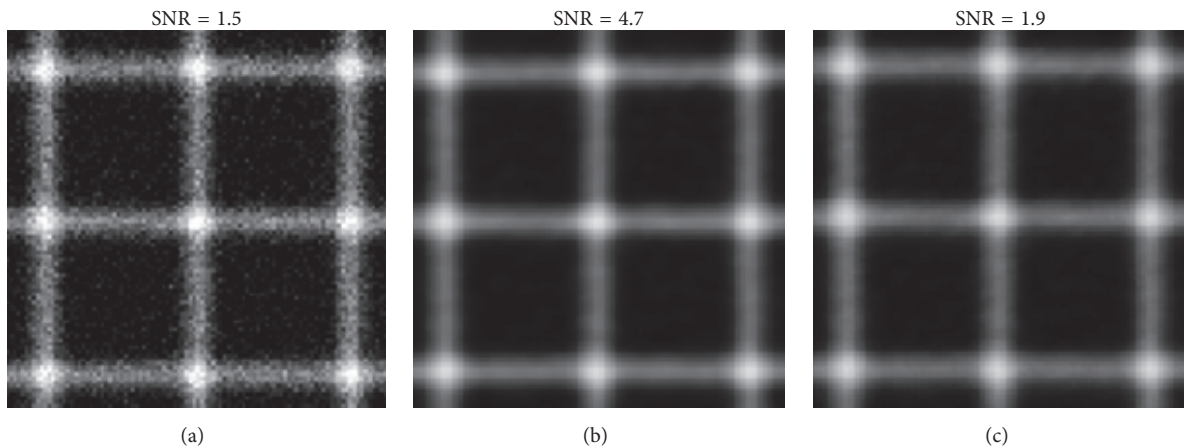


FIGURE 4: (a) Original image, (b) filtered image after applying the Gaussian filter, and (c) mean-filtered image. Here $LW = 9$ pixels.

image. As expected, the filtered image (Figure 4(b)) contained minimal noise levels both at the void regions and along the MTV lines. Also, the intensities at the grid nodes and along the lines are brighter with the Gaussian filter when compared to those in the mean-filtered image (included in Figure 4(c) for ease in comparison). With the Gaussian Fourier transform, a threefold increase in image SNR value was noted compared to the original image.

3. MTV Data Processing

As discussed earlier, analyzing the effect of image SNR and laser line width on MTV subpixel accuracy is crucial when employing N_2O MTV for in-cylinder flow studies. The MTV grid displacements have been attained at subpixel accuracy level using a combination of spatial correlation techniques and polynomial fitting [38]. As seen in Figure 5, there is

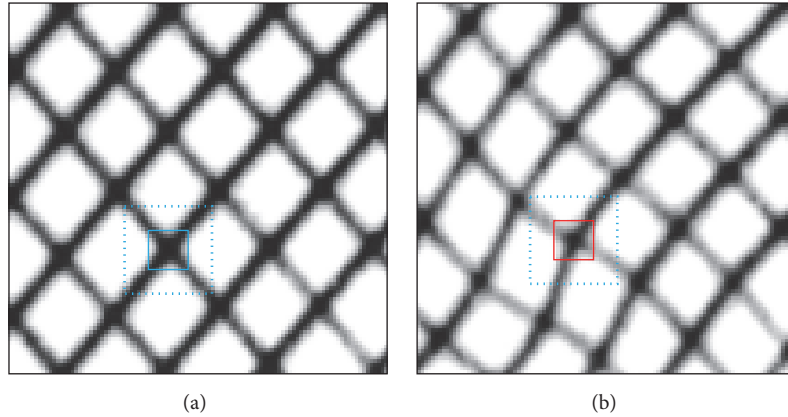


FIGURE 5: (a) and (b): undelayed and delayed MTV images, showing source (solid squares) and room (dashed square) windows. Adapted from [35].

		Undelayed image																	Delayed image														
		C1	C2	C3	C4	C5	C6	C7	C8	C9	C10	C11	C12	C13	C14	C15			C1	C2	C3	C4	C5	C6	C7	C8	C9	C10	C11	C12	C13	C14	C15
R1	37	46	62	86	108	122	140	146	139	128	108	85	72	45	32	R1	9	16	26	36	51	77	96	107	127	130	124	115	94	69	57		
R2	49	59	77	100	115	140	149	158	155	136	123	94	75	58	49	R2	16	22	33	43	54	77	97	119	133	138	134	121	101	76	56		
R3	61	77	92	114	133	155	168	180	168	157	137	113	92	74	67	R3	21	27	38	47	64	89	107	126	137	149	143	127	106	85	63		
R4	86	98	119	138	156	177	190	195	193	175	152	131	110	95	86	R4	37	36	48	62	76	98	121	137	153	156	150	136	118	96	79		
R5	106	118	133	154	179	195	214	218	213	198	181	152	134	113	109	R5	54	63	63	75	95	114	137	155	170	177	170	156	135	114	96		
R6	124	146	155	179	196	218	234	241	228	223	205	173	154	140	126	R6	72	72	90	93	115	135	153	177	186	199	187	175	160	136	116		
R7	138	152	169	188	212	227	244	250	241	231	206	190	170	152	143	R7	95	103	111	122	139	155	183	194	213	215	211	199	175	155	134		
R8	150	158	175	188	215	237	249	255	250	235	217	195	175	155	141	R8	111	114	126	139	155	175	199	215	235	238	231	218	195	175	155		
R9	140	151	176	189	211	230	245	244	247	228	208	186	177	151	141	R9	129	135	138	155	169	192	208	233	243	251	247	230	213	190	167		
R10	126	135	158	179	197	215	230	240	237	216	197	176	155	140	125	R10	132	137	144	161	174	191	216	238	249	250	248	236	213	194	172		
R11	107	125	137	155	177	196	207	220	213	201	177	157	135	119	109	R11	132	129	142	152	168	192	209	233	248	251	240	229	211	187	170		
R12	87	100	117	134	158	176	190	195	193	177	153	133	114	94	85	R12	116	119	126	133	156	178	195	219	230	235	233	220	203	178	158		
R13	68	76	91	116	136	156	171	171	167	149	131	114	91	81	65	R13	91	95	109	117	140	155	179	198	207	218	209	194	179	156	135		
R14	49	64	80	96	120	135	153	161	153	136	118	100	76	58	44	R14	74	76	88	100	115	133	158	178	186	194	186	176	156	135	117		
R15	38	47	65	88	106	124	141	145	143	126	103	85	68	50	38	R15	52	60	64	77	92	113	132	153	168	176	170	157	136	112	90		

FIGURE 6: Illustration of spatial correlation technique: (a) a 7×7 source window with center at (R8, C8) on the undelayed image and (b) highlighted window on the delayed image whose intensities correlate best with those of source window. Thus the tagged region is displaced two pixels in X and Y direction with the center at (R10, C10); correlation coefficient peak $R_{\max} = 0.9984$.

an undelayed image (a) taken immediately ($O \sim ns$) after the photon impingement by laser and the delayed image (b) taken after allowing the flow to move ($O \sim \mu s$). The small solid square is the source window, covering only one grid node in the undelayed image. The principle is to obtain the displacement at each grid node, thereby resulting in a global Lagrangian displacement vector. As seen clearly from this figure, the grid node covered by the source window on the undelayed image is displaced, due to flow motion, to a new location (see smaller solid square on the delayed image on the right). Also, there is a larger dashed square, called roam window, marked surrounding the solid square on the delayed image. This roam window is concentric to the source window's center located on the undelayed image. To show such concentricity, a dotted square is introduced in Figure 5(a); in actual processing, there is no dotted square window applied on the undelayed image.

A spatial correlation coefficient, $R(r, s)$, is determined between the intensity field I_1 of the source window and I_2 of the roam window as a function of pixel displacement (r, s) between them. From the obtained array of $R(r, s)$, the maximum value represents the location of the displaced

source window and, hence, the grid node. Figures 6(a) and 6(b) show sample pixel intensities of a section of undelayed and delayed MTV images. A 7×7 source window, as highlighted in Figure 6(a), has its center at row R8 and column C8 with pixel intensity of 255 (grayscale maximum value). This pixel represents the intersection of two laser lines or in other words the central pixel of an MTV grid node. On correlating the intensity field of source window and a roam window (size of 15×15 in this case) on the delayed image, the window highlighted in Figure 6(b) is determined to correlate well ($R_{\max} = 0.9984$). Hence for this example, the tagged flow moved two pixels in both X and Y directions as indicated by the new window centered at (R10, C10).

From the illustration above, it is expected that the source window should contain sufficient intensity gradients in order to attain more accurate correlations. Such a displacement obtained is of pixel accuracy. In order to obtain the desired subpixel accuracy, the spatial correlation technique includes a higher-order polynomial fitting about the correlation peak of the R matrix. For each simulated case in the present work, one undelayed image (total 104 grid nodes formed by 8 horizontal

and 13 vertical laser lines) and five delayed images were considered. This provided in total 1040 grid displacements in the X and Y directions for each case. A source window of 27×27 was chosen for evaluating the synthetic image displacements. The rms error of displacement was defined as follows:

$$\text{rms error} = \frac{[\text{stdev}(\text{Disp}_X) + \text{stdev}(\text{Disp}_Y)]}{2}, \quad (4)$$

where Disp_X and Disp_Y are the MTV grid node displacements in the X and Y directions obtained from the correlation technique and stdev is the standard deviation. In addition, the statistical error quoted as the 95% error level or confidence level of displacement [39],

$$\begin{aligned} & \text{95\% Error level} \\ & = \sqrt{(\text{Disp}_{X_{\text{meas}}} - \text{Disp}_{X_{\text{actual}}})^2 + (\text{Disp}_{Y_{\text{meas}}} - \text{Disp}_{Y_{\text{actual}}})^2}, \quad (5) \end{aligned}$$

was used for the current analysis. Here subscripts “meas” and “actual” represent the values obtained from spatial correlations and the original values used to create the synthetic images.

4. Results and Discussion

4.1. Effects of SNR and Line Width on Subpixel Accuracy without Filtering. Figure 7 shows the sample of original undelayed images (partial grid taken from the whole 8×13 grid) for various SNR values with a laser line width of 11 pixels. Image SNRs showed values from 2.5 to 1.2 for a to i without filtering. As will be discussed later, the SNR values changed when the images were preprocessed using various filters. Hence, for suitable comparisons and a consistency in the discussion, the SNR values are designated alphabetically while the numerical values are mentioned wherever appropriate. The SNR values for biacetyl MTV images captured in previous engine flow studies usually ranged from 7 to 15 (values based on (3)), with a laser line width of about 11 pixels. Simulating the image noise is complex due to various sources of noise seen in the actual experimental images such as shot, dark current, hot pixel, and readout noises [44]. Also, the fluorescence yield of the nitric oxide molecules as seen in N_2O MTV depends on several factors. Some of these factors are the read laser energy, in-cylinder air pressure and temperature, and the NO number density. Considering all the aforementioned signal and noise uncertainties possible with N_2O MTV, the current work investigates the worst case scenario by simulating images with much lower SNRs than those seen with experimental biacetyl MTV images. The effect of SNR on rms displacement error (see (4) and without filtering) is shown in Figure 8. Few spurious correlations as detected for images with SNR h and i were removed from the error calculations. The rms displacement error without filtering rapidly decreased until the image SNR was greater than 1.6, followed by a gradual decline as the image SNR was increased further.

To analyze the effect of line width on displacement accuracy, synthetic images were generated with different LWs

(i.e., 3 to 15 pixels) for a given noise level. It should be noted that, for the same level of noise, SNR value increased with the increase in line width. For example, in the case of SNR f , SNR value increased from 1.5 to 1.9 when the line width was increased from 9 pixels to 11 pixels. Therefore, SNR values A , D , F , and H in Figure 9 and in the rest of this work are the averaged values of SNRs a , d , f , and h , respectively, obtained with all the LWs for a given noise level. In this way, the image SNR h that included an LW of 11 pixels was shown to be 1.6 (Figure 7) and the image SNR H that represents the average of all LWs from 3 to 15 pixels at this noise level was shown to be 1.4 (Figure 9). Figure 9(a) shows that the displacement error increased as SNR decreased and also as the LW increased. The latter observation of displacement error increasing with LW is important in two ways. First, MTV accuracy depends on the presence of sufficient intensity gradients in the source window (recall the discussion on Figure 6). For a given source window size (15×15 in Figure 9(a)), a wider tag line occupies more pixels and increases the possibility of intensity flatness across the window. Figure 9(b) shows the corresponding error levels using a larger source window of 27×27 pixels². The maximum error values for a given image SNR using a larger window reduced by more than half. Also, the slopes of displacement error curves in Figure 9(a) became steeper with LW as the amount of image noise present was higher. Second, the dissociation of N_2O -to-NO depends on the laser energy density which can be increased by narrowing the laser line width. The observations in Figures 9 and 12 could be useful for designing the N_2O MTV optical setup (laser line forming optics) for engine air flow studies.

4.2. Effects of SNR and Line Width on Subpixel Accuracy Using Different Filters. The performance of different filters, discussed in Section 2, is investigated in reducing the displacement error. The set of undelayed and delayed images with an SNR value of F (or 1.6) was used for this comparison study. Figure 10 shows the MTV displacement error levels with different filters of 5×5 window size and for the original images, without filtering, for various line widths. It was observed that when compared to the original images, the mean and Gaussian filters enhanced subpixel accuracy levels for all line widths, while the median filter enhanced the accuracy levels for line widths greater than 9 pixels. It was interesting to observe that the Wiener filter performed similar to or even better than the median filter in some cases (at LW <9 pixels). However, the corresponding filtered image, as in Figure 3(d), showed visually apparent noise levels. This could be due to the presence of sufficient amounts of spatial gradients of intensity field along two orthogonal directions, which is advantageous when using the spatial correlation technique. Overall, the mean filter resulted in the smallest errors for smaller LWs, while the Gaussian filter was superior at LWs greater than 9 pixels followed by the mean filter. Hence, the mean filter is shown to be highly effective in reducing image noise and thus MTV displacement error.

In addition, the mean filter enhanced the displacement accuracies or reduced the rms displacement error for different SNR values from a to i (at a given LW). Figure 11 shows the comparison plot of displacement error without filtering and

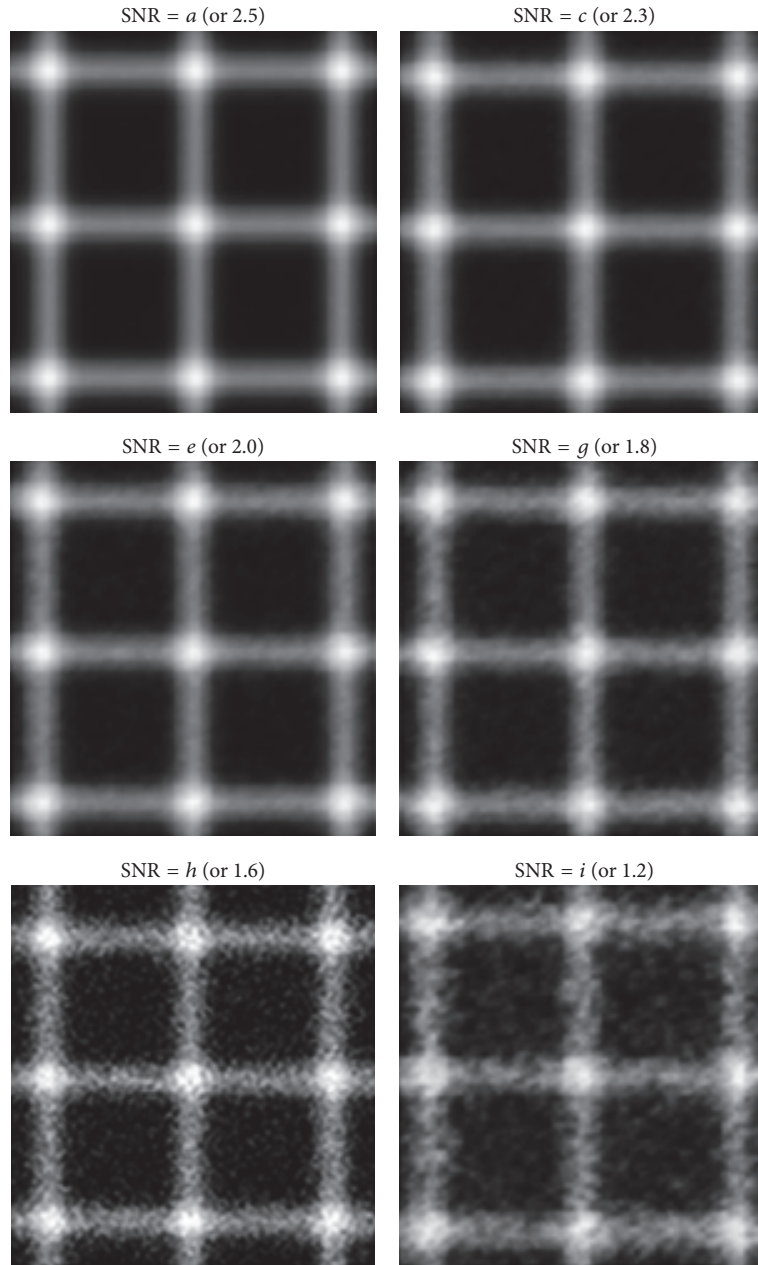


FIGURE 7: Synthetic images of various SNR values with $LW = 11$ pixels.

with mean filter for various SNRs and a line width of 11 pixels. Notice that although the SNR values obtained from image filtering were higher than without filtering, a common x -axis was considered for ease in comparison by choosing the original image SNR values (without filtering). Also, spurious correlations earlier observed with SNR h and i did not occur with the filtered images. Nevertheless, these points were removed while calculating the errors to be consistent while comparing filtered and nonfiltered results. It was observed that the effect of mean filter in reducing the 95% error level was more apparent for highly noisy images than for less noisy images. However, the least noisy image or the image with highest SNR value considered in this work showed higher

displacement error with filtering than without filtering. This can be noted as the limiting case of the mean filter. The mean filter stretches the signal levels, thereby attenuating signal peak intensities (at nodes), while the task of filtering noise is minimal due to lack of significant noise in the original image.

Figure 12 shows the error levels after employing a 5×5 mean filter on the undelayed and delayed images. The corresponding error levels without filtering as seen in Figure 9 are included here for direct comparison. Applying a mean filter to the original images reduced the displacement errors, with exceptions observed for lower line widths. The error levels were higher with filtered images for laser line widths thinner than 5 pixels, as seen in the magnified section (Figure 12(b)).

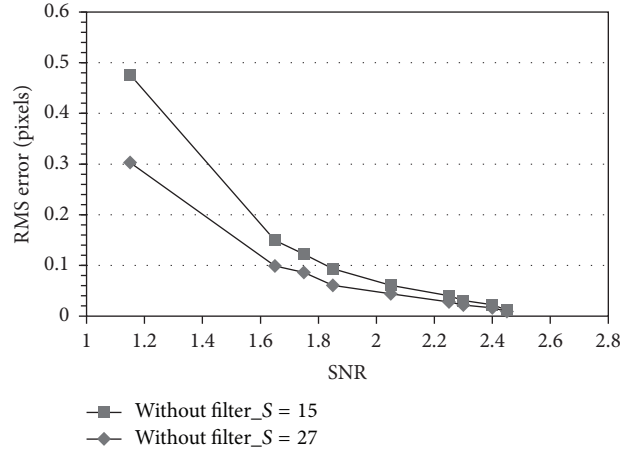


FIGURE 8: Effect of image SNR on rms displacement error without filtering using 15×15 and 27×27 source window sizes. Here $LW = 11$ pixels.

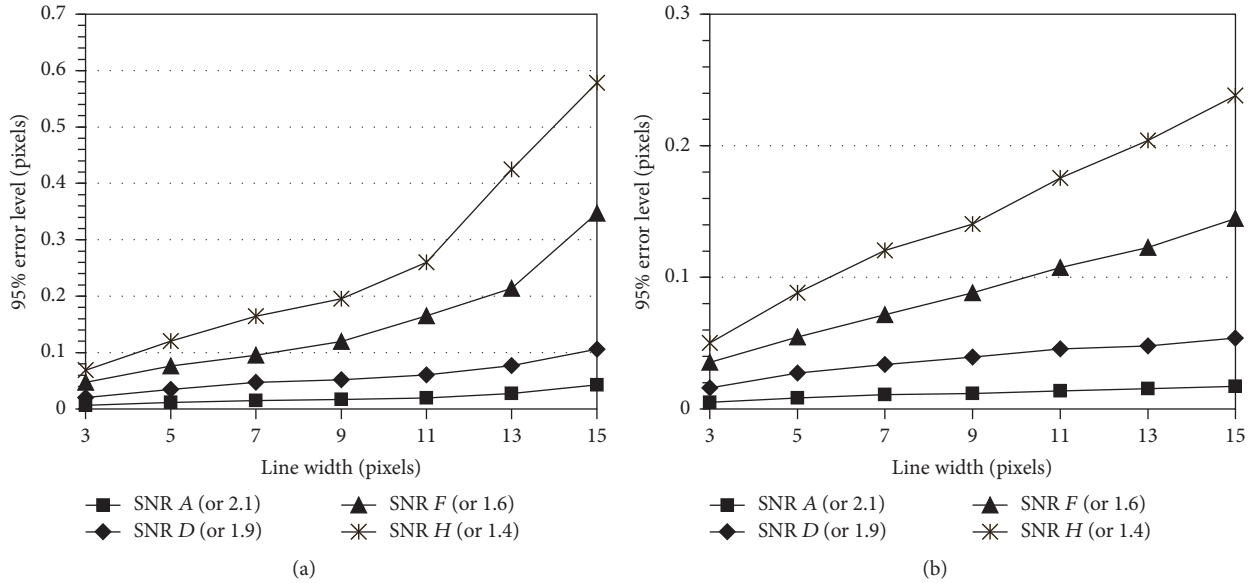


FIGURE 9: Displacement error levels (without filtering) for different SNR values and various line widths using a source window size: (a) 15×15 and (b) 27×27 .

Figure 13 demonstrates the effect of mean filter on processing images of different LWs. Additional grid lines were included to enhance the visualization of filtering effect on different line widths. It was observed that the mean-filtered images smoothed both signal intensities and image noise. The former feature of attenuating the signal is more apparent at $LW = 3$. This illustration further adds to the understanding of why error levels increased for LW below 5 pixels, as seen in Figure 12.

The 95% error level values with and without filtering are tabulated in Figure 14. The effectiveness of the spatial mean filter in reducing the error levels depended on both image SNR and line width. The mean filter showed a significantly positive impact on error reduction for lower SNR images (e.g., error level of 0.7 without filter \rightarrow 0.2 with filter for $LW = 15$, $SNR = H$) compared to that for a higher SNR image

(0.04 \rightarrow 0.02 for $LW = 15$, $SNR = A$). On the other hand, error levels were aggravated with higher SNR images until the line width was greater than 9 pixels. This line width limit was also seen in [39]. The line width after which the mean filter enhanced the MTV displacement subpixel accuracy at each SNR value is highlighted by underlining the error values in Figure 14. From these observations it is realized that the thicker the MTV laser lines are in a high quality mean-filtered image, the better the subpixel accuracy is expected to be. An alternate way to show the limit of line width below which mean filter worsens the subpixel accuracy is by introducing a normalized error parameter (NE):

$$NE = \frac{(95\% \text{ error level}_{w/o \text{ filter}} - 95\% \text{ error level}_{with \text{ filter}})}{(95\% \text{ error level}_{w/o \text{ filter}})} \quad (6)$$

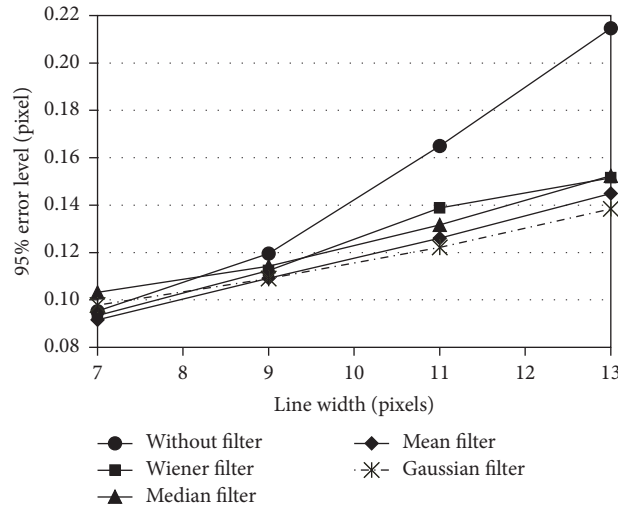


FIGURE 10: Displacement error levels with filtered undelayed and delayed images using different filters for image SNR F (or 1.6).

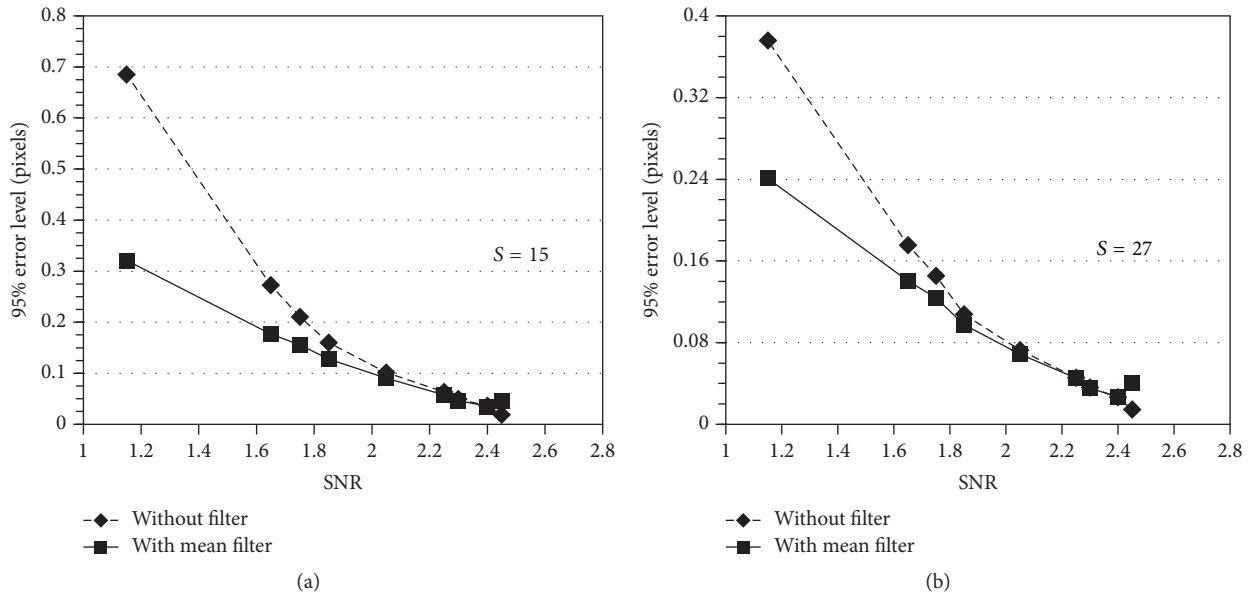


FIGURE 11: Effect of mean filter in reducing displacement error for different image SNRs using 15×15 (a) and 27×27 (b) source window, with $LW = 11$ pixels.

Figure 15 illustrates the efficacy of the proposed parameter. Here, a negative value of NE indicates that the error was increased using a particular filter, mean 5×5 filter in this case, whereas a positive value indicates that the error decreased with the filter application. This plot readily shows the line width limits beyond which applying mean filter reduced the errors for SNR D , 9, SNR F , 9, and SNR H , 7. Thus, the normalized error parameter readily provides the aforementioned line width limits without the need to plot curves of error levels with and without filtering (Figure 12) or list the individual error values (Figure 14).

In addition, the effect of mean filter window size on the resulting displacement error is analyzed by considering one of the less noisy images (original image SNR = 1.9) and

different line widths. As seen in Figure 16(a), the 95% error level increased with the window size k . The mean filter, when applied for a relatively larger neighborhood window, resulted in what we describe as “signal stretching.” Figure 16(b) shows the mean-filtered images that were used in the spatial correlation technique to attain the MTV displacements and the corresponding errors. The signal stretching characteristic is noticed by observing how the grid nodes were enlarged and MTV lines were widened or stretched, thereby representing a pseudo intensity distribution. As the filter size increased, the lines became wider and the image became blurred. The highly blurred images with larger line widths reduced the effect of filter size on displacement error, especially for $k = 9$ and 7 with $LW = 11$ as noted in Figure 16(a). The features

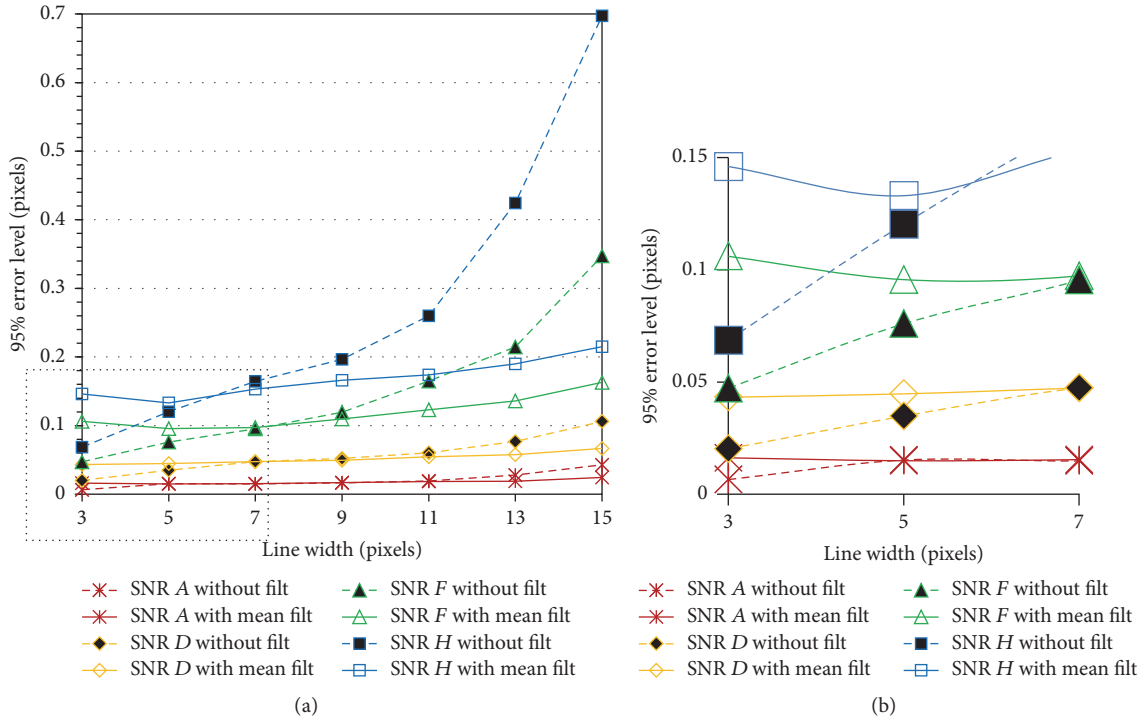


FIGURE 12: (a) Error levels for different SNR values and various line widths with and without employing a 5×5 window mean filter and (b) magnified view of the section highlighted in (a).

of signal stretching and independence of filter size for LWs greater than 11 pixels were also noted in [39]. For more noisy images (not shown here), it was expected and confirmed that the displacement error values were higher compared to those for the less noisy images. In addition, the effect of filter size on displacement error was much less for larger line widths.

5. Preprocessing Experimental MTV Images Using Filters

The spatial and frequency domain filters discussed in this work were applied to biacetyl MTV images. Figure 17(a) shows the MTV delayed image without any filtering applied and will be called hereafter as the “baseline” image. This image was recorded previously along the in-cylinder tumble plane that symmetrically bisects the intake and exhaust valves of an optical engine. Details of the experimental setup can be found in related works [29, 30]. The engine was operated at 2500 rpm and the MTV images were acquired at 107 CAD before TDC during compression stroke. The piston surface was located at the bottom of the MTV grid as indicated with the dashed line in Figure 17(a). Figures 17(b)–17(d) show the MTV delayed image on applying mean, Gaussian, and median filters, respectively. These filtered images demonstrated the intensity attenuation and noise behavior as observed from the simulated images: The mean filter reduced the noise level while simultaneously attenuating the signal pixel intensities (Figure 17(b)). Median filter retained the intensities of actual laser grid and the lines are clearer than with other filters (Figure 17(c)). However, significant

amount of “salt-and-pepper” noise remained in the filtered image. Gaussian filtered image exhibited reduced noise levels similar to those in the mean-filtered image while retaining the grid intensities similar to those seen with median filter (Figure 17(d)). The effects of these filters on MTV measurement accuracy were quantified by evaluating the grid displacements using spatial correlation technique within the region highlighted in Figure 17(a).

Figure 18 shows the corresponding velocity vectors plotted at these grid points using the baseline undelayed and delayed images (not shown here; delay time = $12 \mu\text{s}$). The flow direction was influenced by the piston surface wall interaction as indicated by the upward-pointing curved vectors near the bottom-right of the vector plot. It should be noted that this vector plot is away from and does not include the piston boundary as highlighted in Figure 17(a). In addition, the whole flow field was redirected from the almost vertically downward movement during intake stroke to a more lateral motion (Figure 18) due to upward moving piston during compression stroke.

The displacement of the baseline delayed image was considered as the reference value and the *noise reduction index* (NRI) due to the filtered delayed images (mean, Gaussian, and median) was analyzed from the deviation:

$$\text{NRI} = \sqrt{(\delta X_{\text{filter}} - \delta X_{\text{base}})^2 + (\delta Y_{\text{filter}} - \delta Y_{\text{base}})^2}, \quad (7)$$

where δX and δY are subpixel displacements of grid points in “X” and “Y” direction, and the subscripts filter and base indicate if these values were taken from the baseline

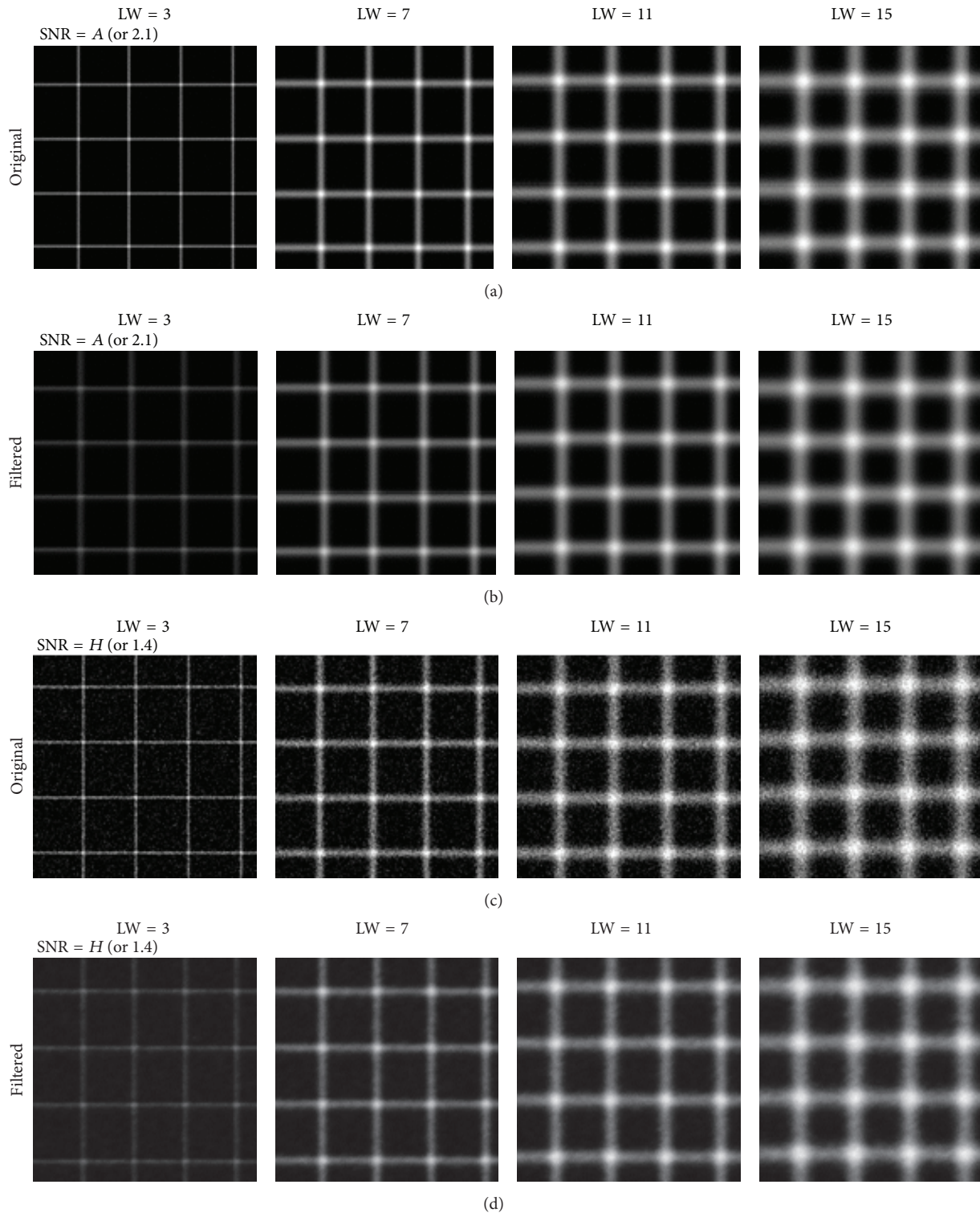


FIGURE 13: Original (a and c) and mean-filtered images (b and d) for selected SNRs and different line widths at each SNR.

image or filtered image. The statistical relation in (7) is termed as the noise reduction index because the laser line width in the experimental MTV images was 11 pixels and it was determined that the mean filter would reduce the measurement error at this LW (see Figure 14). The LW

limits for median and Gaussian filters, however, were not determined in this work and are assumed here to share the same values as for the mean filter.

The error values were calculated for an 8×8 grid (64 grid points). A few spurious correlations were detected which

LW	SNR = A (2.1)		SNR = D (1.9)		SNR = F (1.6)		SNR = H (1.4)	
	Err. 95% (w/o filter)	Err. 95% (filtered)						
3	0.0065	0.0162	0.0202	0.0432	0.0472	0.106	0.0686	0.146
5	0.0152	0.0149	0.0348	0.0447	0.0759	0.0956	0.1203	0.133
7	0.0148	0.0154	0.0473	0.0473	0.0953	0.0973	0.1646	0.153
9	0.0167	0.0169	0.052	0.0495	0.1196	0.1096	0.1964	0.166
11	0.0193	0.0183	0.0605	0.0544	0.165	0.123	0.2599	0.174
13	0.0277	0.0187	0.0768	0.0578	0.2146	0.136	0.4246	0.19
15	0.0428	0.0244	0.106	0.0667	0.3472	0.163	0.6971	0.215

FIGURE 14: Pixel error levels for various line widths and different image SNRs.

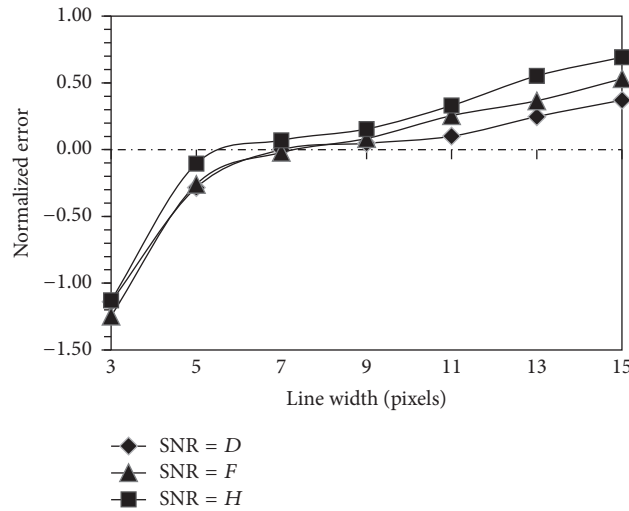


FIGURE 15: Normalized error level for different image SNRs and various line widths.

were removed by applying an error processing algorithm in MATLAB code. Figure 19 shows the plotted values of deviations, after removing spurious correlations, for all the grid points. With the baseline displacements as reference, the displacements calculated from median-filtered image were closer to those of the baseline with an average NRI value of 0.16 pixels for the chosen laser grid. On the other hand, displacements calculated from mean-filtered image showed the highest noise reduction capacity (average NRI of 0.4 pixels) among all the filters.

6. Conclusions

Realizing the capability of N_2O molecular tagging velocimetry to measure air flows, the authors here investigated the potential application of N_2O MTV for in-cylinder air flow measurements. Based on the working principle of N_2O MTV and the related optical setup for in-cylinder MTV grid formation, it was identified that the image SNR and laser line width depend on several working parameters (e.g., laser energy density and NO fluorescence signal). Hence, a parametric study of image SNR and MTV laser line width was made to understand their effects on the subpixel accuracy levels of flow displacements with and without image preprocessing. Although the prime focus of this work is

on N_2O MTV, the current discussions can be applied to other MTV techniques such as biacetyl MTV because both techniques share identical laser grid setup. Synthetic MTV images having different levels of Gaussian white noise were generated for this work. The rms displacement error was used to characterize the subpixel accuracy, apart from the 95% error level that was used to compare the current results with those in previous works. The rms displacement error without filtering rapidly decreased until the image SNR was greater than 1.6, followed by a gradual decline as the image SNR was increased further. The 95% error level (confidence interval) and its slope increased and became steeper, respectively, as SNR decreased and also as line width increased. One of the key aspects to minimize noise or spurious detection while applying MTV for in-cylinder flow measurements is to select proper source window size for spatial correlations. This was demonstrated in this work wherein the error levels were reduced by more than half when switching from a source window of 15×15 to 27×27 pixels².

In the second part of this work, the effect of image preprocessing on error reduction was analyzed using a Gaussian filter and various spatial filters such as mean, median, and Wiener filter. It was observed that the mean filter was effective in removing visual noise and increased the image SNR, while the median- and Wiener-filtered images contained visibly

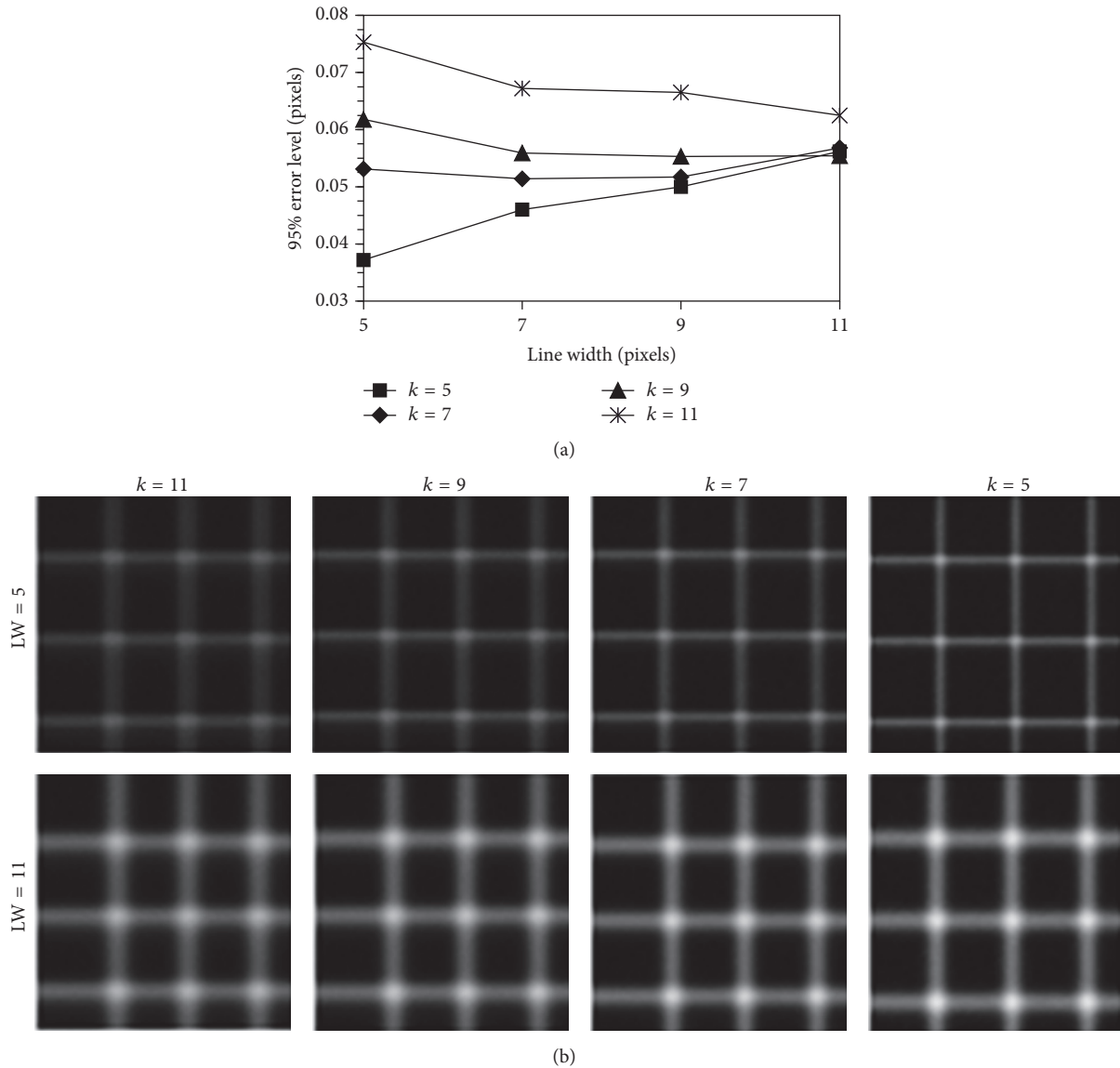


FIGURE 16: (a) RMS displacement error and (b) mean-filtered simulated images of different line widths and filter window sizes for less noisy image set.

apparent levels of noise. When compared to the Gaussian filter, the mean filter resulted in smaller error levels for $LW < 9$ pixels and slightly higher error levels for $LW > 9$ pixels, in agreement with results from a similar work. From a priori knowledge of simulated image noise distribution (Gaussian white noise), the performance of the mean filter indicates that it is very effective in enhancing the displacement subpixel accuracy. Also, the mean filter reduced the displacement error significantly for more noisy images compared to that for less noisy images. However, the least noisy image showed higher displacement error with filtering than without filtering. This was attributed to the intensity attenuation as a result of signal stretching, which was more apparent for $LW < 5$ pixels. The limit of line width below which mean filter worsened the subpixel accuracy moved from 11 pixels to 7 pixels as the image noise increased. In addition, error levels increased as

the filter size was increased and became almost independent of filter size for $LW \geq 11$ as also seen in previous works. The simulation results were further validated using experimental images taken along the in-cylinder tumble plane.

Abbreviations

Δt :	Delay time
k :	Mean filter size
R :	Spatial correlation coefficient
S :	Source window size
CAD:	Crank angle degree
LDV:	Laser Doppler velocimetry
LW:	Line width
MRV:	Magnetic resonance velocimetry
MTV:	Molecular tagging velocimetry

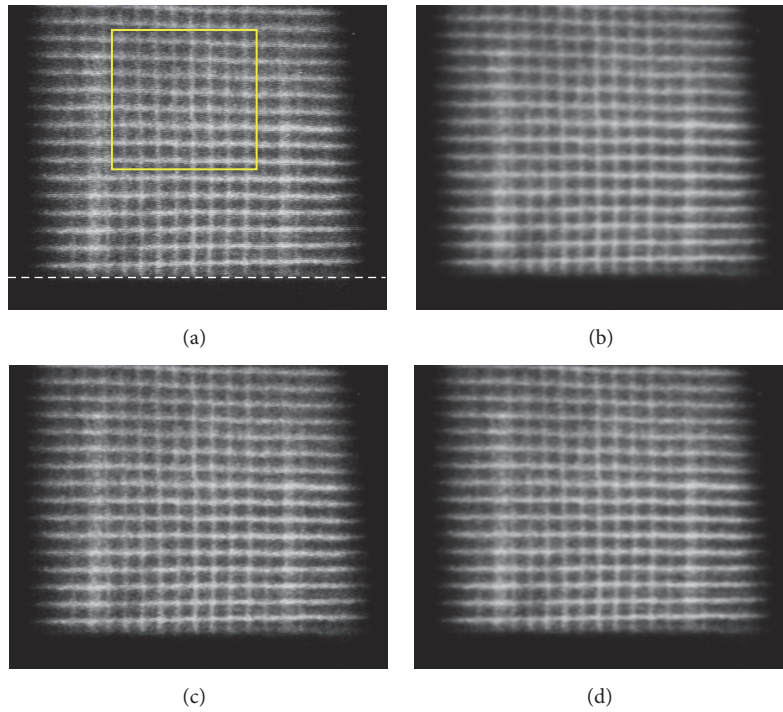


FIGURE 17: (a) Baseline delayed biacetyl MTV image without any filtering and (b) mean-filtered, (c) median-filtered, and (d) Gaussian filtered delayed image. The baseline image was taken at 107 CAD before TDC during compression stroke.

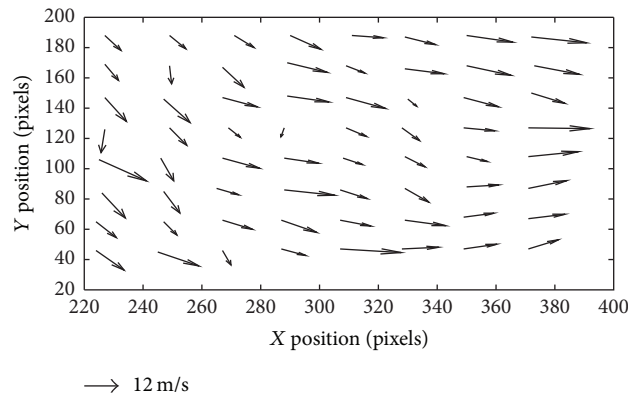


FIGURE 18: Velocity vector field along an in-cylinder tumble plane at 107 CAD before TDC during compression stroke at 2500 rpm.

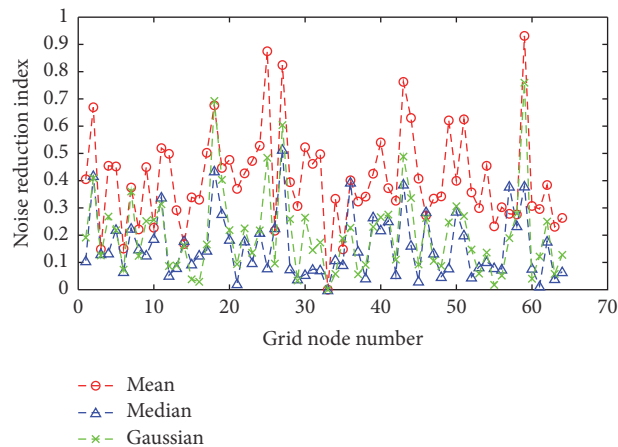


FIGURE 19: Eccentricity values of flow displacements using different image filters with reference being the baseline unfiltered image displacements.

N₂O: Nitrous oxide
 NO: Nitric oxide
 PIV: Particle image velocimetry
 rms: Root-mean-square
 SNR: Signal-to-noise ratio
 TDC: Top dead center.

Competing Interests

The authors declare that there is no conflict of interests regarding the publication of this paper.

Acknowledgments

The authors would like to express their gratitude to Professor Manooch Koochesfahani at MSU for providing selected reference works and valuable feedback on the presentation of the subject.

References

- [1] C. Arcoumanis and J. H. Whitelaw, "Fluid mechanics of internal combustion engines—a review," *Proceedings of the Institution of Mechanical Engineers, Part C: Journal of Mechanical Engineering Science*, vol. 201, no. 1, pp. 57–74, 1987.
- [2] J. B. Heywood, "Fluid motion within the cylinder of internal combustion engines—the 1986 freeman scholar lecture," *Journal of Fluids Engineering, Transactions of the ASME*, vol. 109, no. 1, pp. 3–35, 1987.
- [3] T. Honda, M. Kawamoto, H. Katashiba, M. Sumida, and N. Fukutomi, "A study of mixture formation and combustion for spray guided DISI," SAE Technical Paper 2004-01-0046, SAE International, 2004.
- [4] C. Schwarz, E. Schünemann, B. Durst, J. Fischer, and A. Witt, "Potentials of the spray-guided BMW DI combustion system," SAE Technical Paper 2006-01-1265, SAE International, 2006.
- [5] M. Sjöberg, W. Zeng, and D. Reuss, "Role of engine speed and in-cylinder flow field for stratified and well-mixed DISI engine combustion using E70," *SAE International Journal of Engines*, vol. 7, no. 2, pp. 642–655, 2014.
- [6] H.-E. Albrecht, N. Damaschke, M. Borys, and C. Tropea, *Laser Doppler and Phase Doppler Measurement Techniques*, Springer Science & Business Media, 2013.
- [7] M. J. Hall and F. V. Bracco, "A study of velocities and turbulence intensities measured in firing and motored engines," *SAE Technical Papers*, Article ID 870453, 1987.
- [8] P. Miles, M. Megerle, Z. Nagel, R. D. Reitz, M.-C. D. Lai, and V. Sick, "An experimental assessment of turbulence production, reynolds stress and length scale (Dissipation) modeling in a swirl-supported di diesel engine," *SAE Technical Papers*, 2003.
- [9] G. Pitcher and G. Wigley, "A comparison between in-cylinder steady flow and motored engine air velocities using LDA," in *Proceedings of the 16th International Symposium on Applications of Laser Techniques to Fluid Mechanics*, Lisbon, Portugal, July 2012.
- [10] D. L. Reuss, R. J. Adrian, C. C. Landreth, D. T. French, and T. D. Fansler, "Instantaneous planar measurements of velocity and large-scale vorticity and strain rate in an engine using particle-image velocimetry," *SAE Technical Papers*, 1989.
- [11] M. Kim, S. Lee, and W. Kim, "Tumble flow measurements using three different methods and its effects on fuel economy and emissions," in *Proceedings of the Spring Technical Conference of the ASME Internal Combustion Engine Division*, pp. 267–277, Aachen, Germany, May 2006.
- [12] C. Disch, H. Kubach, U. Spicher, J. Pfeil, F. Altenschmidt, and U. Schaupp, "Investigations of spray-induced vortex structures during multiple injections of a DISI engine in stratified operation using high-speed-PIV," *SAE Technical Papers*, vol. 2, 2013.
- [13] S. Jarvis, T. Justham, A. Clarke, C. P. Garner, G. K. Hargrave, and N. A. Halliwell, "Time resolved digital PIV measurements of flow field cyclic variation in an optical IC engine," *Journal of Physics: Conference Series*, vol. 45, no. 1, pp. 38–45, 2006.
- [14] H. Chen, M. Xu, and D. L. Hung, "Analyzing in-cylinder flow evolution and variations in a spark-ignition direct-injection engine using phase-invariant proper orthogonal decomposition technique," SAE Technical Paper 2014-01-1174, SAE International, 2014.
- [15] R. J. Adrian and J. Westerweel, *Particle Image Velocimetry*, Cambridge University Press, 2011.
- [16] C. Tropea, A. L. Yarin, and J. F. Foss, *Springer Handbook of Experimental Fluid Mechanics*, Springer, Berlin, Germany, 2007.
- [17] D. Freudenhammer, E. Baum, B. Peterson, B. Böhm, B. Jung, and S. Grundmann, "Volumetric intake flow measurements of an IC engine using magnetic resonance velocimetry," *Experiments in Fluids*, vol. 55, no. 5, article 1724, pp. 1–18, 2014.
- [18] D. Freudenhammer, B. Peterson, C.-P. Ding, B. Boehm, and S. Grundmann, "The influence of cylinder head geometry variations on the volumetric intake flow captured by magnetic resonance velocimetry," *SAE International Journal of Engines*, vol. 8, no. 4, pp. 1826–1836, 2015.
- [19] M. Bruschi, D. Freudenhammer, W. B. Buchenberg, H.-P. Schiffer, and S. Grundmann, "Estimation of the measurement uncertainty in magnetic resonance velocimetry based on statistical models," *Experiments in Fluids*, vol. 57, no. 5, article 83, 13 pages, 2016.
- [20] S. O. Warner and B. L. Smith, "Autocorrelation-based estimate of particle image density for diffraction limited particle images," *Measurement Science and Technology*, vol. 25, no. 6, Article ID 065201, 2014.
- [21] B. M. Wilson and B. L. Smith, "Uncertainty on PIV mean and fluctuating velocity due to bias and random errors," *Measurement Science and Technology*, vol. 24, no. 3, Article ID 035302, 2013.
- [22] P. Abraham, D. Reuss, and V. Sick, "High-speed particle image velocimetry study of in-cylinder flows with improved dynamic range," *SAE Technical Papers*, vol. 2, 2013.
- [23] E. Baum, B. Peterson, B. Böhm, and A. Dreizler, "On the validation of les applied to internal combustion engine flows: Part 1: comprehensive experimental database," *Flow, Turbulence and Combustion*, vol. 92, no. 1-2, pp. 269–297, 2014.
- [24] J. Westerweel, G. E. Elsinga, and R. J. Adrian, "Particle image velocimetry for complex and turbulent flows," *Annual Review of Fluid Mechanics*, vol. 45, pp. 409–436, 2013.
- [25] T. V. Overbrueggen, M. Klaas, B. Bahl, and W. Schroeder, "Tomographic particle-image velocimetry analysis of in-cylinder flows," *SAE International Journal of Engines*, vol. 8, no. 3, pp. 1447–1467, 2015.
- [26] R. Vedula, M. Mittal, and H. J. Schock, "Molecular tagging velocimetry and its application to in-cylinder flow measurements," *Journal of Fluids Engineering*, vol. 135, no. 12, Article ID 121203, 2013.

- [27] A. H. Epstein, "Quantitative density visualization in a transonic compressor rotor," *Journal of Engineering for Power*, vol. 99, no. 3, pp. 460–475, 1977.
- [28] B. Hiller, R. A. Booman, C. Hassa, and R. K. Hanson, "Velocity visualization in gas flows using laser-induced phosphorescence of biacetyl," *Review of Scientific Instruments*, vol. 55, no. 12, pp. 1964–1967, 1984.
- [29] M. M. Ismailov, H. J. Schock, and A. M. Fedewa, "Gaseous flow measurements in an internal combustion engine assembly using molecular tagging velocimetry," *Experiments in Fluids*, vol. 41, no. 1, pp. 57–65, 2006.
- [30] M. Mittal and H. J. Schock, "A study of cycle-to-cycle variations and the influence of charge motion control on in-cylinder flow in an IC engine," *Journal of Fluids Engineering, Transactions of the ASME*, vol. 132, no. 5, pp. 0511071–0511078, 2010.
- [31] M. Mittal, R. Sadr, H. J. Schock, A. Fedewa, and A. Naqwi, "In-cylinder engine flow measurement using stereoscopic molecular tagging velocimetry (SMTV)," *Experiments in Fluids*, vol. 46, no. 2, pp. 277–284, 2009.
- [32] P. M. Danehy, S. O'Byrne, A. F. P. Houwing, J. S. Fox, and D. R. Smith, "Flow-tagging velocimetry for hypersonic flows using fluorescence of nitric oxide," *AIAA Journal*, vol. 41, no. 2, pp. 263–271, 2003.
- [33] A. G. Hsu, R. Srinivasan, R. D. W. Bowersox, and S. W. North, "Two-component molecular tagging velocimetry utilizing NO fluorescence lifetime and NO₂ photodissociation techniques in an underexpanded jet flowfield," *Applied Optics*, vol. 48, no. 22, pp. 4414–4423, 2009.
- [34] A. M. ElBaz and R. W. Pitz, "N₂O molecular tagging velocimetry," *Applied Physics B: Lasers and Optics*, vol. 106, no. 4, pp. 961–969, 2012.
- [35] C. P. Gendrich and M. M. Koochesfahani, "A spatial correlation technique for estimating velocity fields using molecular tagging velocimetry (MTV)," *Experiments in Fluids*, vol. 22, no. 1, pp. 67–77, 1996.
- [36] R. D. Keane and R. J. Adrian, "Theory of cross-correlation analysis of PIV images," *Applied Scientific Research*, vol. 49, no. 3, pp. 191–215, 1992.
- [37] B. Stier and M. M. Koochesfahani, "Molecular Tagging Velocimetry (MTV) measurements in gas phase flows," *Experiments in Fluids*, vol. 26, no. 4, pp. 297–304, 1999.
- [38] Q. Zheng and J. C. Klewicki, "A fast data reduction algorithm for molecular tagging velocimetry: the decoupled spatial correlation technique," *Measurement Science and Technology*, vol. 11, no. 9, pp. 1282–1288, 2000.
- [39] M. Caso and D. Bohl, "Error reduction in molecular tagging velocimetry via image preprocessing," *Experiments in Fluids*, vol. 55, no. 8, article 1802, 2014.
- [40] O. Dietrich, J. G. Raya, S. B. Reeder, M. F. Reiser, and S. O. Schoenberg, "Measurement of signal-to-noise ratios in MR images: influence of multichannel coils, parallel imaging, and reconstruction filters," *Journal of Magnetic Resonance Imaging*, vol. 26, no. 2, pp. 375–385, 2007.
- [41] I. T. Young, J. J. Gerbrands, and L. J. Van Vliet, *Fundamentals of Image Processing*, Delft University of Technology, Delft, The Netherlands, 1998.
- [42] G. C. Rafael and E. W. Richards, "Image smoothing using frequency domain filters," in *Digital Image Processing*, Prentice Hall, Upper Saddle River, NJ, USA, 2008.
- [43] G. C. Rafael and E. W. Richards, "Smoothing spatial filters," in *Digital Image Processing*, Prentice Hall, Upper Saddle River, NJ, USA, 2008.
- [44] D. Dussault and P. Hoess, "Noise performance comparison of ICCD with CCD and EMCCD cameras," in *Proceedings of the Optical Science and Technology, the SPIE 49th Annual Meeting*, International Society for Optics and Photonics, 2004.

Research Article

Influence of Advanced Injection Timing and Fuel Additive on Combustion, Performance, and Emission Characteristics of a DI Diesel Engine Running on Plastic Pyrolysis Oil

Ioannis Kalargaris, Guohong Tian, and Sai Gu

Faculty of Engineering and Physical Sciences, University of Surrey, Guildford GU2 7XH, UK

Correspondence should be addressed to Sai Gu; sai.gu@surrey.ac.uk

Received 26 October 2016; Accepted 25 December 2016; Published 15 February 2017

Academic Editor: Constantine D. Rakopoulos

Copyright © 2017 Ioannis Kalargaris et al. This is an open access article distributed under the Creative Commons Attribution License, which permits unrestricted use, distribution, and reproduction in any medium, provided the original work is properly cited.

This paper presents the investigation of engine optimisation when plastic pyrolysis oil (PPO) is used as the primary fuel of a direct injection diesel engine. Our previous investigation revealed that PPO is a promising fuel; however the results suggested that control parameters should be optimised in order to obtain a better engine performance. In the present work, the injection timing was advanced, and fuel additives were utilised to overcome the issues experienced in the previous work. In addition, spray characteristics of PPO were investigated in comparison with diesel to provide in-depth understanding of the engine behaviour. The experimental results on advanced injection timing (AIT) showed reduced brake thermal efficiency and increased carbon monoxide, unburned hydrocarbons, and nitrogen oxides emissions in comparison to standard injection timing. On the other hand, the addition of fuel additive resulted in higher engine efficiency and lower exhaust emissions. Finally, the spray tests revealed that the spray tip penetration for PPO is faster than diesel. The results suggested that AIT is not a preferable option while fuel additive is a promising solution for long-term use of PPO in diesel engines.

1. Introduction

Human developments have been coupled with the evolution of the extraction, use, and disposal of natural resources. The way in which waste is disposed has changed dramatically over the last decades, as have attitudes towards waste reduction, reuse, and recycling, as well as recovering energy from waste. Energy from waste can be recovered through the pyrolysis process which converts the waste into oil and gas. Plastic is a type of waste that is plentiful and can be used effectively due to the high energy content. The conversion products can be used in internal combustion engines to produce power and heat. The effect of plastic pyrolysis oil (PPO) in diesel engines has been studied by various authors mainly in blends with diesel in single cylinder engines [1–8]. The investigations showed that diesel engines can run stable on medium PPO-diesel blend rates but with lower brake thermal efficiency and higher exhaust emissions (NO_x, UHC, and CO). Due to the lower quality of the PPO in comparison with diesel fuel,

one or a combination of the following ways/processes has to be applied in order to achieve stable engine performance at higher PPO-diesel blend rates or without diesel: upgrade of the oil, modification of the engine, and addition of fuel additives.

One of the most important engine parameters is the injection timing. The effect of injection timing (IT) in alternative fuels based on waste plastics has been studied in single cylinder diesel engines and the results are promising. Mani and Nagarajan [9] have investigated the effect of retarded IT on diesel engines running on waste plastic pyrolysis oil (PPO). The results showed that the unburned hydrocarbon, oxides of nitrogen, and carbon monoxide emissions are decreasing while the carbon dioxide emission and brake thermal efficiency are increasing. Another research on a fuel blend of 20% tyre pyrolysis oil and 80% of jatropha ester revealed that the advanced IT results in lower fuel consumption, carbon monoxide, unburned hydrocarbon, and particulate matter emissions whereas the oxides of nitrogen are increasing

[10]. Finally, Wamankar and Murugan conducted a research using a blend of 90% diesel and 10% waste tyre oil. The results showed that the brake thermal efficiency and oxides of nitrogen emission were higher while the fuel consumption, carbon monoxide, and unburned hydrocarbon emissions were lower when running on advanced IT [11].

On the other hand, fuel additives are preferable in the case of good quality oil that needs to boost a property such as cetane number or lubricity in order to improve the engine performance. Diethyl ether is an organic compound with high cetane number, which has been used in research as a cetane number improver. Devaraj et al. [12] investigated the effect of diethyl ether on waste plastic pyrolysis oil used as fuel for a single cylinder diesel engine. The results showed reduction in ignition delay period, heat release rate, cylinder peak pressure, carbon monoxide, carbon dioxide, and oxides of nitrogen emissions while the brake thermal efficiency and unburned hydrocarbon emissions were increased. Another research on tyre pyrolysis oil blended with diethyl ether on a single cylinder research engine revealed that the ignition delay period, unburned hydrocarbon, and oxides of nitrogen emissions are reducing with the addition of diethyl ether whereas the brake thermal efficiency is increasing [13].

What has not been investigated yet in larger diesel engines is the advanced IT by using PPO in blends with diesel and the use of a fuel additive to improve the engine's performance when running on PPO. Moreover, the spray characteristics from oil that derives from the pyrolysis of plastics have not been determined yet. Our previous investigation on the use of PPO in a four-cylinder diesel engine revealed that there is longer ignition delay and higher heat release rate (HRR) in comparison with diesel [14]. In order to reduce the ignition delay period and achieve lower HRR the advanced IT and a commercial fuel additive were tested. An additional investigation on the spray characteristics of the PPO was carried out in parallel with the engine tests to provide more insight knowledge for engine control strategy optimisation.

2. Materials and Methods

2.1. Conversion Process and Fuel Properties. The conversion of the waste plastics into oil, gas, and char is taking place in the pyrolysis plant. More specifically, the plant consists of the primary and secondary chambers, where the plastics are purged with carbon dioxide to ensure that no oxygen is transferred into the next chamber which is the conversion chamber. The conversion chamber is maintained at a temperature of 900°C and the plastics are converted into gas and char. Finally, the gas is passed into a condenser, where it is cooled, and pyrolysis oil is separated out. The basic properties of PPO benchmarked with diesel and the test methods which were used to determine them are presented in Table 1. More information can be found about the plastics, produced oil, and gas composition in our previous publication [14].

Although the precise cetane number of the PPO is not provided in the table, it was clearly observed from our previous investigation that the combustion delay was considerably extended with higher PPO blending ratio, which suggests that PPO has lower cetane number than diesel [14].

TABLE 1: PPO and diesel properties.

Property	Method	PPO	Diesel
Density@15°C (kg/l)	ASTM D4052	0.9813	0.8398
Kinematic viscosity@40°C (cSt)	IP 71	1.918	2.62
Flash point (°C)	ASTM D93	13	59.5
Aromatic content (%)	IP 391	65.5	29.5
Acid number (mg KOH/g)	IP 139	41	0
LHV (MJ/kg)	ASTM D240	38.300	42.900
Water content (mg/kg)	ASTM D6304	1190	65
Ash content (wt.%)	IP 391	0.166	<0.001
Carbon residue (wt.%)	ASTM D4530	4.83	<0.01
Hydrogen content (wt.%)	ASTM D5291	8.5	13.38
Carbon content (wt.%)	ASTM D5291	87.9	86.57
Oxygen content (wt.%)	ASTM D5622	3.3	0.05
Sulphur content (wt.%)	ASTM D5453	0.155	0.0014
Nitrogen content (mg/kg)	ASTM D4629	820	44

TABLE 2: Fuel additive composition.

Compound	Quantity (% wt)
Petroleum naphtha	29–38
2-Ethylhexanol	16–24.25
2-Ethylhexyl nitrate	7.75–15.5
1,2,4-Trimethylbenzene	7.75–15.5
1,3,5-Trimethylbenzene	0.775–3.875
Propylene glycol ether	0.775–3.875
Xylene	0.8–4
Trimethylbenzene	7.75–15.5
1,2,3-Trimethylbenzene	0.8–4
Soy methyl ester	5

In order to reduce the ignition delay period, the cetane number of the fuel should be increased. One of the main cetane number improver additives manufactured today is the 2-ethylhexyl nitrate (2-EHN). It should be mentioned that 2-EHN can reduce lubricity so it is important to add a lubricant additive. Table 2 shows the composition of the commercial fuel additive that was used in the experiments. The commercial fuel additive was chosen according to the primary functions of reducing the ignition delay period (cetane number improver), increasing the injectors' lubrication, and cleaning and removing the deposits from the combustion chambers.

2.2. Diesel Engine Experimental Setup. The diesel engine that is used to conduct the experiments is a four-cylinder, direct injection, turbocharged water-cooled diesel engine. Figure 1 presents the schematic layout of the experimental setup and Table 3 shows the engine's specifications. The engine is mated to an alternator and then to a load bank to control the load of

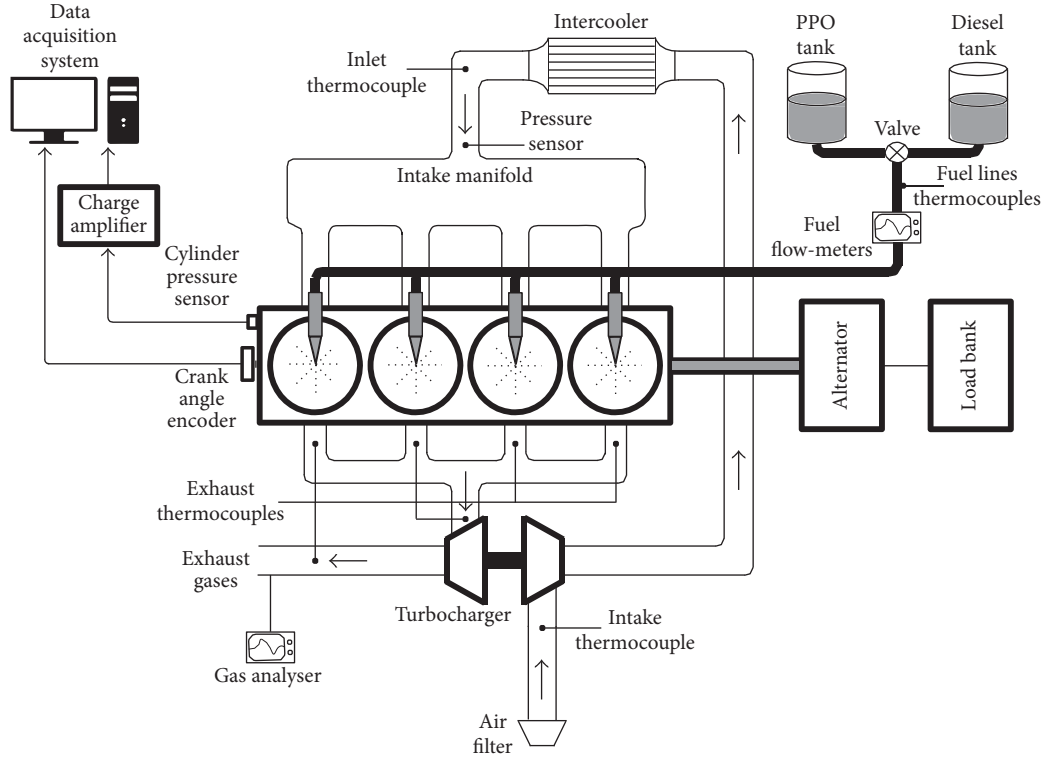


FIGURE 1: Schematic layout of the experimental setup.

TABLE 3: Test engine specifications.

Brand	AKSA
Model	A4CRX46TI
Compression ratio	17 : 1
Displacement	4.58 l
Rated power	68 kW
Rated speed	1500 rpm
Injection pressure	240 bar
Bore	110 mm
Stroke	125 mm

the engine. Furthermore, several sensors are used to monitor the engine's performance and a gas analyser that can measure the exhaust emissions (CO, CO₂, NO_x, and UHC) as it can be seen in Figure 1.

The engine was started and run for 30 minutes on diesel to warm-up and stabilise the oil and coolant temperatures and then it was switched on the desired fuel blend and run for 5 minutes before the data acquisition was started. The flow-meter measurements, manifold pressure, temperatures, and exhaust emissions data were taken for a period of five minutes and the average values were calculated. As regards the combustion analysis, 100 consecutive cycles were acquired from the in-cylinder pressure sensor and the average was calculated. In addition, the heat release rate was calculated

from (1) by using the in-cylinder pressure data and the crank angle encoder readings.

$$\frac{dQ}{d\theta} = \frac{\gamma}{\gamma - 1} p \frac{dV}{d\theta} + \frac{1}{\gamma - 1} V \frac{dp}{d\theta}, \quad (1)$$

where $dQ/d\theta$ is the net heat release rate (J/°CA), γ is the ratio of the specific heats, p is the cylinder pressure (Pa), and V is the cylinder volume (m³). In this study, a constant value of 1.35 was used for γ . After the end of the data acquisition, the engine was switched back to diesel and run for 30 minutes to flush out the fuel lines and the injection system from the pyrolysis oil.

2.3. Spray Test Experimental Setup. The spray characteristics tests were carried out on a constant volume, high pressure chamber. The chamber was equipped with two windows on two sides in order to have optical access for the spray visualization. Moreover, the background pressure of the chamber was controlled at 5 bar. The diagram in Figure 2 shows the experimental setup for the spray test rig.

The fuel injection system was composed of a fuel tank, a fuel pump that was able to adjust the injection pressure up to 500 bar, an injector, and an electronic control unit (ECU). The signal from the ECU triggers the injector and the high speed camera, achieving synchronization of the spray visualization. The injector used in the experiments was a single-hole solenoid injector. Two different nozzle holes' diameters of 0.12 mm and 0.18 mm were used in the

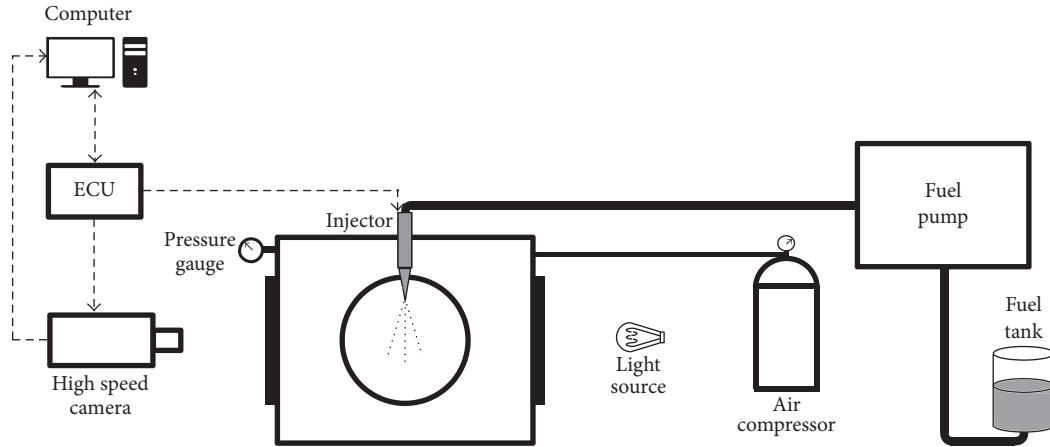


FIGURE 2: Schematic layout of the spray test rig.

experiments. Moreover, two different injection pressures of 300 bar and 450 bar were tested at every nozzle diameter size. The reason that the injection pressures were not tested at higher values is because the PPO is going to be used in diesel engines for stationary power and heat generation, which are usually equipped with mechanical injectors.

For the spray macroscopic characteristic investigation (spray tip penetration, spray cone angle, and spray area) a light source was used on one side and a high speed camera on the other. The high speed camera (Dantec Dynamics, Speedsense) was set up to record the spray images with an imaging speed of 60,000 frames per second and resolution of 256×256 pixels. In order to ensure the reliability of the results every experiment was repeated five times on each test condition. After that, the images were processed for further analysis of the spray characteristics. A program was written in MATLAB software, where a batch of spray images was able to get analysed at once and provide the spray tip penetration, spray cone angle, and spray area versus the time after the start of injection.

3. Results and Discussion

3.1. Advanced Injection Timing. In this section are presented and discussed the experimental results obtained from the engine by running on advanced IT (AIT) with a blend of 75% plastic pyrolysis oil and 25% diesel (PPO 75) at 75% and 100% engine loads which represent 9.47 bar and 12.63 bar of BMEP, respectively. The results of AIT (-23°CA bTDC) are compared with the standard IT (SIT) operation (-18°CA bTDC). The investigation is focused on the combustion characteristics, engine performance, and exhaust emission analysis. Moreover, the spray characteristics of PPO are analysed and compared with diesel.

Figure 3 shows the cylinder pressure with crank angle at 75% load. It can be seen that the AIT results in much higher in-cylinder pressure in comparison with SIT. This behaviour can be explained due to the earlier start of combustion on smaller cylinder volume. More specifically, the peak cylinder pressure for PPO 75 AIT at 75% load is advanced by 2.9°CA in

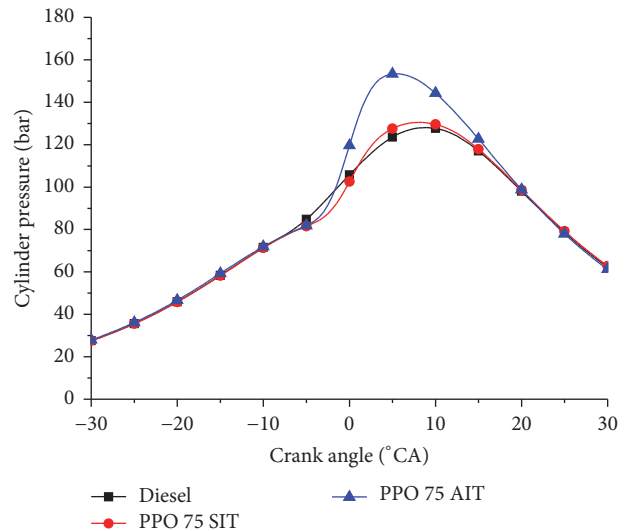


FIGURE 3: Variation of cylinder pressure with crank angle at 75% load.

comparison with the SIT operation. This result indicates that the ignition delay period of the PPO 75 AIT was even longer, resulting in better air-fuel mixing. The AIT is not sufficient to provide smaller ignition delay period due to the lower in-cylinder temperatures and pressures at the earlier $^\circ\text{CA}$ of the compression stroke.

The heat release rate (HRR) for the diesel and PPO 75 at SIT and AIT is presented in Figure 4. It can be seen from Figure 4 that the PPO 75 at AIT results in much higher HRR in comparison with SIT operation. The main reason for that is the longer ignition delay in the case of AIT. More specifically, the AIT of 5°CA degrees results in advance start of combustion of only 0.8°CA correlated to SIT. The longer ignition delay of AIT contributes to the better fuel atomisation and fuel-air mixing by allowing longer air-fuel mixing time which will reduce the local rich-fuel zones where the equivalence ratio (ϕ) is greater than 1. Furthermore,

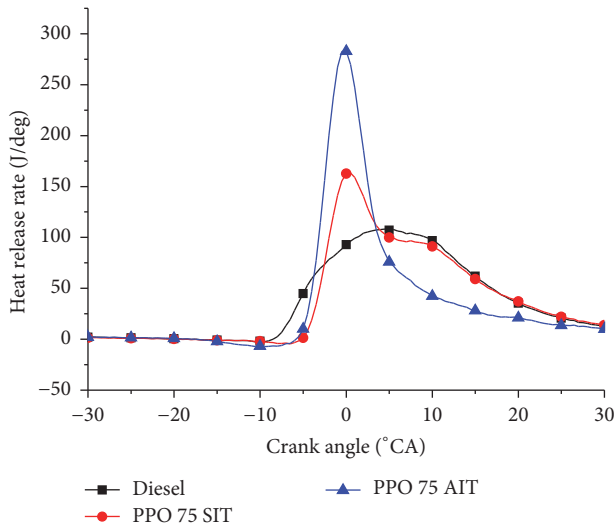


FIGURE 4: Variation of heat release rate with crank angle at 75% load.

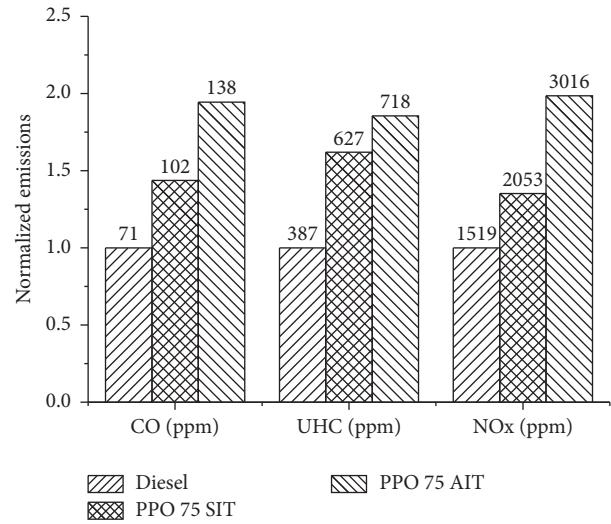


FIGURE 6: Normalized values of CO, UHC, and NOx emissions.

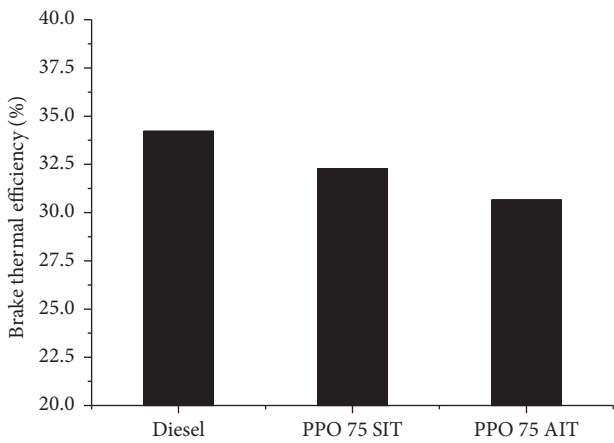


FIGURE 5: Brake thermal efficiency for diesel, PPO 75 SIT, and PPO 75 AIT.

fuels with high aromatic content as PPO tend to have higher adiabatic flame temperature because of the ring structure. The high adiabatic flame temperature results in higher heat release rate [14, 15]. Consequently, the higher portion of premixed combustion resulted in more violent combustion and higher HRR and in-cylinder peak pressure.

Figure 5 shows the brake thermal efficiency for diesel, PPO 75 SIT, and PPO 75 AIT at 75% load. It can be observed that the BTE is reducing from 32.3% on PPO 75 SIT operation to 30.7% on PPO 75 AIT. The main reason for the lower BTE is the longer ignition delay period which contributes to the increase of the fuel impingement on the cylinders walls. Consequently, the fuel that takes part in the effective combustion on the expansion stroke is less. Furthermore, the air-fuel mixing is enhanced by the longer ignition delay resulting in extremely high HRR early on the expansion stroke and less effective energy conversion of the heat to power on the cylinder. Finally, the lower BTE can

be explained due to the advanced start of combustion which results in increased heat transfer losses to the cylinders walls.

Figure 6 illustrates the normalized values of the carbon monoxide (CO), unburned hydrocarbons (UHC), and nitrogen oxides (NOx) emissions for the engine operation on diesel, PPO 75 SIT, and PPO 75 AIT. The Y-axis (normalized emissions) shows the variation of the values in comparison with the diesel operation which has been set as the baseline point of 1. Moreover, on the top of every column is written the actual value of the emissions.

It can be noticed from Figure 6 that the CO emissions increase considerably for the AIT operation (almost double in comparison to diesel with standard injection timing). CO emissions are mainly affected by the equivalence ratio and temperature, and it is a sign of incomplete combustion [15]. This result indicates that the combustion performance is more deficient and incomplete in the case of PPO 75 AIT. The longer ignition delay period results in the formation of local fuel-rich zones (crevices and cylinder walls) which are not able to oxidize to form CO₂. The main reasons for the UHC emissions on the exhaust are the flame quenching and the undermixing or overleaning zones [15–17]. According to Figure 6 the UHC emissions increase dramatically in the case of AIT. It is believed that the longer ignition delay enhances the formation of local rich-fuel zones on the cylinder walls which are not able to burn completely. The elevated fuel consumption of the PPO 75 AIT also contributes to the increased UHC emissions. Finally, the NOx emissions are greatly affected by the change of the injection timing. More specifically, the NOx emissions of the PPO 75 AIT are almost double in comparison with diesel and 953 ppm higher with PPO 75 SIT. In combustion theory, there are three NOx production mechanisms: the thermal NO formation, the prompt NO, and the NO formation from the nitrogen in the fuel [15, 18]. In diesel engines the mechanism that produces the higher amount of NOx is mainly the thermal mechanism due to the elevated temperatures and high oxygen availability. The effect of the thermal mechanism is even higher in the case

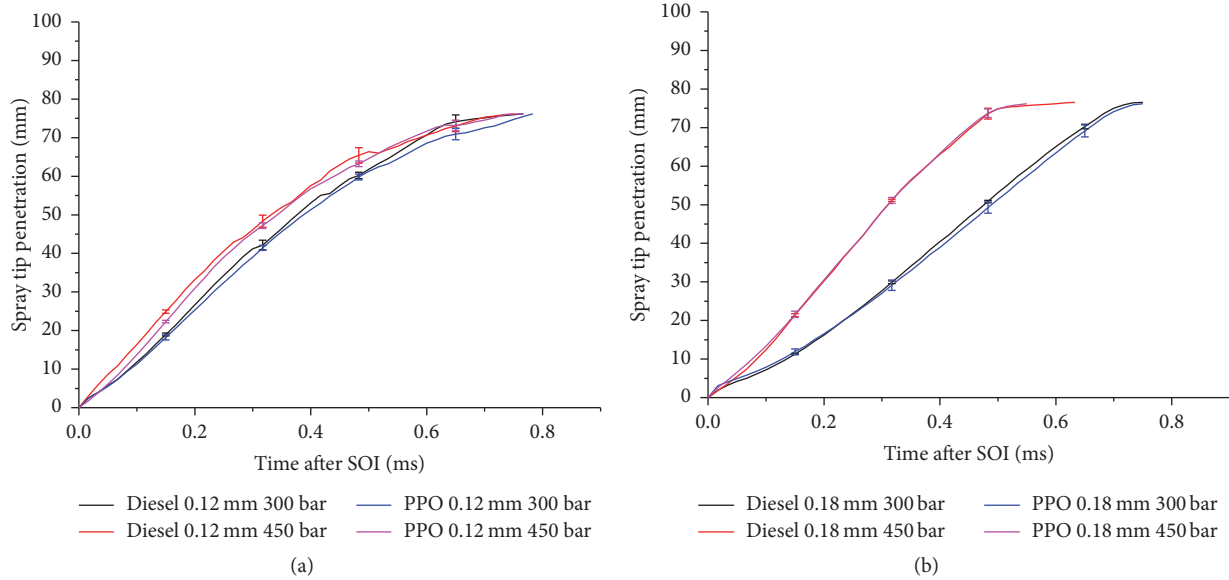


FIGURE 7: Variation of spray tip penetration with time for nozzle 0.12 mm (a) and 0.18 mm (b).

of the PPO 75 AIT due to the longer ignition delay. The longer ignition delay results in more homogeneous air-fuel mixture, higher in-cylinder pressures, in-cylinder temperatures, and heat release rates.

Figure 7 depicts the spray tip penetration for diesel and PPO for nozzle diameters of 0.12 mm and 0.18 mm and injection pressures of 300 bar and 450 bar (the bars show the standard error). The distance between the injector exit and the spray tip is defined as the spray tip penetration [19]. It can be seen that the impact of injection pressure is higher for the nozzle diameter of 0.18 mm in comparison with the 0.12 mm. As regards the differences between the diesel and PPO, it can be noticed that the spray tip penetration of PPO is faster for both 300 and 450 bar injection for the 0.12 mm nozzle diameter. On the other hand, the spray tip penetration is almost identical for the nozzle of 0.18 mm diameter. The results from the macroscopic spray characteristics analysis suggest that PPO has longer penetration, which means more chance to wet the wall which will lead to higher CO and UHC emissions. In addition to advanced injection, the in-cylinder pressure is lower at the time of injection, which will enhance the wall-wetting effect. It seems that the use of a larger hole at lower injection pressure would help; however it will increase particle emissions.

3.2. Fuel Additive. In this section are presented the experimental results obtained from the engine by running on PPO 75 blended with a commercial fuel additive at two different ratios of 1:80 and 1:40. The composition of the fuel additive is presented in Table 2. The blend results are compared with diesel and PPO 75 operation at 85% load which represents 10.74 bar of BMEP. The investigation is focused on the combustion characteristics, engine performance, and exhaust emission analysis.

Figure 8 illustrates the cylinder pressure with crank angle for diesel, PPO 75, and PPO 75 with two different ratios of

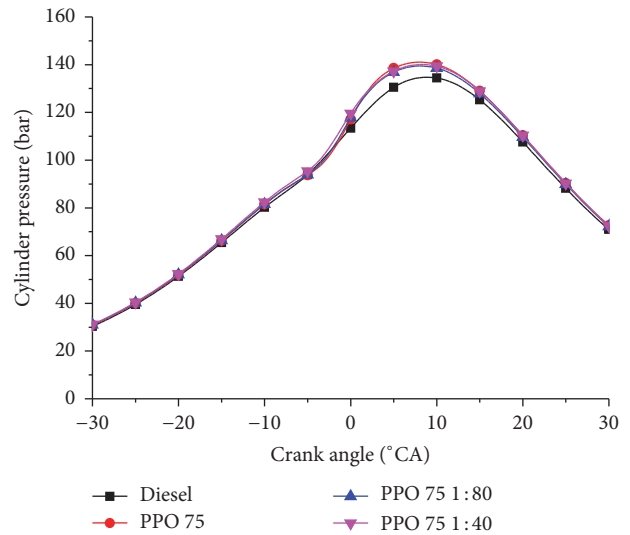


FIGURE 8: Variation of cylinder pressure with crank angle at 85% load.

fuel additive at 85% load. It can be observed that the cylinder pressure reaches higher values in the case of PPO operations in comparison with diesel. The main reason for that is the longer ignition delay of PPO 75 that results in later start of combustion during the compression stroke (closer to the TDC). Moreover, the longer ignition delay enhances the air-fuel mixing producing faster expansion of the combustion. The fuel additive addition marginally reduces the ignition delay period and the peak cylinder pressure. This happens due to the cetane improver that it is contained in the fuel additive.

The HRR for diesel and PPO 75 fuel additive blends at 85% load is presented in Figure 9. It can be clearly seen that

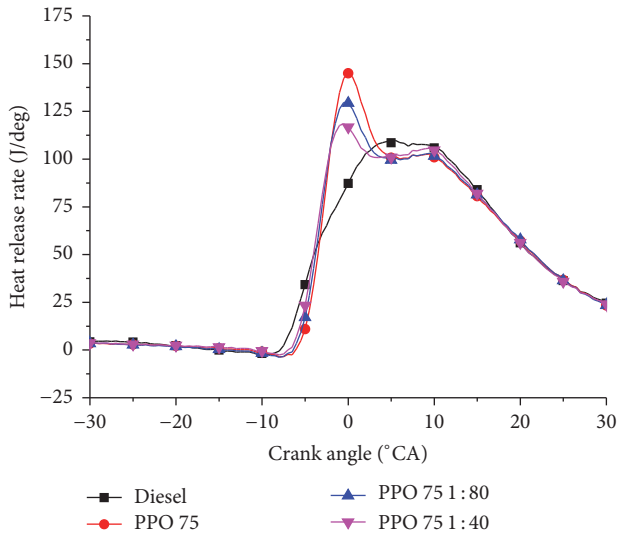


FIGURE 9: Variation of heat release rate with crank angle at 85% load.

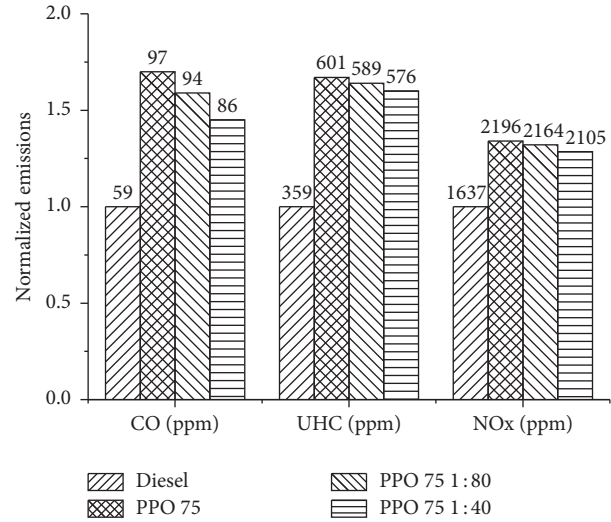


FIGURE 11: Normalized values of CO, UHC, and NOx emissions.

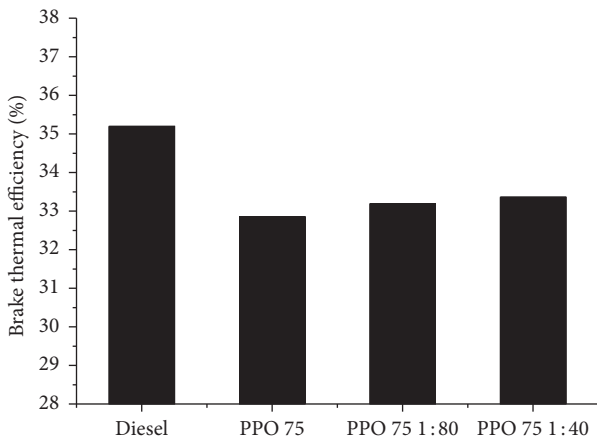


FIGURE 10: Variation of BTE at 85% load.

the higher the fuel additive addition the shorter the ignition delay period. At the same time, the peak HRR is reducing, resulting in a smoother, less violent combustion and more similar to diesel profile. However, it can still be observed the two-phase combustion for the PPO 75 fuel additive blends due to the longer ignition delay period which enhances the premixed combustion portion. It is worth mentioning at this point that the engine's noise was better as the ratio of the fuel additive was increasing. The knock effect is a very important factor for the engine's operational life. The reduction of the knock effect achieves the increase of the engine's operational life. In order to eliminate the knock effect the addition of a proper cetane number improver seems to be unavoidable in the case of PPO 75.

Figure 10 depicts the variation of BTE for diesel, PPO 75, PPO 75 1:80, and PPO 75 1:40 at 85% load. According to the figure, there is an improvement of the BTE by increasing the amount of the fuel additive. More specifically, the BTE increases from 32.8% to 33.2% with a blend ratio of 1:80

and to 33.5% with a ratio of 1:40 fuel additive. This result indicates that the earlier start of combustion improves the conversion of heat (released from the fuel) to kinetic energy on the pistons. There is still room for improvement which is possible to be covered by adding a dedicated cetane number fuel additive.

Figure 11 presents the normalized values of the carbon monoxide (CO), unburned hydrocarbons (UHC), and nitrogen oxides (NOx) emissions for the engine operation on diesel, PPO 75, PPO 75 1:80, and PPO 75 1:40. It can be observed from the experimental results that the CO emissions decrease with the addition of the fuel additive, but they still remain much higher in comparison with diesel. This result indicates that the fuel additive enhances the combustion performance and more carbon atoms are able to oxidize and form CO₂. Moreover, the shorter ignition delay period results in less impingement of the fuel on the cylinder walls and local fuel-rich zones. As regards the UHC emissions, it can be noticed from Figure 11 that there is a slight decrease with the addition of the fuel additive, but UHC emissions are still significantly higher than diesel operation. The shorter ignition delay period reduces the amount of fuel that impinges on the cylinder walls; therefore, less rich-fuel regions are developed. Finally, according to the experimental results presented in Figure 11, NOx emissions do not seem to get affected significantly by the addition of the fuel additive. Maybe this is a result of two different processes which result in the same total amount of NOx emission. The addition of the fuel additive reduces the ignition delay period resulting in less homogeneous air-fuel mixing (lower in-cylinder temperatures and lower NOx). At the same time the fuel additive improves the combustion even in rich-fuel zones resulting in elevated in-cylinder temperatures and NOx emissions. Consequently, the total amount of NOx emissions remains the same.

4. Conclusions

An experimental investigation was carried out to analyse and understand the combustion, performance, and emission characteristics of a diesel engine running on advanced injection timing and on standard injection timing with the addition of a fuel additive on oil which derives from the pyrolysis of waste plastics. The following conclusions can be drawn from the test results:

- (i) The engine was able to operate at AIT on PPO 75 at 75% load but with longer ignition delay, higher cylinder peak pressure, and higher heat release rate in comparison with the PPO 75 SIT operation.
- (ii) The addition of the fuel additive reduces the ignition delay period, cylinder peak pressure, and peak heat release rate. As a result, the brake thermal efficiency, CO, UHC, and NOx emissions are all improved.
- (iii) The engine's thermal efficiency decreases with the AIT and all measured emissions, including CO, UHC, and NOx, increase with AIT. The spray test revealed that the PPO spray has a longer tip penetration, which explained why AIT is not a preferable solution.

The testing results suggest that for both long-term and short-term operation, the AIT is not preferable as the engine performance declines. As regards to the fuel additive engine testing, the results suggest that the use of a dedicated cetane number fuel additive would achieve even better combustion performance (similar to diesel).

Nomenclature

PPO 75:	75% plastic pyrolysis oil + 25% diesel fuel
SIT:	Standard injection timing
AIT:	Advanced injection timing
bTDC:	Before top dead centre
NOx:	Nitrogen oxides
PM:	Particulate matter
CO:	Carbon monoxide
CO ₂ :	Carbon dioxide
UHC:	Unburned hydrocarbon
LHV:	Lower heating value
BMEP:	Brake mean effective pressure
HRR:	Heat release rate
φ :	Equivalence ratio
BTE:	Brake thermal efficiency.

Competing Interests

The authors declare that there is no conflict of interests regarding the publication of this paper.

Acknowledgments

The authors sincerely thank Thermitech Solutions Ltd and UK Engineering and Physical Sciences Research Council (EP/K036548/2) for the support to conduct this research.

References

- [1] M. Mani, C. Subash, and G. Nagarajan, "Performance, emission and combustion characteristics of a DI diesel engine using waste plastic oil," *Applied Thermal Engineering*, vol. 29, no. 13, pp. 2738–2744, 2009.
- [2] C. Wongkhorsub and N. Chindaprasert, "A comparison of the use of pyrolysis oils in diesel engine," *Energy and Power Engineering*, vol. 5, pp. 350–355, 2013.
- [3] M. Mani, G. Nagarajan, and S. Sampath, "An experimental investigation on a di diesel engine using waste plastic oil with exhaust gas recirculation," *Fuel*, vol. 89, no. 8, pp. 1826–1832, 2010.
- [4] R. Guntur, D. Kumar, and V. K. Reddy, "Experimental evaluation of a diesel engine with blends of diesel-plastic pyrolysis oil," *International Journal of Engineering Science and Technology*, vol. 6, pp. 5033–5040, 2011.
- [5] M. Mani, G. Nagarajan, and S. Sampath, "Characterisation and effect of using waste plastic oil and diesel fuel blends in compression ignition engine," *Energy*, vol. 36, no. 1, pp. 212–219, 2011.
- [6] J. Pratoomyod and K. Laohalidanond, "Performance and emission evaluation of blends of diesel fuel with waste plastic oil in a diesel engine," *International Journal of Engineering Science and Technology*, vol. 2, pp. 57–63, 2013.
- [7] C. Güngör, H. Serin, M. Özcan, S. Serin, and K. Aydın, "Engine performance and emission characteristics of plastic oil produced from waste polyethylene and its blends with diesel fuel," *International Journal of Green Energy*, vol. 12, no. 1, pp. 98–105, 2015.
- [8] V. K. Kaimal and P. Vijayabalan, "A detailed study of combustion characteristics of a DI diesel engine using waste plastic oil and its blends," *Energy Conversion and Management*, vol. 105, pp. 951–956, 2015.
- [9] M. Mani and G. Nagarajan, "Influence of injection timing on performance, emission and combustion characteristics of a DI diesel engine running on waste plastic oil," *Energy*, vol. 34, no. 10, pp. 1617–1623, 2009.
- [10] A. Sharma and S. Murugan, "Combustion, performance and emission characteristics of a di diesel engine fuelled with non-petroleum fuel: a study on the role of fuel injection timing," *Journal of the Energy Institute*, vol. 88, no. 4, pp. 364–375, 2015.
- [11] A. K. Wamankar and S. Murugan, "Effect of injection timing on a di diesel engine fuelled with a synthetic fuel blend," *Journal of the Energy Institute*, vol. 88, no. 4, pp. 406–413, 2015.
- [12] J. Devaraj, Y. Robinson, and P. Ganapathi, "Experimental investigation of performance, emission and combustion characteristics of waste plastic pyrolysis oil blended with diethyl ether used as fuel for diesel engine," *Energy*, vol. 85, pp. 304–309, 2015.
- [13] S. Hariharan, S. Murugan, and G. Nagarajan, "Effect of diethyl ether on Tyre pyrolysis oil fueled diesel engine," *Fuel*, vol. 104, pp. 109–115, 2013.
- [14] I. Kalargaris, G. Tian, and S. Gu, "Combustion, performance and emission analysis of a DI diesel engine using plastic pyrolysis oil," *Fuel Processing Technology*, vol. 157, pp. 108–115, 2017.
- [15] J. B. Heywood, *Internal Combustion Engine Fundamentals*, McGraw Hill, New York, NY, USA, 1988.
- [16] G. Greeves, I. M. Khan, C. H. T. Wang, and I. Fenne, "Origins of hydrocarbons emissions from diesel engines," SAE Technical Paper 770259, 1977.
- [17] S. Mendez, J. T. Kashdan, B. Thirouard, G. Bruneaux, and F. Vangraefschepe, "Formation of unburned hydrocarbons in low

temperature diesel combustion,” SAE Technical Paper 2009-01-2729, 2009.

- [18] H. Semerjian and A. Vranos, “NO_x formation in premixed turbulent flames,” *Symposium (International) on Combustion*, vol. 16, no. 1, pp. 169–179, 1977.
- [19] J. Mo, C. Tang, J. Li, L. Guan, and Z. Huang, “Experimental investigation on the effect of n-butanol blending on spray characteristics of soybean biodiesel in a common-rail fuel injection system,” *Fuel*, vol. 182, pp. 391–401, 2016.

Research Article

Experimental Study on the Influence of DPF Micropore Structure and Particle Property on Its Filtration Process

Zhongwei Meng,^{1,2} Jia Fang,^{1,2} Yunfei Pu,³ Yan Yan,^{1,2} Yi Wu,¹
Yongzhong Wang,¹ and Qiang Song⁴

¹Vehicle Measurement, Control and Safety Key Laboratory of Sichuan Province, Sichuan Collaborative Innovation Center for Automotive Key Components, School of Automobile and Transportation Engineering, Xihua University, Chengdu 610039, China

²Key Laboratory of Fluid and Power Machinery (Xihua University), Ministry of Education, Chengdu 610039, China

³Department of Automotive Engineering, Chengdu Aeronautic Polytechnic, Chengdu 610100, China

⁴Key Laboratory for Thermal Science and Power Engineering of Ministry of Education, Department of Thermal Engineering, Tsinghua University, Beijing 100084, China

Correspondence should be addressed to Zhongwei Meng; mengzw@mail.xhu.edu.cn and Jia Fang; jiafang@mail.xhu.edu.cn

Received 19 September 2016; Accepted 22 November 2016

Academic Editor: Guohong Tian

Copyright © 2016 Zhongwei Meng et al. This is an open access article distributed under the Creative Commons Attribution License, which permits unrestricted use, distribution, and reproduction in any medium, provided the original work is properly cited.

A single layer filtration system was developed to investigate the filtration and regeneration performance of diesel particle filter (DPF). The particle layer thickness was directly measured online to analyze the different filtration stages. The influence of particle property on particle layer stage performance was also investigated. The results indicate that the filtration velocity can greatly affect the deep bed filtration stage, and the deposited particle layer can be compressed even in very low filtration velocity and higher filtration velocity trends to form denser particle layer. Optimizing the pore structure can effectively shorten the deep bed filtration stage and reduce the pressure drop eventually. An empirical function was proposed to relate the pore structure and the initial increment rate of pressure drop, which presented that reducing the pore size distribution range (3σ) can result in low DPF filtration pressure drop. The filtration stage could be further divided into four stages, and the value of particle layer thickness ranging within 15~20 μm has been found to be critical number for the shift from the transient stage to the cake filtration stage. Particle with large primary diameter and BET surface was beneficial to form loose particle layer.

1. Introduction

Diesel engines are widely employed for their efficient fuel consumption and low CO₂ emission, but they are also one of the widely recognized sources for particle emission, which has negative impacts on the environment and human health. Increasingly stringent legislations on vehicular emissions have triggered research interests in fuel formulations and oxygenated fuel addition [1–5], engine calibration and designs [6–9], and effective after treatment technologies [10, 11] to reduce particle and gaseous emissions. Among all the aforementioned techniques, engine calibration has limited room for emissions improvement, and the effects of oxygenated fuel addition on particle emissions are somewhat controversial [2]. Therefore, diesel particle filter (DPF) has been considered as an effective means to reduce particle

emissions from diesel engines since it directly captures diesel particles to prevent their release to the atmosphere [11]. Although a DPF potentially has impressive filtration efficiencies, generally in excess of 95% and up to about 99% in mass, it requires low operating pressure drop to avoid the deterioration of the engine output power and fuel efficiency. Such a low pressure drop can reduce the DPF regeneration frequency and the fuel regeneration. Thus it is necessary to investigate the filtration mechanism and methods to minimize the pressure drop.

Typically, a three-stage filtration process, including deep bed filtration stage, transition filtration stage, and particle layer (“cake”) filtration stage, was used to illustrate the particle deposition process in porous ceramic pores. The microscopic observations have been firstly conducted to show the

particle deposition process, by cutting the DPF substrate and then exposing the loaded DPF channels to obtain the surface topography above the ceramic surface. While the information of particle packing property was missed [12], the uneven particle distribution along the DPF channel was observed with the thickness being less than $100\ \mu\text{m}$, which was directly due to uneven wall flow velocity along the channel length [13]. The inhomogeneous porous particle cake was also investigated with the thickness ranged in 130 to $500\ \mu\text{m}$, and the particle cake consisted of several superposed layers corresponding to different soot generations [14]. However these offline measurements cannot quantify the particle loading and distinguish the transition of the different filtration stages. Therefore, the single DPF filtration channel system was developed to online measure the particle deposition process without cutting the DPF substrate. Based on the single channel system, evolution of the filtration process was presented by the microscopic pictures [15], and the deposited particulate volumes required to reach the transition points from deep bed to “cake” filtration were determined [16], and the packing density of particle layer can be calculated [17]. The deposited particle cake tends to present the similar packing property once the deep bed and transient stage were completed. So the deposition process in deep bed filtration stage and packing property of cake filtration stage are the two hot research points to investigate the filtration process to minimize the filtration pressure.

In the year 2007, a dense layer coated on common DPF ceramic wall was experimentally reported to control the deep bed filtration and reduce the overall filtration pressure drop [18]. This improved technology was referred to as the dual layer pore structure, in which the gas inflow side of the wall is given a filtration layer having small pores and a high porosity. It has been demonstrated to drastically improve the filtration efficiency, drastically reduce the backpressure with particle accumulation, and provide a linear relationship between soot loading and backpressure [19]. The ash loaded DPFs were found to show similar features of reducing the pressure drop [20, 21]. A numerical simulation model was applied to study the influence of pore diameter of dense layer on the particle slip and the accumulated particle inside the wall, which could obviously affect the filtration efficiency, pressure drop, and the catalytic oxidation of deposited particle in regeneration process [22]. The dual layer technology is a good way to avoid the accumulated particle inside the micropores. However, the influence of micropore structure on deep bed filtration stage has not yet been reported, which is the first motivation of our study presented in this paper.

As mentioned above, the particle packing property in cake filtration stage as another research point needs to be focused on. It is related to not only the pressure drop but also the regeneration process. While simple approaches were used to describe the soot layer, mostly assuming a constant value for soot layer density and permeability in previous research work. The values of $100\ \text{kg/m}^3$ and $140\ \text{kg/m}^3$ were mostly employed as packing density in mathematical models for the simulation of the loading and regeneration process in the DPF [23–26]. In order to validate the simulation model with

the experimental results, the density values were usually selected optionally and baselessly. For example, the range of 65 to $99\ \text{kg/m}^3$ was applied in [27], and the values of 117 to $136\ \text{kg/m}^3$ were used in [28]. Thus the experimental measure of the particle layer density independently to the permeability is greatly needed. The values of 25 – $100\ \text{kg/m}^3$ were experimentally obtained by measuring the thickness and mass of particle layer deposited on single channel piece [17]. For the reason of the big experimental workload (e.g., pieces cutting and images solving), only several filtration velocities and particle loading were involved in this investigation. Furthermore, the method of cutting the single channel piece could lead to possibly damaging the deposited particle layer and obtaining large deviation on particle layer mass weighting. Therefore, the damage-free measuring of the particle layer thickness is urgently needed. The thickness can be directly measured online by the laser displacement sensor to simplify the experimental measurement, and this improvement can give a convenient for investigating the influence mechanism of the particle layer property, which is the second motivation of this study.

In the present study, a single layer channel system is developed, which can be employed to investigate both the particle filtration and regeneration process. Firstly, the filtration pressure drop of ceramic pieces under different velocity and pore structures were measured, and the deep bed filtration stage was focused on to investigate the relationship between the initial pressure drop increasing rate and the micropore structure. The dimensional analysis and experimental fitting methods were employed. Secondly, the filtration stage was analyzed based on the surface scanning electron microscope (SEM) measurement and the relationship between the thickness and pressure drop. Finally, the particle with different parameters is used to obtain the different particle cake packing densities to seek the effect of particle property on particle layer filtration process.

2. Experimental Setup and Materials

2.1. Single Layer Channel Filtration System. In order to visualize the observations of filtration process of DPF, a single layer channel filtration system is built under laboratory conditions; and the sketch map of this system is shown in Figure 1. As to the particle sources, the diesel engines exhaust soot, carbon black particle, and fuel (e.g., Propane) combustion generated soot are considered and flow into the single layer channel part separately through bypass valve control. When the diesel engine or the fuel burner are acted as soot generator, the inlet pipe and single layer channel part are heated and thermal insulated at the constant temperature 200°C . It is aimed at avoiding the water and volatile organic compounds (VOC) of the exhausted gas condensed in the single layer channel part. The condensed water and VOC can destroy the deposited particle layer resulting in a failure to obtain the expected experimental data correctly. Besides the heating, the thermal insulation can reduce the particle thermophoresis deposition in the sample pipe, so the particle concentration can be preserved uniformly, except for the fluctuation of the operating

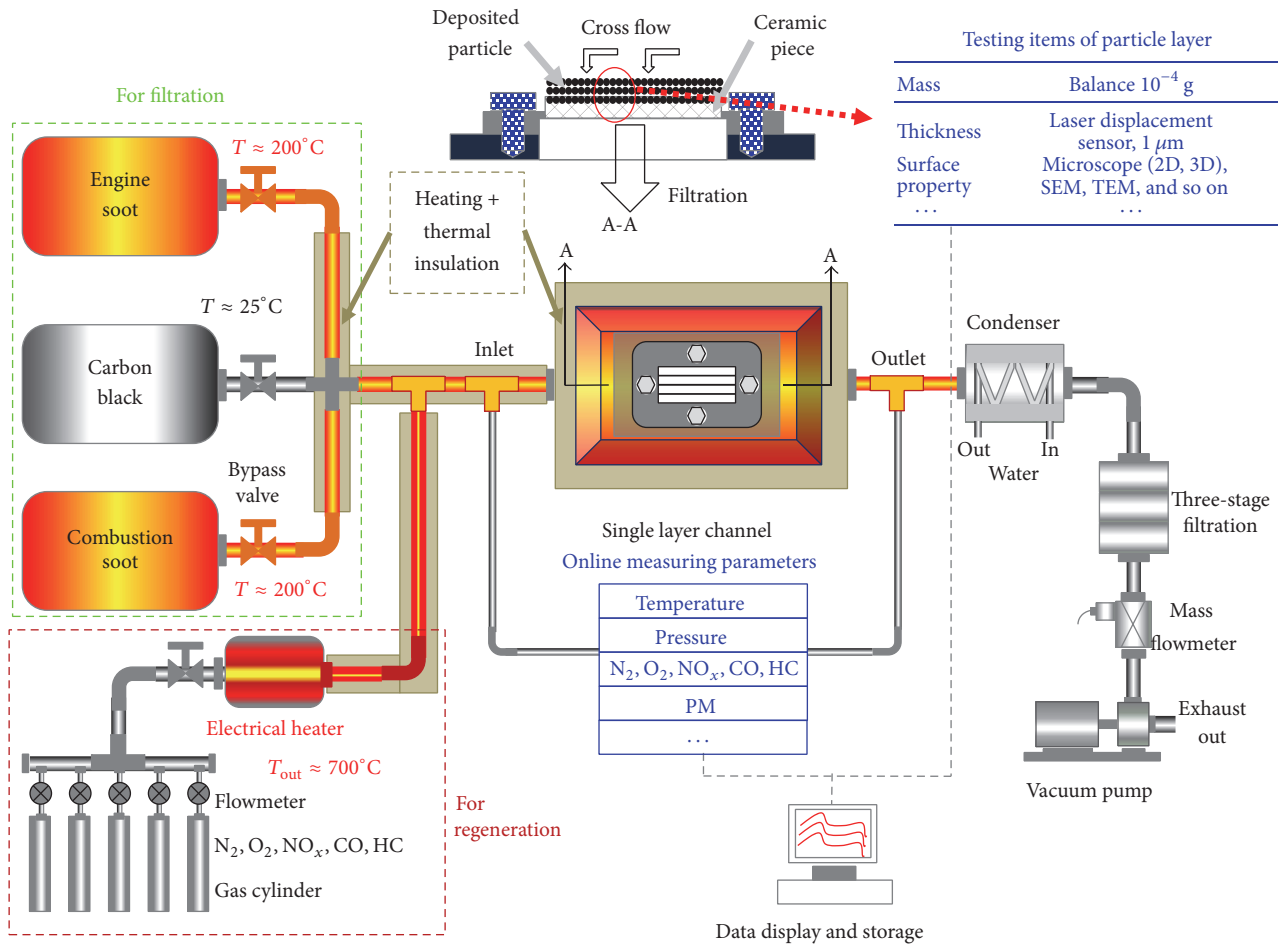


FIGURE 1: The schematic diagram of single layer channel filtration system.

condition of the particle source. When applying the carbon black particle as the substituted or artificial diesel engine soot, the filtration process is conducted at the room temperature of about 25°C. The dried commercial carbon black is prepared before the experiment and then homogeneously dispersed by an aerosol generator (*Palas RBG1000*) to simulate the diesel engine exhaust soot.

As to the single layer channel part, a single layer of ceramic piece ($30 \times 60 \text{ mm}^2$) cutting from a whole wall flow ceramic DPF filter is mounted in the middle of this part, which is attached to the stainless steel (SS) plate using high temperature cement (*OMEGABOND® OB-400*) and fastened the SS plate by 4 bolts with M8 mm. The real pictures of the ceramic piece and its attached SS plate before and after the soot deposition are shown in Figure 2. The deposited particle mass can be measured by weighting the ceramic piece together with the SS plate before and after the particle deposition using an electronic balance with the accuracy of 10^{-4} g. The surface topography of particle layer on ceramic piece can also be measured offline by microscope or SEM/TEM (transmission electron microscope) method, which can directly show the microscopic and detail variation information of the particle deposition process. The particle deposition process on the ceramic

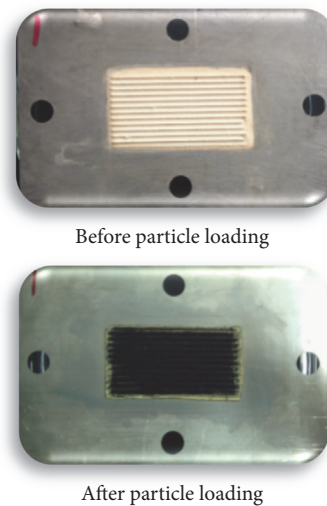


FIGURE 2: The ceramic pieces.

piece surface can also be directly observed through the visualization window (Quartz glass) in the upright cover just above the ceramic piece. The picture of the visualization window

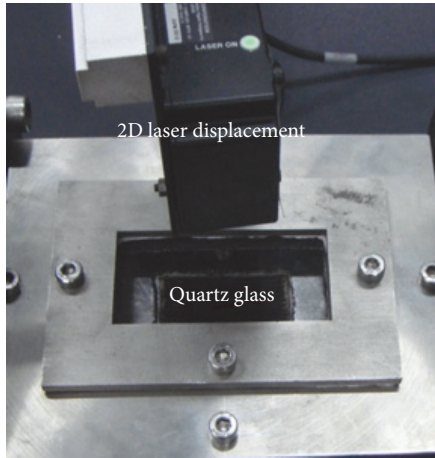


FIGURE 3: The visualization window.

is shown in Figure 3. A 2D laser displacement sensor (*LJ-G080, Keyence*) is applied to online measure the thickness of particle layer through the visualization window. The *LJ-G080* sensor has 650 testing points with the accuracy of $1\ \mu\text{m}$, which is capable of measuring the evolution of particle layer deposition during the filtration process.

Besides, the other online measuring parameters at the inlet and outlet of the single layer channel are temperature, pressure drop, exhaust gas concentration, and particulate matter (PM) mass and number distribution. The temperature is measured by K-type thermocouples, and pressure drop is measured by U-type manometer or high accuracy pressure transducers (*OMEGA's PX409-005CG5V*) with the measure ranges less than $\pm 35\ \text{kPa}$. The gas concentrations are measured by *AVL DICOM4000* or *MRU NOVA PLUS* gas analyzer. The PM mass and number distributions are measured by the *CAMBUSTION DMS500* fast particle analyzer.

As to the single layer channel configuration, the channel height is selected for 15 mm, which is larger than the 1.16 mm for 300 CPSI DPF or 2.16 mm for 100 CPSI DPF. The reason of this design is to facilitate the mechanical machining of the SS frame and convenient for installing and removing the single layer ceramic piece. The researched particle diameter is normally smaller than 300 nm, so the particle in aerosol has good tracking capability with the cross flow. Although the cross flow pattern of single layer channel is different from that of honeycomb channel of DPF filter, the particle deposition processes on the ceramic surface of these two flow patterns have good consistency with each other. In this system, the particle deposition process normal to the ceramic surface is just focused on, while the particle migration potentially driven by the main flow direction parallel to ceramic surface is ignored.

As to the single layer channel operating pressure, because the particle sources are connected to the single layer channel through the bypass pipes, and the redundant exhaust is directly discharged into the atmosphere, so the inlet pressure of the single layer channel is nearly the atmospheric pressure. Actually the particle is absorbed into the single layer channel for filtration driven by a vacuum pump. The operating pressure of the single layer channel system is actually different

from the real DPF system. The range of about 90–100 kPa is normally for the former one, while the range of about 100–115 kPa is normally for the later one. The variation of the operating pressure can cause the variation of operating temperature and particle concentration, while this deviation can be estimated and limited into a certain degree. The filtration velocity (flow rate) is controlled by a thermal wire type mass flowmeter, shown in Figure 1. The vertical filtration velocity in this system is set to 0.02–0.15 m/s, which is in accordance with the wall flow filtration velocity of the real honeycomb DPF filter. Before the exhaust from the single layer channel flow into the mass flowmeter, the exhaust is cooled by a condenser, and then the condensed water and VOC fraction and the penetrated particle from the single layer channel are absorbed and filtered by a three-stage filtration system, to protect the mass flowmeter and ensure the measure accuracy.

On the other side, after the ceramic piece is loaded with particle through the filtration process, the combustion of the loaded particle layer can also be visually observed by this single layer system. The regeneration of deposited particle layer can be conducted by elevating the inlet exhaust temperature larger than 550°C to oxidize it, using an electrical heater (*MHI MTA925-02*) with maximum outlet temperature being about 700°C . The gas concentration and mass flowrate for the regeneration are controlled by the gas cylinder group and their flowmeters for each of them. Because the reason of this paper is not focused on the regeneration process, the detailed information of the regeneration function of this single layer channel system is just illustrated simply so far.

2.2. Particle Sources. In this study, a one-cylinder diesel generator CF5000LN (0.406 L, wind cooled, 9 kW/3600 RPM) and a four-cylinder diesel engine DK4A (2.5 L, common rail, turbo charged, 75 kW/3600 RPM) are used to produce diesel soot as the soot generator. The CF5000LN generator is operated at 70% engine full load with the exhaust temperature about 350°C , while the DK4A engine is operated at the load of 57 Nm/2250 RPM with the exhaust temperature about 290°C .

Besides, four-type Degussa carbon blacks (Printex-U, SB 4A, CB FW200, SB250) are also used as substituted soot to investigate the particle deposition process. The particle properties of these carbon blacks together with the DK4A engine soot are shown in Table 1, and the microscopic TEM (TECNAI G2 F20) picture of these particles is also shown in Figure 4. The primary diameter data of different particles are their statistical mean values among more than 20 particles selected from the TEM pictures using image processing software. The values of Brunauer-Emmett-Teller (BET) surface, VOC, and ash contents of carbon black are provided by manufacturers. The VOC content of DK4A soot is measured by vacuum dry method, while the BET surface and ash content of DK4A soot are not presented in this paper. The DK4A soot is collected directly from the engine rail pipe using the multi-layer stainless steel mesh filter and the sample mass obtained about 40 mg per hour under a steady state engine condition.

The Special Black (SB) 250 particles have the largest primary diameter of 51 nm, while the lowest BET surface ($40\ \text{m}^2/\text{g}$) is shown. The Carbon Black (CB) FW 200 particles

TABLE 1: The parameters of different particles.

Particles	Primary diameter (nm)	BET (m^2/g)	VOC (%)	Ash (%)
DK4A soot	24	NA	4.1	NA
Printex-U	34	92	5.0	0.02
SB 4A	44	180	14.5	0.02
CB FW200	20	550	20.0	0.02
SB 250	51	40	3.5	0.4

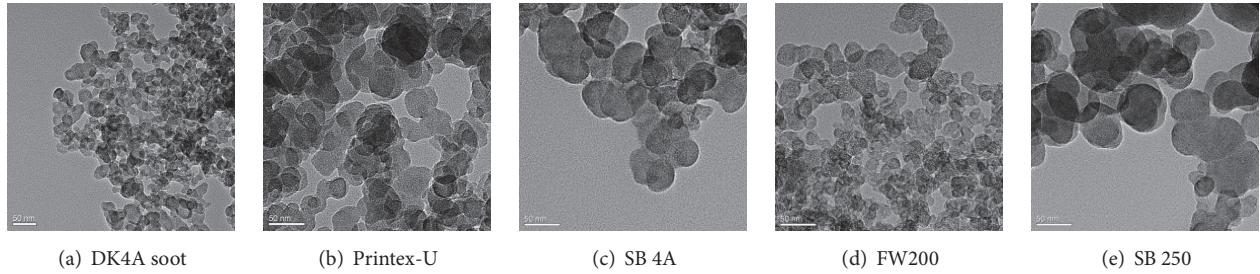


FIGURE 4: The TEM pictures of different particles.

have the smallest primary diameter of 20 nm, while the highest BET surface ($550 \text{ m}^2/\text{g}$) is shown. The VOC content of the DK4A soot is about only 4.1%, and although the VOC contents of SB 4A and CB FW200 particles are relatively large as 14.5% and 20.0% separately, the carbon black particles are operated in room temperature of about 25°C ; thus the influence of VOC on particle filtration process is ignored in this paper. Besides, the ash contents of carbon black particles are smaller than 0.4% at the most, which is believed to be larger than the ash content of DK4A soot; thus the influence of ash content on particle filtration process is also ignored in this study.

2.3. Micropore Structure of Experimental Ceramic Pieces. There are seven types of ceramic pieces used in this study, which are randomly cut from filters from different four DPF suppliers (one is American company, and the other three ones are domestic manufacturers). The micropore structures of these ceramic pieces are shown in Table 2, which are measured by a mercury porosimeter (*Micromeritics, AutoPore IV 9510*). The porosities of the tested pieces ranged from 13.88% to 51.34%, while the average pore diameters ranged from $5.59 \mu\text{m}$ to $12.16 \mu\text{m}$.

Table 2 also shows the value of three standard deviations (3σ), which is obtained from the Gaussian fitting the pore size distribution curves of different tested ceramic pieces. The Gaussian fitting curves of three ceramic pieces, for example, are shown in Figure 5, and the values of the 3σ ranged from $2.91 \mu\text{m}$ to $12.43 \mu\text{m}$, which are capable of representing the micropore size distribution of ceramic pieces.

The #1 ceramic pieces were prepared to study the influence of filtration velocity ($0.02\text{--}0.04 \text{ m/s}$) on the filtration process, while the #2 to #4 pieces were used for 0.02 m/s filtration velocity condition, and the #5 to #7 pieces were used for 0.04 m/s condition to study the influence of pore structure on the filtration process in Section 3.1 in this paper. Besides,

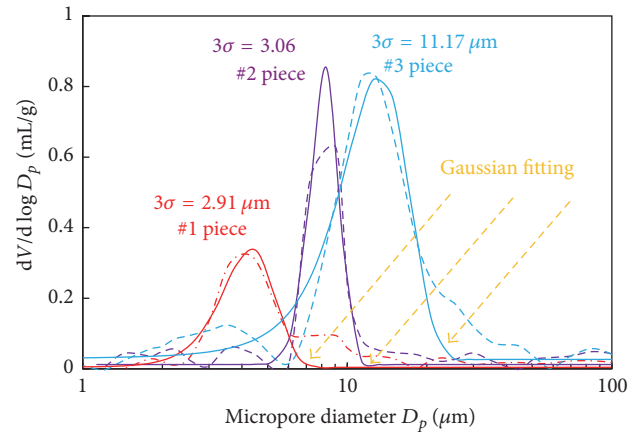


FIGURE 5: Gaussian fitting of tested ceramic pieces.

the #1 ceramic pieces are also used to conduct the research work of Sections 3.3 to 3.5.

3. Experimental Results and Discussion

3.1. Filter Pressure Drop. The pressure drop of #1 ceramic pieces is measured for testing with different filtration velocities, and the diesel generator CF5000LN is used as particle source, and the operating temperature is kept at 200°C for steady state filtration test. With the increase in particle loading time, the pressure drop increases along with the deposited particle to present the typical three-stage filtration process, which is shown in Figure 6. With the increase in filtration velocity, the deposited particle into the micropores of ceramic piece in unit time is increased, which led to rapidly completing the deep bed and transient filtration stage under high filtration velocity condition. The initial increment rates are obtained by fitting the first 120 s data of pressure drop

TABLE 2: Filter pore structures.

Ceramic pieces	Porosity $\varepsilon_w/\%$	Average pore diameter $D_p/\mu\text{m}$	Three standard deviations (3σ)/ μm
#1	15.70	5.59	2.91
#2	26.57	7.08	3.06
#3	51.34	12.16	11.17
#4	19.82	6.00	8.80
#5	47.06	11.02	12.43
#6	13.88	6.40	2.88
#7	18.29	6.48	3.18

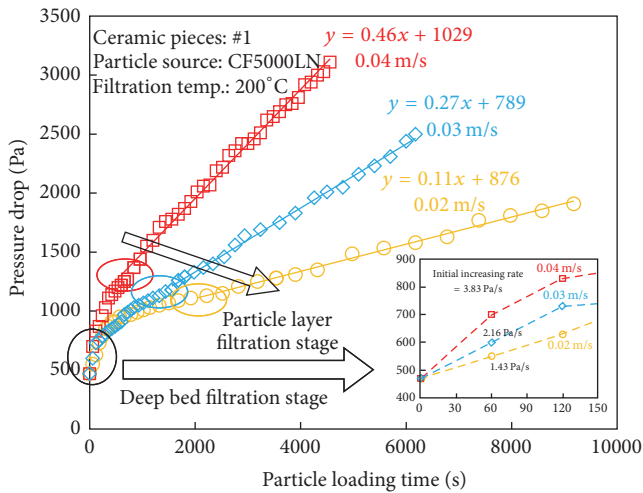


FIGURE 6: Pressure drop for different filtration velocities (in order to conveniently compare the increment rates of the pressure drop for different filtration velocities, the initial pressure drops are set to the same value of 470 Pa which is measured for the 0.02 m/s filtration velocity).

curve, with the values being 1.43 Pa/s for 0.02 m/s filtration velocity, 2.16 Pa/s for 0.03 m/s, and 3.83 Pa/s for 0.04 m/s, respectively. It is attributed to the increasing deposited particle mass in unit time and filtration velocity, which is defined by Darcy's formula. The micropores are gradually blocked by deposited particle causing the ceramic piece permeability to gradually decrease. For the reason of the micropores being not blocked homogenously with loading time, the increment rate of pressure drop curve gradually decreased with loading time; thus the initial increment rates of first 120 s are used to evaluate the deep bed filtration process. The particle tends to more easily penetrate the ceramic piece in higher filtration velocity, so the deposited particle mass dividing the filtration velocity in higher filtration velocity condition is smaller than that of lower filtration velocity. Therefore, the initial increment rate does not increase quadratically with filtration velocity. For example, comparing with the two operating conditions of the 0.02 and 0.04 m/s, the value of $3.83/1.43 = 2.68$ is clearly smaller than the value $(0.04/0.02)^2 = 4$ and the relative deviation is about 33%.

The starting times of particle layer filtration also obviously decrease with the increase in filtration velocity, shown in Figure 6. The particle layer filtration stages appear after about 1900 s for 0.02 m/s filtration velocity, 1300 s for 0.03 m/s, and 600 s for 0.04 m/s, which are approximately evaluated from the pressure drop curves. The pressure drop increment rates during the particle layer filtration stage are fit and shown with straight line with the increment rate values being 0.11 Pa/s for 0.02 m/s, 0.27 Pa/s for 0.03 m/s, and 0.46 Pa/s for 0.04 m/s filtration velocity, respectively. After the particle layer is formed, the particle filtration efficiency is kept constantly up to about 99% generally. So the value of deposited particle mass in unit time divided by the filtration velocity in particle layer filtration stage is kept nearly constantly for different filtration velocity. Based on this reason, the increment rate of pressure drop increases approximately quadratically with the increase in filtration velocity. For example, comparing with the two operating conditions of the 0.02 and 0.04 m/s, the value of $0.46/0.11 = 4.18$ is near the value of $(0.04/0.02)^2 = 4$; the relative deviation is only about 4.5%, which is obviously smaller than 33% in deep bed filtration stage. However, the particle layer would tend to become denser in high filtration velocity, which should be taken into account under the condition of higher filtration velocity.

Although the different filtration velocity has significant effect on the deep bed filtration, once the particle layer is formed, the particle layer filtration process would present similar changing trends under different filtration velocities. This result suggests that decreasing the pressure drop of deep bed and transient filtration stage may be the only way to decrease the DPF pressure drop under the steady state filtration condition. This is also the original cause of dual layer filtration technology illustrated in the Introduction part of this paper. Therefore, different pore structure ceramic pieces are used to investigate the influence of micropore structure on filtration process, which is targeted to find the relationship between the pore structure and deep bed filtration process and ultimately obtain the optimization region or method to decrease the DPF pressure drop.

The measured pressure drop curves for different pore structure pieces with the 0.02 m/s and 0.04 m/s filtration velocities are shown in Figure 7. The slopes of the pressure drop curves during the particle layer filtration stage have little difference for the different pore structures for the same

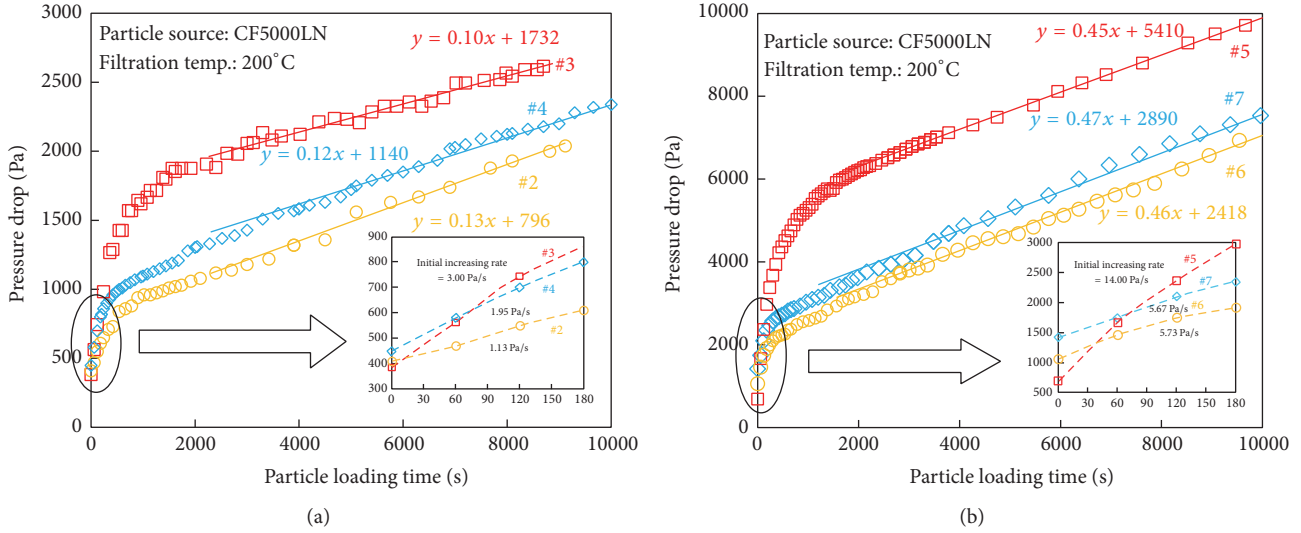


FIGURE 7: Pressure drop of different pore structure pieces: (a) filtration velocity = 0.02 m/s and (b) 0.04 m/s.

filtration velocity. The relative deviations are about 16% and 4% for two filtration velocities. The reason is that the flow through the deposited particle layer mainly depends on the soot properties and the filtration velocities, and the particle layer characteristics are no longer subjected to the structure of the ceramic micropores below it.

The pore structure has obvious effects on the pressure drop during the deep bed filtration and transition filtration stages. The filter with higher initial pressure drop increment rate and longer transition filtration stage has higher pressure drops during particle layer filtration stages. Thus, proper ceramic filter will reduce the pressure drop and delay the regeneration period which will reduce the fuel penalty during the filter regeneration process. If the pressure drop limit for filter regeneration is selected as 6000 Pa, for example, filter #5 would need to be regenerated after about 1500 s, while filter #6 would need about 8000 s under the same operating condition, shown in Figure 7(b). Thus optimizing the pore structure is effective to reduce the DPF pressure drop. The initial increment rates are also fitted and marked in Figure 7 using the first 120 s data of pressure drop curves. Higher initial increment rate tends to cause higher DPF pressure drop. Therefore, investigation on the relationship between the pore structure and initial increment rate is quite useful to select and optimize the DPF pore structure.

3.2. The Relationship between the Pore Structure and Initial Increment Rate of Pressure Drop. There are 9 values of initial increment rate $(d\Delta P/dt)_{\text{initial}}$ marked in Figures 6 and 7 for different pore structures and filtration velocities. However the values of $(d\Delta P/dt)_{\text{initial}}$ cannot be simply correlated with only one parameter of the velocity u , or the porosity ε_w , or the average pore diameter D_p and or the pore size distribution range 3σ , shown in Table 1. Thus a multiparameter correlation method is applied to empirically fit the data. Firstly, the Buckingham π theorem was used for a dimensional analysis

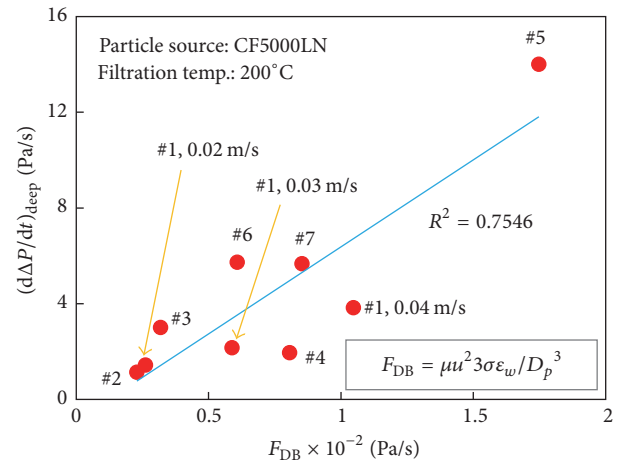


FIGURE 8: The relationship between $(d\Delta P/dt)_{\text{initial}}$ and F_{DB} .

to correlate $(d\Delta P/dt)_{\text{initial}}$ with u , ε_w , D_p , 3σ , and the exhaust dynamic viscosity μ as follows:

$$\left(\frac{d\Delta P}{dt}\right)_{\text{deep}} \propto \frac{\mu u^2 3\sigma \varepsilon_w}{D_p^3} = F_{DB}. \quad (1)$$

From (1), the values of $(d\Delta P/dt)_{\text{initial}}$ are directly proportional to the viscosity μ , u^2 , 3σ , and ε_w and inversely proportional to D_p^3 . The values of the parameter F_{DB} defined by (1) are calculated using the above parameters, and the relationship between $(d\Delta P/dt)_{\text{initial}}$ and F_{DB} is presented in Figure 8. $(d\Delta P/dt)_{\text{initial}}$ is found to generally increase with F_{DB} , while the points are dispersed along the linear fitting curve with the coefficient of determination $R^2 = 0.7546$. Equation (1) is just a dimensional analysis for the parameter of $(d\Delta P/dt)_{\text{initial}}$. The detailed physical process is ignored in this analysis, and the large deviation is obtained by directly using this correlation.

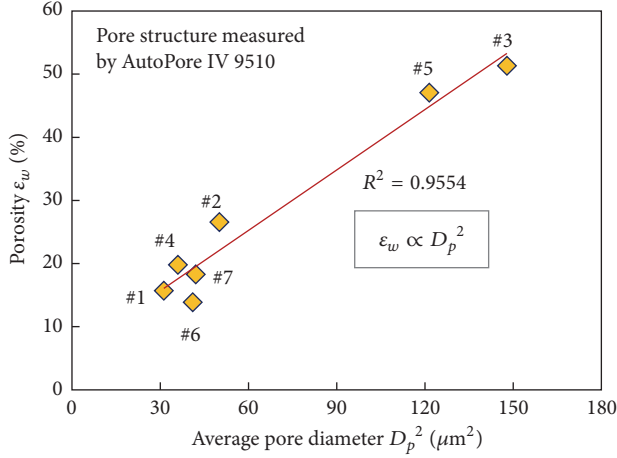


FIGURE 9: The relationship between the porosity ε_w and the diameter D_p .

The bad linear fitting can be attributed to the definitions of filtration velocity and porosity in (1). Firstly, as it has been mentioned above in Section 3.1, the initial increment rate does not increase quadratically with filtration velocity; thus the quadratic variation leads to large deviation from the linear fitting, which needs to be corrected. Secondly, larger porosity of ceramic piece would lead to lower filtration velocity and bigger particle deposition surface in micropores, so $(d\Delta P/dt)_{\text{initial}}$ would be inversely proportional to the porosity theoretically, which is contradicted to (1) variation trend. In practical condition, the porosity ε_w is actually varied together with the diameter D_p . A particular experimental relationship between them is generated during the material manufacturing process without theoretical basis. A corresponding quadratic relationship of the porosity ε_w with the diameter D_p is clearly observed in Figure 9 with the linear fitting deviation $R^2 = 0.9554$. This quadratic correlation is an experimental curve fitting of just 7 data points provided by four DPF manufactures. The data sample numbers are very limited, but we believe this relationship has certain representation to a certain degree.

Based on the special relationship between the porosity ε_w and the diameter D_p ($\varepsilon_w \propto D_p^2$), the revised parameter F'_{DB} is defined in (2) as follows:

$$\left(\frac{d\Delta P}{dt}\right)_{\text{deep}} \propto \frac{\mu u^2 3\sigma D_p}{\varepsilon_w} = F'_{\text{DB}}. \quad (2)$$

In (2), the values of $(d\Delta P/dt)_{\text{initial}}$ are proportional to D_p and inversely proportional to ε_w . The relationship between $(d\Delta P/dt)_{\text{initial}}$ and the revised parameter F'_{DB} defined by (2) is shown in Figure 10. The linear fitting degree is effectively improved as $R^2 = 0.9791$.

This relationship among various parameters in (2) is quite reasonable for DPF application. Firstly, increasing D_p without changing ε_w means to reduce the micropore numbers, which would enhance the plugging degree in micropores and lead to increase in the initial increment rate of pressure drop in deep bed filtration stage. Secondly, if the porosity ε_w is

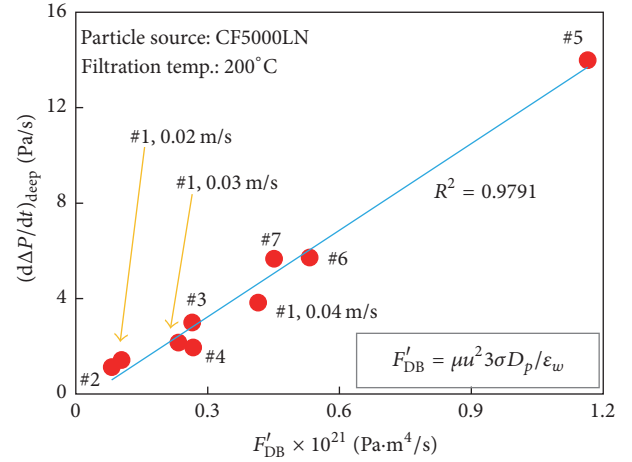


FIGURE 10: The relationship between $(d\Delta P/dt)_{\text{initial}}$ and F'_{DB} after revising parameter F'_{DB} .

increased while D_p is kept constant, the micropore number would be increased to provide larger filtration surface, which would obviously reduce the value of $(d\Delta P/dt)_{\text{initial}}$. Besides, as to the dual layer filtration technology, the upper layer has very smaller pores and very thinner thickness compared with the lower layer, which leads to significantly decreasing the average micropore size D_p and slightly decreasing the porosity ε_w . Therefore, $(d\Delta P/dt)_{\text{initial}}$ can be decreased to obtain low DPF pressure drop using the dual layer technology compared with the common or regular DPF design.

Particularly, both (1) and (2) present the same variation relation between $(d\Delta P/dt)_{\text{initial}}$ and the pore size distribution range (3σ). Reducing 3σ would reduce the value of the $(d\Delta P/dt)_{\text{initial}}$ and eventually lead to low final DPF pressure drop. Large value of 3σ means large number of the smaller micropores appearing in porous wall. Smaller micropores would act as the throat of the microflow channel in porous wall, which will result in high pressure drop during deep bed filtration process. Therefore, reducing the pore size distribution range (3σ) can improve the homogenization of the microfiltration flow in porous wall, which gives an effective method to optimize the pore structure and reduce the DPF filtration pressure drop.

3.3. Microscopic Measurement of Particle Deposition Process.

In order to conveniently observe the particle deposition process, the SEM method was applied and the results are shown in Figure 11. Four stages are observed in particle deposition process, which is in accordance with [15]. The particle deposition process can be divided as follows: Stage I, deep bed filtration stage: particles mainly deposit inside the micropores and gradually block it, while particles rarely deposit on skeletal position between adjacent micropores, shown in Figure 11(a); Stage II, particle tree growth stage: particles continually deposit into the micropores to form a particle trees (about 20~30 μm) just above the micropores, just like several "particle bread" growing from the micropores position with the heights above the ceramic surface, shown in Figure 11(b);

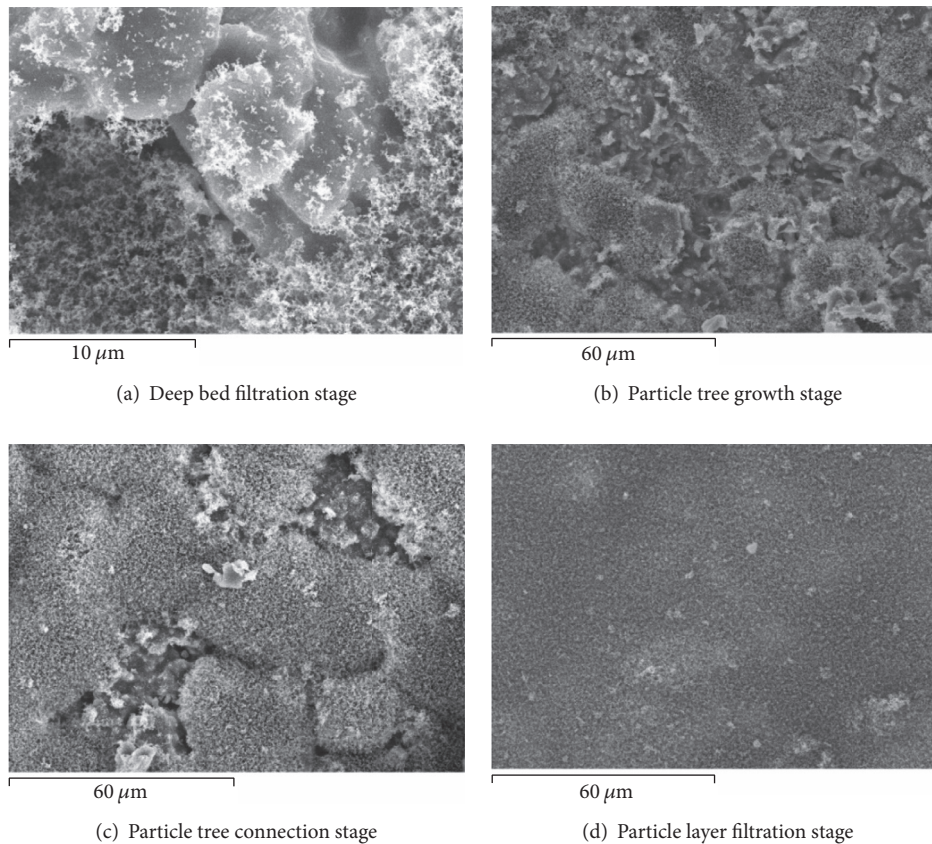


FIGURE 11: The SEM images of the surface of ceramic piece in different filtration stage (particle source: CF5000LN; filtration temp. = 200°C; filtration velocity = 0.02 m/s; #1 ceramic pieces).

Stage III, particle tree connection stage: particle trees gradually become “fat” and grow up (about 40~50 μm); inlet particles gradually deposit on the particle trees and make the particle trees connect with each other, shown in Figure 11(c); Stage IV, particle layer filtration stage: after the particle trees connect each other to cover the whole ceramic surface, the inlet particle deposit on the flat surface of the connected particle trees to form the particle layer, shown in Figure 11(d). Generally, as to the typical three-stage filtration process, the transient filtration stage could be further divided into the particle tree growth and connection stages.

Different pore structure presents different deep bed filtrations, particle tree growth, and connection stages. Once the particle layer is formed, the deposited particle layer property is nearly independent of the micropore structure just below it. Therefore, except the investigation on the influence of micropore structure on deep bed filtration stage, the effect of particle property on deposited particle layer characterization is also another hot research topic and needs to be further investigated. The SEM microscopic measurement has the limitation just for qualitatively analyzing, not for quantitatively evaluating. Thus the 2D laser displacement measurement is applied to online measure the thickness of the particle layer to understand the particle deposition process.

3.4. The Thickness of Deposited Particle Layer. The particle layer thickness is online measured and correlated with pressure drop under 0.02 m/s filtration velocity condition, which is shown in Figure 12. Two different particles are employed; one is DK4A diesel engine soot, and the other is Printex-U carbon black. The measured particle layer thickness is less than 50 μm . As to the DK4A soot, the loading time to obtain the particle layer thickness of 37 μm is about 13740 s, while the time is 1110 s to get about 50 μm particle layer thickness using the high concentration particle generator (Printex-U), compared with the low particle concentration of engine exhaust gas.

With the increase in the particle layer thickness, the pressure drop presented the similar variation trend with the relationship between pressure drop and loading time, shown in Figures 6–8. The pressure drop curves first increase rapidly and then decelerate the increment rate in the cake filtration stage. The pressure drop increases sharply when the particle layer thickness is less than about 3 μm , because the particles are mainly deposited into the micropores of ceramic piece, rather than deposited on the ceramic piece surface. So the pressure drop increases sharply, but the particle layer thickness is close to the initial status (near zero). This process is referred to as the deep bed filtration stage. After that, the particles start

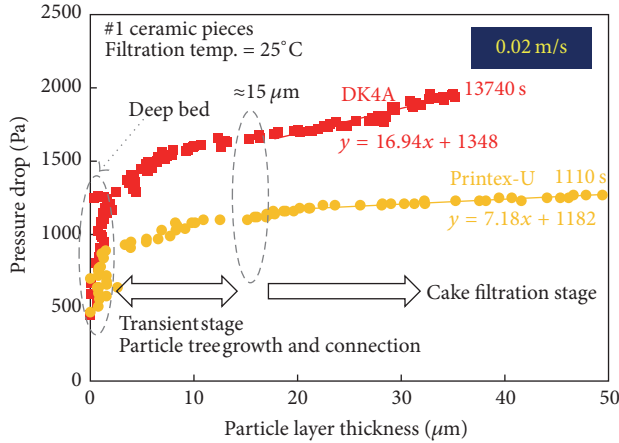


FIGURE 12: The pressure drop of ceramic pieces with the particle layer thickness.

to deposit on the ceramic surface to form particle trees and then connect each other to form the flat particle layer. During the particle tree growth and connection process, the pressure drop increases nonlinearly with the particle layer thickness. The curves are similar to those of pressure drop versus the loading time. When the particle layer thickness is larger than a critical value (about $15 \mu\text{m}$, in Figure 12), the pressure drop changes near linearly with the thickness. In this cake filtration stage, the particle layer presented to form homogeneous depositing particle layer, which leads to linear relationship between pressure drop and thickness.

Besides, the pressure drop increment rate of DK4A soot is more than two times larger than that of Printex-U particle during the particle layer filtration stage, shown in Figure 12. Although the curve of DK4A soot is measured at 200°C rather than 25°C for the Printex-U particle, the conclusion of the DK4A soot layer being denser than the Printex-U particle layer can be obtained by applying the Darcy Equation ($\Delta P = \mu \cdot u \cdot \delta_p / K_p$) to get the increment rate of $(d\Delta P / d\delta_p)_{\text{cake}} = \mu \cdot u / K_p$ (where δ_p means the particle layer thickness and K_p means the particle layer permeability). Previous studies have shown that the Printex-U particle can be served as the artificial diesel engine soot, while the particle property and particle packing property have certain difference to be noticed in the following study. Then influence of particle property on pressure drop of particle layer is studied, which is target to find a possible way to reduce the particle layer pressure drop by varying the particle property.

The pressure drop of different carbon black particles is shown in Figure 13. The filtration is selected as 0.03 m/s rather than 0.02 m/s , which is aimed at shortening the deep bed filtration stage to get different filtration process for comparison. The process of that pressure drop increases sharply while the thickness close to zero was clearly limited, for the deposited mass in unit time increasing to rapidly block the micropores to form particle tree. The shift value of particle layer thickness to start the cake filtration was delayed to about $20 \mu\text{m}$ rather than $15 \mu\text{m}$. The possible reason may be that larger velocity tends to form higher particle tree in the typical transient

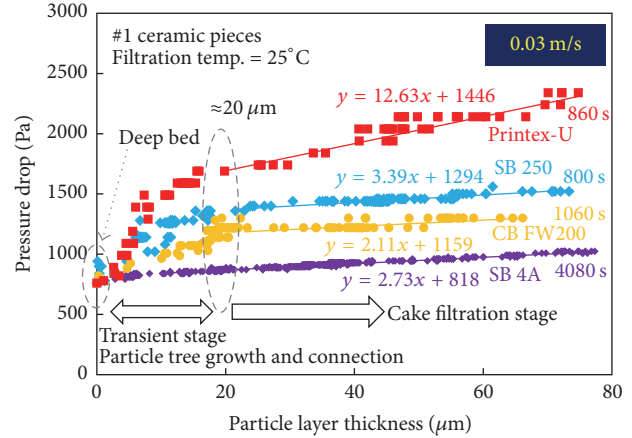


FIGURE 13: The pressure drop of different carbon black particles.

stage. The Printex-U particle presents the highest pressure drop value and increment rate compared with the other three carbon black particles, while the SB 4A particle shows the lowest pressure drop value and relative smaller increment rate in cake filtration stage. For the reason of only four particle samples, the clear correlation principle between the particle property and pressure drop cannot be curtly proposed, while the particle with large primary diameter and BET surface tend to present low pressure drop. For example, although the SB 250 particle has the largest diameter (51 nm), it also has the lowest BET surface ($40 \text{ m}^2/\text{g}$), so it presents higher pressure drop and increment rate than CB FW200 and SB 4A particle. The CB FW200 particle has the largest BET surface ($550 \text{ m}^2/\text{g}$), while it has smaller primary diameter (20 nm) compared with the SB 4A particle (44 nm , $180 \text{ m}^2/\text{g}$). So the CB FW200 particle shows higher pressure drop than SB 4A particle, while it has smaller increment rate ($2.11 \text{ Pa}/\mu\text{m}$) than that of SB 4A particle ($2.73 \text{ Pa}/\mu\text{m}$). Therefore, large primary diameter and BET surface could be beneficial to form loose particle layer to decrease the pressure drop and increment rate.

3.5. The Bulk Density of Deposited Particle Layer. Based on the measured particle layer thickness, its packing density can be obtained by weighting the deposited mass on the ceramic surface before and after particle loading, the results are shown in Figure 14. In order to investigate the compressed characterization of deposited particle layer, the filtration velocities were selected up to 0.15 m/s , which is larger than the general limit value of 0.05 m/s for usual operating condition of DPF. With the increase in the filtration velocity, the packing density increases rapidly in the low filtration velocity and then starts to slow down the increment rate when the velocity is larger than about 0.1 m/s . This result showed that the particle layer could be compressed more obviously in low filtration velocity; high filtration velocity leads to high packing density. The values packing densities range within $70\sim 92 \text{ kg}/\text{m}^3$ for Printex-U, $75\sim 105 \text{ kg}/\text{m}^3$ for DK4A, $78\sim 118 \text{ kg}/\text{m}^3$ for CB

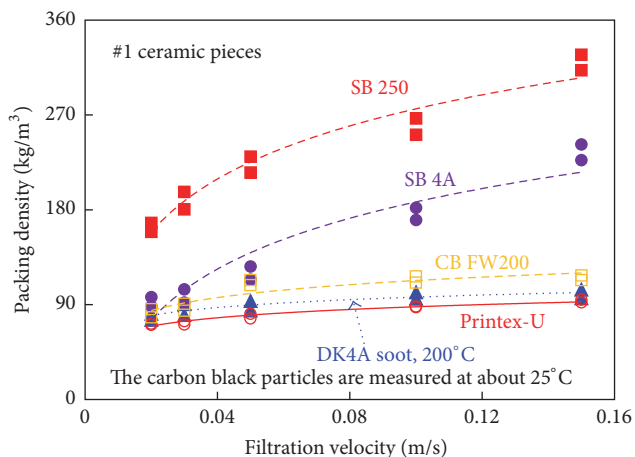


FIGURE 14: The packing density of the different particles.

FW200, 88~242 kg/m³ for SB 4A, and 160~327 kg/m³ for SB 250, respectively.

The packing density seems to be related more to the primary diameter than to the BET surface of the particles. The SB 250 particle presents the largest packing density, because it has the largest primary diameter; even its BET surface is the smallest one. Although the CB FW200 has the highest BET surface, it presents a relative smaller packing density compared with SB 250 and SB 4A particles, because it has the lowest primary diameter among them. As to the packing density, the Printex-U particle shows nearly the similar variation trend with the DK4A diesel engine soot.

4. Conclusions

Based on the experimental study presented in this paper, the following conclusions can be drawn.

- (1) The single layer channel system is proved to be capable of investigating the particle deposition process on porous ceramic surface. Except for the pressure drop and the microscopic observation, the particle layer thickness can be measured online directly for analyzing, which gives a good tool for visualizing the DPF filtration and regeneration research.
- (2) Increasing the filtration velocity can obviously decrease the deep bed filtration period, while once the particle layer is formed, the particle layer filtration process would present similar changing trends under different filtration velocities.
- (3) Increasing the filtration velocity, particle layer is obviously compressed to result in the packing density increases rapidly in the low filtration velocity and then starts to slow down the increment rate when the velocity is larger than about 0.1 m/s.
- (4) The pore structure can greatly affect the deep bed filtration to show different pressure drops. The piece with higher initial increasing pressure drop rates

and longer transition filtration stages shows higher pressure drop during particle layer filtration stage.

- (5) An experimental fitting equation for correlating the pore structure and initial increment rate of deep bed filtration has been proposed. Reducing the pore size distribution range (3σ) can improve the homogenization of the microfiltration flow in porous wall, and it can effectively result in low DPF filtration pressure drop.
- (6) The filtration process can be further divided into four progressive stages: deep bed, particle tree growth, particle tree connection, and particle layer filtration stages. The typical transient filtration stage could be further divided into the particle tree growth and connection stages, which are observed by SEM method and online thickness measurement. Besides, the thickness ranging within 15~20 μm has been found for the shift value of the transient stage to the cake filtration stage.
- (7) During the particle layer filtration stage, particle with large primary diameter and BET surface is beneficial to form loose particle layer to decrease the pressure drop and increment rate, while the packing density seems to be related more to the primary diameter than to the BET surface.

Competing Interests

The authors declare that there is no conflict of interests regarding the publication of this paper.

Acknowledgments

This work has been supported by (1) The National Natural Science Foundation of China (51676167); (2) the Chunhui Plan of the Ministry of Education of China (Z2014058); (3) the Industry Cluster project for Electronic Engine Control Systems and After Treatment Systems of Chengdu, China (2013-265); (4) Research Project of Key Laboratory of Fluid and Power Machinery (Xihua University), Ministry of Education (SZJJ2016-005); (5) Science & Technology Department of Sichuan Province (2015TD0021, 2017TD0026); and (6) the Innovation Foundation of Xihua University (YCJJ2015040, YCJJ2016087) [1].

References

- [1] A. Ben Amara, R. Dauphin, H. Babiker et al., "Revisiting diesel fuel formulation from Petroleum light and middle refinery streams based on optimized engine behavior," *Fuel*, vol. 174, pp. 63–75, 2016.
- [2] L. Chen, R. Stone, and D. Richardson, "A study of mixture preparation and PM emissions using a direct injection engine fuelled with stoichiometric gasoline/ethanol blends," *Fuel*, vol. 96, pp. 120–130, 2012.
- [3] F. Millo, D. S. Veza, T. Vlachos et al., "Particle number and size emissions from a small displacement automotive diesel engine: bioderived vs conventional fossil fuels," *Industrial and*

- Engineering Chemistry Research*, vol. 51, no. 22, pp. 7565–7572, 2012.
- [4] L. Chen, Z. Zhang, W. Gong, and Z. Liang, “Quantifying the effects of fuel compositions on GDI-derived particle emissions using the optimal mixture design of experiments,” *Fuel*, vol. 154, pp. 252–260, 2015.
 - [5] E. G. Giakoumis, C. D. Rakopoulos, A. M. Dimaratos, and D. C. Rakopoulos, “Exhaust emissions of diesel engines operating under transient conditions with biodiesel fuel blends,” *Progress in Energy and Combustion Science*, vol. 38, no. 5, pp. 691–715, 2012.
 - [6] H. Lee and Y. Jeong, “The effect of dynamic operating conditions on nano-particle emissions from a light-duty diesel engine applicable to prime and auxiliary machines on marine vessels,” *International Journal of Naval Architecture and Ocean Engineering*, vol. 4, no. 4, pp. 403–411, 2012.
 - [7] L. Chen, R. Stone, and D. Richardson, “Effect of the valve timing and the coolant temperature on particulate emissions from a gasoline direct-injection engine fuelled with gasoline and with a gasoline-ethanol blend,” *Proceedings of the Institution of Mechanical Engineers, Part D*, vol. 226, no. 10, pp. 1419–1430, 2012.
 - [8] P.-Q. Tan, S.-S. Ruan, Z.-Y. Hu, D.-M. Lou, and H. Li, “Particle number emissions from a light-duty diesel engine with biodiesel fuels under transient-state operating conditions,” *Applied Energy*, vol. 113, pp. 22–31, 2014.
 - [9] L. Chen, Z. Liang, X. Zhang, and S. Shuai, “Characterizing particulate matter emissions from GDI and PFI vehicles under transient and cold start conditions,” *Fuel*, vol. 189, pp. 131–140, 2017.
 - [10] S. H. Lee, J. H. Kwak, S. Y. Lee, and J. H. Lee, “On-road chasing and laboratory measurements of exhaust particle emissions of diesel vehicles equipped with aftertreatment technologies (DPF, urea-SCR),” *International Journal of Automotive Technology*, vol. 16, no. 4, pp. 551–559, 2015.
 - [11] A. Mamakos, G. Martini, and U. Manfredi, “Assessment of the legislated particle number measurement procedure for a Euro 5 and a Euro 6 compliant diesel passenger cars under regulated and unregulated conditions,” *Journal of Aerosol Science*, vol. 55, pp. 31–47, 2013.
 - [12] M. Masoudi, A. G. Konstandopoulos, M. S. Nikitidis et al., “Validation of a model and development of a simulator for predicting the pressure drop of diesel particulate filters,” SAE Technical Paper 2001-01-0911, 2001.
 - [13] S. Bensaïd, D. L. Marchisio, N. Russo, and D. Fino, “Experimental investigation of soot deposition in diesel particulate filters,” *Catalysis Today*, vol. 147, pp. S295–S300, 2009.
 - [14] A. Liati and P. Dimopoulos Eggenschwiler, “Characterization of particulate matter deposited in diesel particulate filters: visual and analytical approach in macro-, micro- and nano-scales,” *Combustion and Flame*, vol. 157, no. 9, pp. 1658–1670, 2010.
 - [15] S. Choi, K.-C. Oh, and C.-B. Lee, “The effects of filter porosity and flow conditions on soot deposition/oxidation and pressure drop in particulate filters,” *Energy*, vol. 77, pp. 327–337, 2014.
 - [16] J. Yang, M. Stewart, G. Maupin, D. Herling, and A. Zelenyuk, “Single wall diesel particulate filter (DPF) filtration efficiency studies using laboratory generated particles,” *Chemical Engineering Science*, vol. 64, no. 8, pp. 1625–1634, 2009.
 - [17] G. C. Koltsakis, A. Konstantinou, O. A. Haralampous, and Z. C. Samaras, “Measurement and intra-layer modeling of soot density and permeability in wall-flow filters,” SAE Technical Paper 2006-01-0261, 2006.
 - [18] A. G. Konstandopoulos, M. Kostoglou, S. Lorentzou, and N. Vlachos, “Aspects of multifunctional diesel particulate filters and their efficient simulation,” *Catalysis Today*, vol. 188, no. 1, pp. 2–13, 2012.
 - [19] Y. Mizuno, Y. Miyairi, F. Katsube et al., “Study on wall pore structure for next generation diesel particulate filter,” SAE Technical Paper 2008-01-0618, 2008.
 - [20] H. Iwata, A. Konstandopoulos, K. Nakamura, T. Kasuga, K. Ogyu, and K. Ohno, “Durability of filtration layers integrated into diesel particulate filters,” *SAE Technical Papers*, vol. 2, 12 pages, 2013.
 - [21] A. Sappok, I. Govani, C. Kamp, Y. Wang, and V. Wong, “In-situ optical analysis of ash formation and transport in diesel particulate filters during active and passive DPF regeneration processes,” SAE Technical Paper 2013-01-0519, 2013.
 - [22] T. Bollerhoff, I. Markomanolakis, and G. Koltsakis, “Filtration and regeneration modeling for particulate filters with inhomogeneous wall structure,” *Catalysis Today*, vol. 188, no. 1, pp. 24–31, 2012.
 - [23] M. Yu, D. Luss, and V. Balakotaiah, “Regeneration modes and peak temperatures in a diesel particulate filter,” *Chemical Engineering Journal*, vol. 232, pp. 541–554, 2013.
 - [24] S. Bensaïd, D. L. Marchisio, and D. Fino, “Numerical simulation of soot filtration and combustion within diesel particulate filters,” *Chemical Engineering Science*, vol. 65, no. 1, pp. 357–363, 2010.
 - [25] S.-J. Lee, S.-J. Jeong, and W.-S. Kim, “Numerical design of the diesel particulate filter for optimum thermal performances during regeneration,” *Applied Energy*, vol. 86, no. 7–8, pp. 1124–1135, 2009.
 - [26] E. Jiaqiang, W. Zuo, J. Gao, Q. Peng, Z. Zhang, and P. M. Hieu, “Effect analysis on pressure drop of the continuous regeneration-diesel particulate filter based on NO₂ assisted regeneration,” *Applied Thermal Engineering*, vol. 100, pp. 356–366, 2016.
 - [27] A. S. Shende, J. H. Johnson, S. L. Yang, S. T. Bagley, and A. M. Thalagavara, “The filtration and particulate matter oxidation characteristics of a catalyzed wall-flow diesel particulate filter experimental and 1-D 2-layer model results,” SAE Technical Paper 2005-01-0949, 2005.
 - [28] C. T. Huynh, J. H. Johnson, S. L. Yang, S. T. Bagley, and J. R. Warner, “A one-dimensional computational model for studying the filtration and regeneration characteristics of a catalyzed wall-flow diesel particulate filter,” SAE Technical Paper 2003-01-0841, 2003.